

# The Circumgalactic Medium

Hsiao-Wen Chen<sup>a</sup> and Fakhri S. Zahedy<sup>b</sup>

<sup>a</sup>The University of Chicago, Department of Astronomy & Astrophysics, 5640 S. Ellis Ave., Chicago, IL 60637, USA

<sup>b</sup>University of North Texas, Department of Physics, 210 Avenue A, Denton, TX 76201, USA

© 20xx Elsevier Ltd. All rights reserved.

## Abstract

Galaxies are part of a vast cosmic ecosystem, embedded in an extensive gaseous reservoir that regulates their growth by providing the necessary fuel for star formation while preserving a fossil record of past interactions, outflows, and feedback processes. The circumgalactic medium (CGM) contains multiphase gas spanning a broad dynamic range in spatial scale, density, and temperature, with its thermodynamic and chemical properties deeply linked to the star formation histories of galaxies. As a rich laboratory for studying gas physics, the CGM offers unique insights into the processes governing gas cooling, heating, and material transfer between galaxies and their surroundings. Chemical tagging, based on the relative abundances of multiple elements, serves as a powerful timing tool to trace the origin of the gas and connect the stars in the interstellar medium (ISM) to the diffuse CGM. Developing a complete understanding of the CGM and its cosmic evolution requires multi-wavelength observational tools, ranging from X-ray, UV/optical, and sub-mm to radio, to probe this diffuse gas in both absorption and emission.

**Keywords:** galaxy halos, cosmic ecosystems, quasar absorption lines, the baryon cycle

---

## Contents

Glossary	2
Nomenclature	2
1. Introduction	2
1.1. Cosmic ecosystems	2
1.2. A historical overview of circumgalactic research	4
1.3. The CGM and key questions in galaxy evolution	4
2. The different phases of the CGM	5
3. Observational methods	6
3.1. Emission measures	7
3.2. Absorption spectroscopy	9
4. Known empirical properties of the multiphase CGM	11
4.1. Global distributions	12
4.2. Resolved density, size, and metallicity structures	13
4.3. Thermodynamics and energy balance	15
4.4. Chemical enrichment	17
5. Future outlook	19
5.1. Spatially and spectrally resolve the multiscale and multiphase CGM in absorption and emission	20
5.2. Independent constraints from Sunyaev-Zel'dovich signals and fast radio bursts	22

---

### Key points and learning objectives

- Learn about the intricate connection between the circumgalactic medium (CGM) and galaxy formation and evolution.
- Develop an understanding of the complex multiphase and multiscale physics that shapes the diffuse cosmic gas.
- Apply chemical tagging as a timing clock for establishing chemical enrichment history
- Identify the tools needed to establish a holistic understanding of the diffuse cosmic gas.

## Glossary

**pc.** One parsec equals to  $3.086 \times 10^{18}$  cm, which is roughly 3.26 light years; 1 kpc = 1000 pc; 1 Mpc = 1000,000 pc.

**Doppler parameter.** The spectral line width of an astronomical object, caused by the internal velocity dispersion along the line of sight.

**metal.** elements heavier than hydrogen and helium.

**Voigt profile.** A mathematical representation of a spectral line, involving a convolution of a Lorentzian distribution and a Gaussian function to effectively capture the intrinsic and thermal broadening that shape spectral lines from astronomical objects.

**resonant line.** A spectral feature produced by an electron moving between the ground state and the first excited state of an atom.

**forbidden line.** A spectral feature with a very low transition probability due to the selection rules governed by the principles of quantum mechanics. These transitions are commonly seen in low-density astrophysical environments.

**nebular line.** An emission line commonly seen in ionized gas in H II regions or planetary nebulae. It is produced by electrons moving from excited states to lower orbits.

**$\alpha$ -element.** Elements formed by  $\alpha$ -capture process.

## Nomenclature

AGN	active galactic nucleus powered by a supermassive black hole in the center of a galaxy
BPT	Baldwin, Phillips, & Terlevich diagram
CGM	circumgalactic medium
HI	neutral hydrogen
H II	ionized hydrogen, one electron removed
ICM	intracluster medium
IGM	intergalactic medium
IFS	integral field spectrograph
ISM	interstellar medium
QSO	quasi-stellar object
quasar	the most luminous class of AGN
SMBH	supermassive black hole
VSF	velocity structure function
WHIM	warm-hot ionized medium
$z$	redshift, a dimensionless measure of the recession velocity of an external object
$Z$	Metallicity, that is fraction of elements heavier than helium

## 1 Introduction

Modern cosmology represents a major triumph of the scientific method. Today’s standard model of cosmology, also known as the  $\Lambda$ CDM (Lambda Cold Dark Matter) model, can explain and connect the observed large-scale structures of the Universe today, based on large spectroscopic surveys of galaxies (e.g. York et al., 2000), to the primordial density and temperature fluctuations in the early Universe observed as anisotropies in the power spectrum of the Cosmic Microwave Background (see a review by Bullock and Boylan-Kolchin, 2017). Despite  $\Lambda$ CDM cosmology’s significant success in explaining the formation of large-scale structures ( $\gtrsim 10$  Mpc scales) and their evolution over almost 14 Gyr of cosmic time, major questions remain on physical processes acting on smaller scales. This smaller scale ( $\lesssim 1$  Mpc) is the realm of the astrophysics of galaxy formation and evolution.

### 1.1 Cosmic ecosystems

Galaxies are the fundamental building blocks of our Universe, hosting various processes, with star formation being one of their primary activities. However, a puzzle emerges: star-forming galaxies across all masses lack enough material in their interstellar medium (ISM) to sustain star formation for a period comparable to their current age. The typical gas depletion timescale for these galaxies, covering a wide range of masses, is less than a few Gyr. (e.g., Bigiel et al., 2011; Kennicutt and Evans, 2012). The solution lies in the understanding that galaxies are not closed systems—they rely on an external supply of gas to replenish their ISM and sustain star formation over the lifetime of the universe.

Over the past few decades, observations have established that most galaxies, from dwarf galaxies in our cosmic neighborhood to Milky-Way analogs and giant ellipticals in the distant Universe, are surrounded by spatially extended gaseous envelope known as the circumgalactic medium (CGM). Within this gaseous envelope is the stage on which the complex and multi-scale physical processes of the baryon cycle, the two-way exchange of baryonic matter between galaxies and their environments, play out. As illustrated in Fig. 1, a composite image from combining multi-wavelength observations, galaxies accrete gas from the surrounding intergalactic medium (IGM), which can then replenish the ISM and fuel star formation. In turn, vigorous star formation activity can trigger outflows, powered by supernova explosions, that expel gas and heavy elements out of galaxies. The fate of such expelled material varies: some will eventually fall back onto galaxies

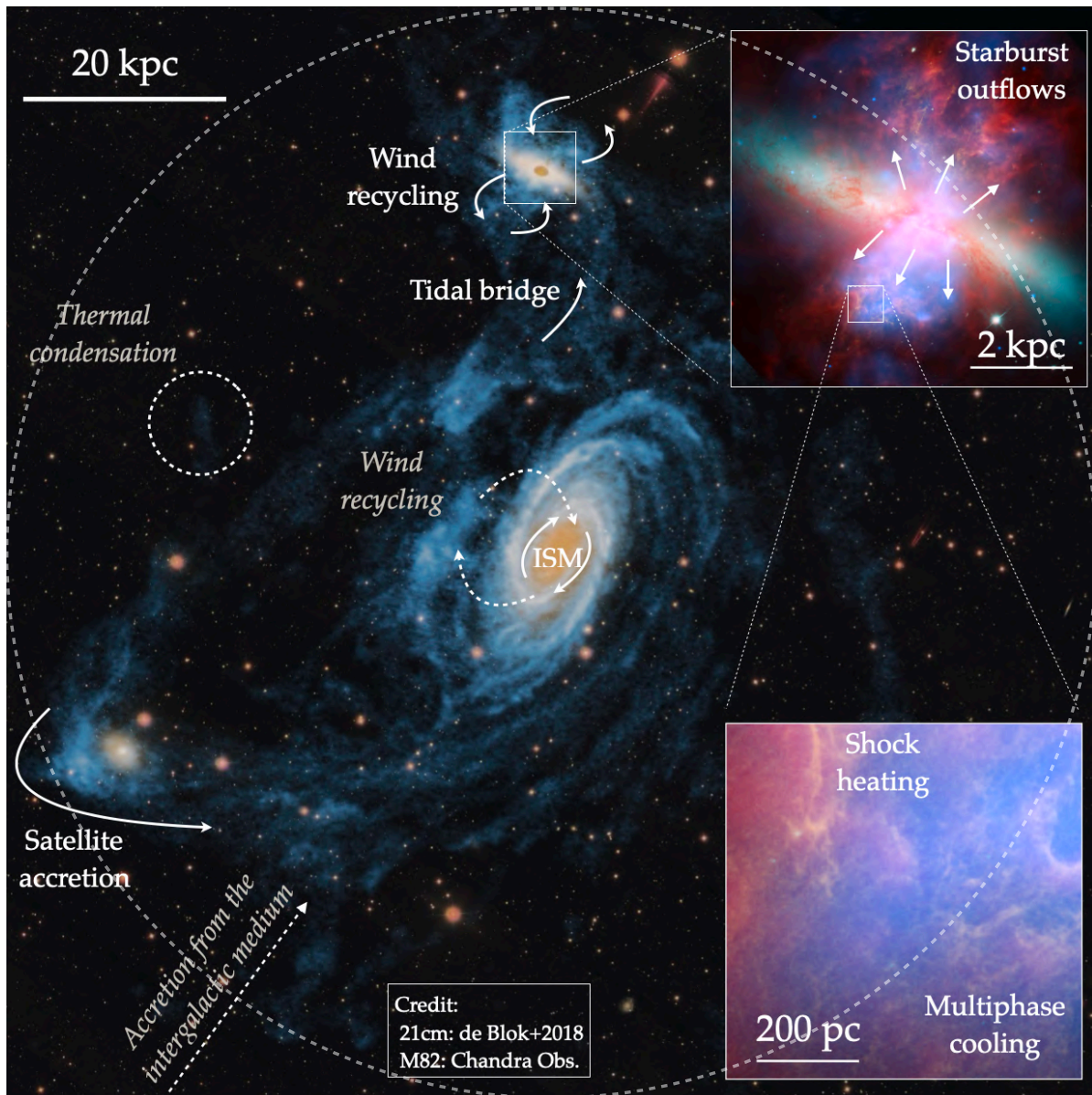


**Fig. 1** Composite images of regions around the M81 group, revealing the intricate multi-scale physical processes that govern the cycling of gas between the multiphase circumgalactic medium (CGM), stars, and galaxies within the cosmic ecosystems. HI 21 cm images covering a region of  $\approx 120$  kpc on a side centered at M81 are overlaid on top of optical images obtained from the Sloan Digital Sky Survey (SDSS; York et al., 2000). This multi-wavelength composite image (adapted from de Blok et al., 2018) showcases widespread diffuse gaseous streams uncovered by HI 21 cm observations connecting between what appear to be isolated galaxies in the optical images. The rich morphology in the diffuse HI emission enables identifications of key processes such as wind recycling, satellite accretion, tidal stripping, and possibly thermal condensation and accretion from the IGM in the broader CGM around M81. In addition, the inset in the upper-right corner displays a zoomed-in composite image of the proto-typical starburst galaxy, M82, adapted from the Chandra Observatory imaging archive). Combining X-ray and optical  $H\alpha$  images reveals powerful, multiphase starburst-driven outflowing materials reaching beyond 6 kpc in the projected distance along the polar axis. At the same time, a second inset in the lower-right corner highlights exquisite details of shock heating and multiphase cooling regions on still smaller scales of  $\sim 10$  pc.

if their potential wells are deep enough. Others may escape the gravitational pull of the galaxies and enrich the IGM instead. In addition, gravitational interactions between galaxies and the hydrodynamic effects of satellite galaxies moving through a hot halo can lead to tidal stripping and ram-pressure stripping of gas from satellite members within galaxy groups (e.g., Gunn and Gott, 1972).

There is now growing recognition that the CGM plays a key role in galaxy evolution (National Academies of Sciences, Engineering, and Medicine, 2021). With the understanding that galaxies are not isolated island universes, but instead integral parts of a cosmic ecosystem, then studying the CGM is therefore akin to developing the science of economics for galaxies. Like economics, it promotes a fuller understanding

## 4 The Circumgalactic Medium

of galaxy evolution by investigating how galaxies obtain, recycle, and exchange resources (gas) and goods (heavy elements) with their environment, and how these processes impact the course of galaxy evolution.

### 1.2 A historical overview of circumgalactic research

In the mid-20th century, Guido Münch identified gas clouds at significant heights ( $\sim 0.5\text{--}1$  kpc) above the Galactic disk. His observations were based on absorption lines from neutral sodium (Na I) and singly ionized calcium (Ca II) ions in the spectra of blue, hot stars at high Galactic latitudes. These findings were first noted in Spitzer (1956) and later formally published by Münch and Zirin (1961). The presence of these neutral and low-ionization species implies that these clouds are cool ( $T \lesssim 10^4$  K) and dense ( $n_{\text{H}} \sim 10$  hydrogen atoms  $\text{cm}^{-3}$ ). Furthermore, their observability requires that these clouds are pressure confined, which then led Spitzer (1956) to theorize the existence of a hot ( $T \sim 10^6$  K), diffuse ( $n_{\text{H}} \sim 10^{-4}$   $\text{cm}^{-3}$ ), and volume-filling gaseous corona that surrounds the Milky Way.

Münch's discovery illustrates the power of absorption-line spectroscopy for detecting and characterizing intervening gas seen along background lines of sight (see Section 3 and Fig. 5 below). This observational method would experience its first revolution sometime in the following decade, with the discovery of a class of blue point sources now known as quasars or quasi-stellar objects (QSOs). The extragalactic nature and vast, cosmological distances to these QSOs were almost immediately recognized (Schmidt, 1963; Oke and Schmidt, 1963), and many investigators started exploring the possibility of using background QSOs to detect tenuous gas outside the Galaxy (Bahcall and Salpeter, 1965, 1966; Rees and Sciama, 1967). Within only a few years, various authors had established that intervening absorption lines are a ubiquitous feature in the spectra of QSOs (e.g., Burbidge et al., 1966; Greenstein and Schmidt, 1967; Bahcall et al., 1967).

At the end of 1960s, Bahcall and Spitzer (1969) postulated that a majority of these absorption lines are produced by diffuse gas in the extended gaseous halos surrounding galaxies, as predicted by the earlier Spitzer (1956) study. However, it would be another decade before the first associations between galaxies and QSO absorption-line systems could be made, when several works identified galaxies with redshifts coincident with metal absorption species, specifically the Ca II  $\lambda\lambda 3934, 3969$  and Mg II  $\lambda\lambda 2796, 2803$  doublets previously detected in QSO spectra (e.g., Boksenberg and Sargent, 1978; Boksenberg et al., 1980; Bergeron, 1986). A common feature of these findings were the large projected distances between the QSO lines of sight and the foreground galaxies associated with the absorption, far above the disk size and consistent with the extended halo physical picture of Bahcall and Spitzer (1969).

In the few decades following these pioneering studies, observational studies of the CGM have continued to rely largely on the absorption lines imprinted by the intervening CGM gas in QSO spectra. In particular, the advent of the *Hubble Space Telescope* (HST) and large ground-based telescopes in the 1990s and early 2000s triggered a second renaissance of the field by allowing systematic studies to characterize the extended gaseous halos of galaxies using large samples ( $\gtrsim$  dozens) of background QSO-foreground galaxy pairs (e.g., Morris et al., 1993; Lanzetta et al., 1995; Steidel et al., 1997; Chen et al., 1998, 2001), a trend that has continued to the present day.

### 1.3 The CGM and key questions in galaxy evolution

In the  $\Lambda$ CDM paradigm, linear matter overdensities seeded during the early Universe grow over time until they reach a point where self-gravity begins to dominate, and they collapse to form dark-matter halos. Because baryonic matter is subdominant to dark matter in mass, the fate of these baryons is to be accreted into the gravitational potential wells of dark matter halos. The accreted baryons cool radiatively and condense over time as they fall deeper into the center of a dark-matter halo (Rees and Ostriker, 1977; White and Rees, 1978), eventually forming dense, molecular gas complexes stars are born out of. The primary objective of galaxy evolution studies is to explain how from a seemingly simple beginning came the incredibly diverse population of galaxies seen across cosmic time. Here we outline several major problems in galaxy evolution studies and motivate how the CGM is linked with each one.

1. **Why have galaxies turned so little of their baryons into stars?** In the present day, galaxies across all masses harbor only a small fraction of their dark matter halo's cosmological budget of baryons in stars and ISM gas. While dark-matter halos hosting Milky-Way sized galaxies appear to be the most efficient in turning their gas to stars, even then fewer than 20% of their budgeted baryons are locked in stars. Lower mass halos hosting dwarf galaxies and massive halos hosting giant elliptical galaxies have done far worse, with fewer than  $\lesssim 5\text{--}10\%$  of their baryons converted into stars (e.g., Kravtsov et al., 2018). Such mass dependence in a dark matter halo's global star formation efficiency suggests that multiple physical processes are at play across different mass regimes to regulate star-formation processes. The CGM is an excellent venue to search for evidence of the physical processes responsible for the regulation of star formation.

2. **Where are the baryons and how did they get so far away from galaxies?** If a great majority of baryons are not locked in stars within galaxies, where are they? The first possible answer is that most baryons have never been incorporated into galaxy halos to begin with, and they remain in the IGM. While observations of the Lyman-alpha ( $\text{Ly}\alpha$ ) forest indicate that this is the case at high redshifts ( $z > 2$ , e.g., Rauch, 1998), the cool IGM's share of the cosmic baryon budget appears to be a factor of several times lower in the present day. Another possibility is that a large fraction of baryons were once accreted into dark matter halos, but they had since been heated and possibly expelled out of halos due to energetic feedback processes from galaxies, and they now reside in a warm-hot ionized phase (WHIM; e.g., Bregman, 2007; McQuinn, 2016). However, detecting WHIM is extremely challenging due to the expected low densities and high temperatures ( $T \sim 10^{5\text{--}7}$  K;  $n_{\text{H}} < 10^{-4}$   $\text{cm}^{-3}$ ), and empirical constraints on their baryonic content remain highly uncertain to date. The final scenario is that baryons reside within dark matter halos, but unlike ISM gas they are too diffuse and therefore difficult to detect in emission. Characterizing the physical properties of the CGM and accounting for its various gas phases and how they relate to the baryon budget is therefore of great importance to solving this problem and distinguishing between the three scenarios above.

3. **Why do some galaxies stop forming stars altogether and stay that way?** Among different populations of galaxies, massive quiescent galaxies present some of the most perplexing problems in galaxy evolution studies. These massive galaxies, with total stellar masses of  $M_{\text{star}} \gtrsim 10^{11} M_{\odot}$  and residing in dark-matter halos with of  $M_{\text{h}} \gtrsim 10^{13} M_{\odot}$ , are dominated by old ( $\gtrsim 5$  Gyr) stellar populations



(e.g., [Tojeiro et al., 2011](#)). Unlike lower-mass galaxies like our Milky Way, these massive galaxies show little ongoing star formation and appear to have ceased forming stars for many Gyr (e.g., [Ferreiras et al., 2009](#)). A natural expectation is that these galaxies lack the cool gas needed to replenish their ISM and restart star formation. Searching and characterizing the cool CGM of these massive quiescent galaxies is, therefore, necessary to advance our understanding of massive galaxy evolution.

## 2 The different phases of the CGM

The multiphase nature of the CGM is reflected by the co-presence of gas at different temperatures, densities, and ionization states in both observations and simulation studies. Observationally, multi-wavelength images of the Milky Way and nearby galaxies have revealed complex mixtures of different gas phases (e.g., [Putman et al., 2012](#)). An example of the M81 group with a total mass of  $M_h \approx 10^{12} M_\odot$  (e.g., [Karachentsev and Kashibadze, 2006](#)) is displayed in Fig. 1. Composites of radio 21 cm observations (targeting neutral hydrogen gas), optical narrow-band images (targeting nebular lines from ionized gas), and X-ray images (targeting hot plasma) unveil the intricate structures of cold neutral gaseous streams of  $T \lesssim 1000$  K connecting between member galaxies of the group across  $\sim 100$  kpc in the projected distance. These are in addition to detailed multiphase gaseous structures on scales of  $\sim$  pc in the biconical outflows from M82. This multiphase gas fills up the immense space between luminous stellar bodies. What is missing in this image is the ambient hot atmosphere too faint to be detected using existing X-ray telescopes, but routinely observed around more massive galaxies and galaxy clusters of mass exceeding  $M_h \approx 10^{14} M_\odot$  in the nearby universe (e.g., [Sun et al. 2009](#), [O’Sullivan et al. 2017](#); see also [Donahue and Voit 2022](#) for a recent review). In halos hosting galaxy groups of  $M_h \approx 10^{13} M_\odot$ , ionized hot plasma has been detected through absorption features of high-ionization species, such as O VI and O VII, which correspond to oxygen atoms that have been ionized five and six times, respectively (e.g., [Mulchaey et al., 1996](#); [Fang et al., 2002](#)) and the Sunyaev-Zel’dovich signals against the cosmic microwave background (e.g., [Carlstrom et al., 2002](#); [Hand et al., 2011](#); [Pratt et al., 2021](#); [Hadzhiyska et al., 2024](#)).

Moving further into the distant Universe, absorption line spectroscopy has also uncovered absorption features at different wavelengths, providing signposts for different ionization states of elements like hydrogen, oxygen, silicon, and carbon (see Section 3). These ions, such as neutral hydrogen (HI), CIV and OVI, trace gas at a broad range of temperatures. Their distinct absorption line profiles also reflect this. Cooler gas moves more slowly with smaller velocity dispersions, leading to a narrower line width, while hotter gas associated with more energetic outflows or more diffuse halo structures exhibits a broader line width.

Cosmological simulations incorporating baryonic physics have consistently shown that the diffuse gas permeating the universe makes up the majority of baryonic matter. The thermal and ionization conditions of the gas are dictated by different competing heating and cooling processes and can be broadly classified into four different regimes (e.g., [Torrey et al., 2019](#), see also Fig. 2). Specifically, in the low-density IGM, the primary heating source is photoionization by the metagalactic ionizing radiation field (e.g., [Madau, 1995](#); [Haardt and Madau, 2012](#); [Khairé and Sriand, 2019](#); [Faucher-Giguère, 2020](#)). As the Universe expands, the IGM undergoes adiabatic cooling, forming a diffuse phase with a tight correlation between gas temperature and density (e.g., [Hui and Gnedin, 1997](#), see the *upper-left* panel of Fig. 2). At the mean density of the present-day Universe,  $n_H \approx 10^{-5} \text{ cm}^{-3}$ , this unshocked gas remains at a relatively cool temperature of  $T \sim 10^4$  K. At the same time, gas in overdense regions is expected to follow gravitational collapse and become shock-heated to virial temperature  $T_{\text{vir}}$ , which scales with the mass of the bound “halo”,  $M_h$ , according to  $T_{\text{vir}} \approx 1.2 \times 10^6 \text{ K} (M_h/10^{12} M_\odot)^{2/3}$  from the Virial theorem (e.g., [Mo et al., 2010](#)). The gas remains hot due to inefficient cooling at low densities of  $n_H \lesssim 10^{-4} \text{ cm}^{-3}$ . Within the hot halos, density fluctuations induced by various dynamical processes, including IGM accretion, satellite interactions, turbulence, and feedback from active galactic nuclei (AGN) or massive stars are expected to trigger thermal instabilities with higher-density regions cooling at a faster rate (e.g., [Mo and Miralda-Escude, 1996](#); [Maller and Bullock, 2004](#); [Voit et al., 2017](#)). As the temperature decreases, these regions are expected to collapse and form cooler and higher-density clumps of  $T \sim 10^4$  and  $n_H \gtrsim 0.01 \text{ cm}^{-3}$ , re-establishing pressure equilibrium with the ambient hot medium. The gas remains ionized by the metagalactic ionizing radiation field. At the interface of the cool clumps and hot medium, a transient warm-hot ionized phase of  $T \sim 10^{5-6}$  and  $n_H \sim 10^{-3} - 10^{-4} \text{ cm}^{-3}$  can form through shocks or turbulent mixing due to accretion or outflows interacting with the ambient medium.

To capture the full range of physical processes that shape the properties of multiphase gas, it is essential to sample the broad dynamic range of temperatures and densities across a representative cosmological volume—a daunting challenge for both theoretical and observational studies. To the advantage of astronomers, different metal ions can serve as tracers of different gas phases, depending on the gas’s chemical composition, temperature, and density (e.g., [Osterbrock and Ferland, 2006](#)). Each ion’s distinctive electron configuration provides unique line transitions as empirical probes of these gas phases. For example, in cool, condensed clouds, metals are primarily singly ionized and prominent transitions include Mg II, and Ca II, similar to what is observed in the ISM. In contrast, more highly ionized species dominate in progressively warmer, lower-density gas and sensitive tracers include CIV for warm ionized gas and OVI for the warm-hot plasma (Fig. 2; see [Verner et al., 1994b,a](#), for a more complete list of transition). Therefore, targeting a suite of ions and their associated line features provides a powerful tool for characterizing the multiphase CGM.

A census of the mass budget between different baryonic components in halos like the Milky Way is summarized in the *lower-left* panel of Fig. 2. Stars and ISM in star-forming regions make up less than 25% of the expected total baryonic mass from the cosmic baryon-to-dark matter ratio (e.g., [Planck Collaboration et al., 2020a](#)). In contrast, the cool and warm-hot ionized phases combined in the CGM contribute to a comparable amount of mass (and likely more) found in stars. A still larger fraction of baryonic mass is found in the hot atmosphere but with large associated uncertainties due to observational challenges. The schematic diagram in Fig. 2 illustrates the relative spatial distributions of these different phases in a galaxy halo, following a common pressure profile. Condensed cool clumps occur primarily in the inner halo or along the filaments, while low-density, warm clouds are seen primarily in the halo outskirts. These clumps are embedded

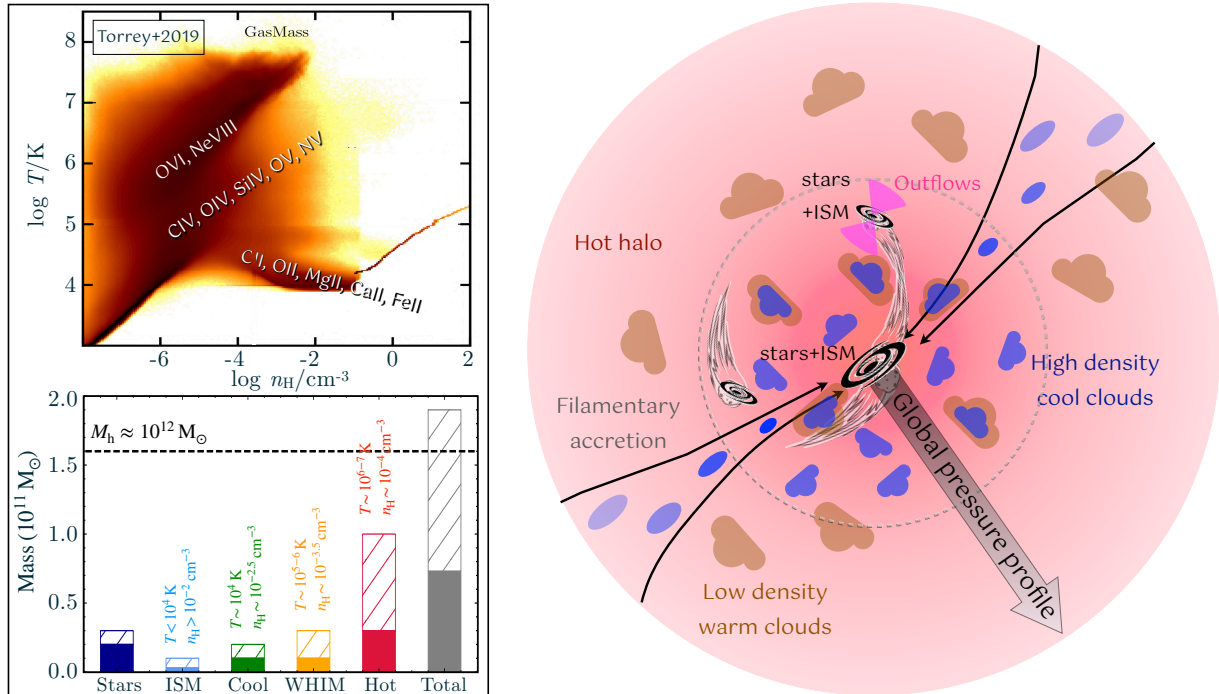


**Fig. 2** The galactic atmosphere, encompassing the multiphase CGM, spans a broad range in temperature and density. Cosmological simulations have shown that the gas content of the Universe can be broadly classified into four different regimes, from cool, photoionized IGM of temperature  $T \lesssim 10^4$  K and density  $n_{\text{H}} \lesssim 10^{-5} \text{ cm}^{-3}$ , condensed cool gas of  $T \sim 10^4$  K and  $n_{\text{H}} \sim 10^{-2} \text{ cm}^{-3}$  in galactic halos, warm-hot ionized medium (WHIM) of  $T \sim 10^{5-6}$  K and  $n_{\text{H}} \sim 10^{-2} - 10^{-4} \text{ cm}^{-3}$ , and to low-density hot plasma of  $T > 10^6$  K and  $n_{\text{H}} \lesssim 10^{-4} \text{ cm}^{-3}$ , separate from the cool IGM of  $T \sim 10^4$  K and  $n_{\text{H}} \lesssim 10^{-5} \text{ cm}^{-3}$  which contains less than 40% of the total mass in the diffuse gas phase (upper-left panel; adapted from Torrey et al., 2019, for the  $z = 0$  Universe). These different phases are most effectively probed by absorption transitions associated with different ionic species, with low-ionization lines such as C II and Mg II tracing the cooler and higher density phase and higher-ionization lines such as O VI and Ne VIII tracing hotter and lower-density gas. The current mass census for different baryonic components in a Milky-Way-like halo of  $M_{\text{h}} \approx 10^{12} M_{\odot}$  at  $z < 1$  is summarized in the lower-left panel. The horizontal dashed line indicates the anticipated total baryonic mass from the cosmic baryon-to-dark matter ratio (e.g. Planck Collaboration et al., 2020b). Colored bars represent the best-estimated mass contributions of stars (e.g., Kravtsov et al., 2018; Behroozi et al., 2019), the ISM (e.g., Parkash et al., 2018), and different phases of the CGM at distinct temperature and density regimes with uncertainties indicated by the hatched regions (see e.g., Faerman and Werk, 2023; Qu et al., 2023; Zhang et al., 2024). Stars and the ISM combined contribute to less than 25% of the total baryonic mass in galaxy halos, while the majority of baryons reside in the diffuse gas phases. The schematic diagram in the right panel illustrates the current empirical understanding of the multiphase galactic atmosphere. Large-scale processes such as tidal stripping, filamentary accretion from the IGM, and thermodynamics of the hot halo interact to shape the CGM structure. Cool, dense clumps occur primarily in the inner halo or filaments, while warm, low-density clouds occur primarily in halo outskirts, establishing a global pressure profile (see also Voit et al., 2019; Qu et al., 2023). These processes collectively contribute to the complex evolution of gas around galaxies, influencing star formation and galactic growth.

in a hot atmosphere stirred by various large-scale dynamical processes, including tidal stripping of satellite galaxies, IGM accretion, and outflows interacting with the hot halo. As the cool clumps move through the hot medium, turbulent mixing layers are expected to develop resulting in an additional intermediate transient phase.

While significant progress has been made in understanding the multiphase structure of the CGM around Milky Way-like galaxies, key questions remain. Among them are the fate of cool gas clumps and the distribution of baryons across halos of varying mass and star formation histories. Under gravity, cool, dense clumps are expected to fall through the hot halo, but whether they can survive this descent has major implications for maintaining the fuel needed to sustain star formation. Moreover, the large uncertainties in the CGM mass budget, as shown in Fig. 2, suggest that more than half of the baryons may lie beyond the gravitationally bound halos. This has profound implications for the energy required to drive galactic outflows and highlights the persistent issue of the missing baryons in the universe (e.g., Shull et al., 2012; de Graaff et al., 2019).

### 3 Observational methods

To investigate diffuse multiphase gas, it is essential to consider how gas particles interact with photons. Taking hydrogen as an example, each neutral atom consists of one electron in a quantum state of energy  $E_n = -13.6 \text{ eV}/n^2$ . To ionize a hydrogen atom and eject its electron,

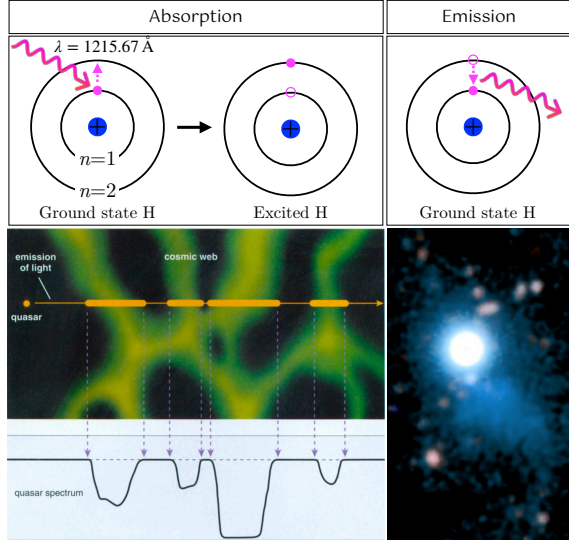


**Fig. 3** Mapping the diffuse cosmic gas based on absorption and emission signals. *Top*: Absorption of  $\text{Ly}\alpha$  photons with energy matching the difference between the first and second electron levels of hydrogen atoms elevates the electron to the first excited state, attenuating the flux at  $\text{Ly}\alpha$  wavelength, 1215.67 Å. When the excited electron decays back to the ground state, a  $\text{Ly}\alpha$  photon is emitted, revealing the location of the hydrogen atom. Gaseous streams within the cosmic filaments, made of primarily hydrogen, intercept the light from distant background quasars and are expected to attenuate the light at the  $\text{Ly}\alpha$  wavelength at the rest frame of the streams, resulting in absorption line features in the quasar spectra (*bottom left*; credit: Robert A. Simcoe, 2004, American Scientist; see also Fig. 5 below). The “forest” of  $\text{Ly}\alpha$  absorption features provides a sensitive one-dimensional probe of density fluctuations along the line of sight toward the background quasar. Conversely, observations of  $\text{Ly}\alpha$  photons in emission provide two-dimensional maps of density fluctuations in the galactic atmosphere (*lower-right*; adapted from Cantalupo et al., 2014, see also Fig. 4 below).

a high-energy photon with at least 13.6 eV (corresponding to a wavelength of  $\lambda = 912 \text{ \AA}$  or 91.2 nm) is required. As noted in Section 2, the diffuse IGM is expected to be fully ionized by the metagalactic ionizing radiation field, maintaining a typical temperature of  $10^4 \text{ K}$  (e.g. Osterbrock and Ferland, 2006). Under equilibrium, the photoionization and recombination maintain a stable fraction of neutral hydrogen following  $n_{\text{HI}} \Gamma = n_e n_p \alpha$ , where  $n_{\text{HI}}$ ,  $n_e$  and  $n_p$  represent respectively the neutral hydrogen, electron, and ionized hydrogen densities. The likelihood of an electron being ejected from a neutral hydrogen atom or captured by ionized hydrogen is quantified by the photoionization rate  $\Gamma$  and the recombination coefficient  $\alpha$ , respectively. The ionization balance equation naturally leads to the expected neutral fraction,  $f_{\text{HI}} \equiv n_{\text{HI}} / (n_{\text{HI}} + n_p)$  and  $n_p \approx n_e \approx n_{\text{H}}$  for highly ionized gas, leading to  $f_{\text{HI}} \approx n_{\text{HI}} / n_p = n_e \alpha / \Gamma$ . Although this neutral fraction is minuscule in the IGM ( $f_{\text{HI}} \lesssim 0.01$ ), hydrogen is the most abundant element in the Universe (e.g., Payne, 1925). These few neutral hydrogen atoms can produce observable signals, providing critical insights into the physical state of the diffuse IGM (e.g., Rauch, 1998).

A prominent spectral feature in photoionized gas is the hydrogen  $\text{Ly}\alpha$  line, which is produced when an electron in a neutral hydrogen atom transitions between the ground state ( $n = 1$ ) and the first excited state ( $n = 2$ ), releasing or absorbing energy equivalent to 10.2 eV. This energy corresponds to a wavelength of 1215.67 Å (or 121.567 nm). As illustrated in Fig. 3, neutral hydrogen atoms in the ground state (typical for gas cooler than a few  $\times 10^4 \text{ K}$ ) absorb photons at this wavelength, causing electrons to move to the  $n = 2$  level, resulting in the attenuation of  $\text{Ly}\alpha$  photon flux. Shortly after excitation, the electrons return to the ground state, emitting a  $\text{Ly}\alpha$  photon. Similar excitation and de-excitation processes occur for other elements, creating absorption or emission lines. The diffuse IGM and CGM emit extremely faint light when illuminated by background radiation. The interactions between gas particles and background photons vary based on density, temperature, and ionization state, producing distinct spectral features. By analyzing these features, astronomers can reconstruct 3D maps of these physical quantities, providing critical insights into the underlying cosmic structures and helping to constrain theoretical models.

### 3.1 Emission measures

Direct imaging of faint emission from cosmic gas offers a detailed map of the cosmic matter distribution, revealing the intricate connections and interactions between this diffuse gas and galaxies where stars form. The brightness of the gas can be predicted using its emission coefficient,  $j_\nu$ , which quantifies the energy radiated per unit volume, per unit solid angle (measured in steradians), and per unit time. For hydrogen  $\text{Ly}\alpha$  emission, this is determined by the likelihood of a free electron being captured by an ionized hydrogen atom and subsequently releasing a  $\text{Ly}\alpha$  photon. It can be shown following the electron cascades that for every recombination event, the probability of releasing a  $\text{Ly}\alpha$  photon is  $\eta_\alpha = 0.68$  (0.41) in optically thick (thin) cases (e.g., Dijkstra, 2017). The  $\text{Ly}\alpha$  emissivity of diffuse photoionized gas is directly related to the recombination rate of free electrons in the ionization balance equation described above, following  $j_{\text{Ly}\alpha} = (h\nu_{\text{Ly}\alpha} / 4\pi) n_e n_p \alpha_{\text{Ly}\alpha}^{\text{eff}}$  erg s<sup>-1</sup> cm<sup>-3</sup> str<sup>-1</sup>. Here  $h$  is the Planck constant,  $\nu_{\text{Ly}\alpha}$  the  $\text{Ly}\alpha$  photon frequency, and  $\alpha_{\text{Ly}\alpha}^{\text{eff}} = \eta_\alpha \alpha$  is the effective recombination coefficient to the  $2p$  state, from where a transition to the  $n = 1$  is allowed (e.g., Draine, 2011; Dijkstra, 2017). For fully-ionized gas, where  $n_e \approx n_p \approx n_{\text{H}}$ , it is straightforward to work out the anticipated surface brightness signal, integrated over a finite depth ( $l_{\text{neb}}$ ) of a nebula at redshift  $z$ , as  $\text{SB}_{\text{Ly}\alpha} \approx 1.5 \times 10^{-14} (l_{\text{neb}} / 1 \text{ kpc}) n_{\text{H}}^2 / (1+z)^4$  erg s<sup>-1</sup> cm<sup>-2</sup> arcsec<sup>-2</sup> at  $T \approx 10^4 \text{ K}$ , where  $(1+z)^{-4}$  factor accounts for the cosmological surface brightness dimming due to expansion of the Universe.

It is immediately clear that the observed strength of the emission signals depends sensitively on two factors: (1) the ionized gas density (and implicitly the intensity of the ionizing radiation field) and (2) redshift. Because the anticipated signal depends on  $n_{\text{H}}^2$ , the highest density peaks are expected to drive the observed signals. It is therefore helpful to introduce a clumping factor,  $C \equiv \langle n_{\text{H}}^2 \rangle / \langle n_{\text{H}} \rangle^2$ , and recast the emissivity to  $j_{\text{Ly}\alpha} = (h\nu_{\text{Ly}\alpha} / 4\pi) C \langle n_{\text{H}} \rangle^2 \alpha_{\text{Ly}\alpha}^{\text{eff}}$ . Because of the  $(1+z)^{-4}$  dependence, the anticipated signal fades drastically with increasing redshift. For a 1-kpc size CGM clump of  $n_{\text{H}} = 0.001 \text{ cm}^{-3}$  (e.g., Chen et al., 2023a) at  $z = 2$ , the expected  $\text{Ly}\alpha$  surface brightness signal is exceedingly faint at  $\text{SB}_{\text{Ly}\alpha} \approx 2 \times 10^{-22} \text{ erg s}^{-1} \text{ cm}^{-2} \text{ arcsec}^{-2}$  for  $C = 1$ . Detecting this faint  $\text{Ly}\alpha$  emission signals from the diffuse



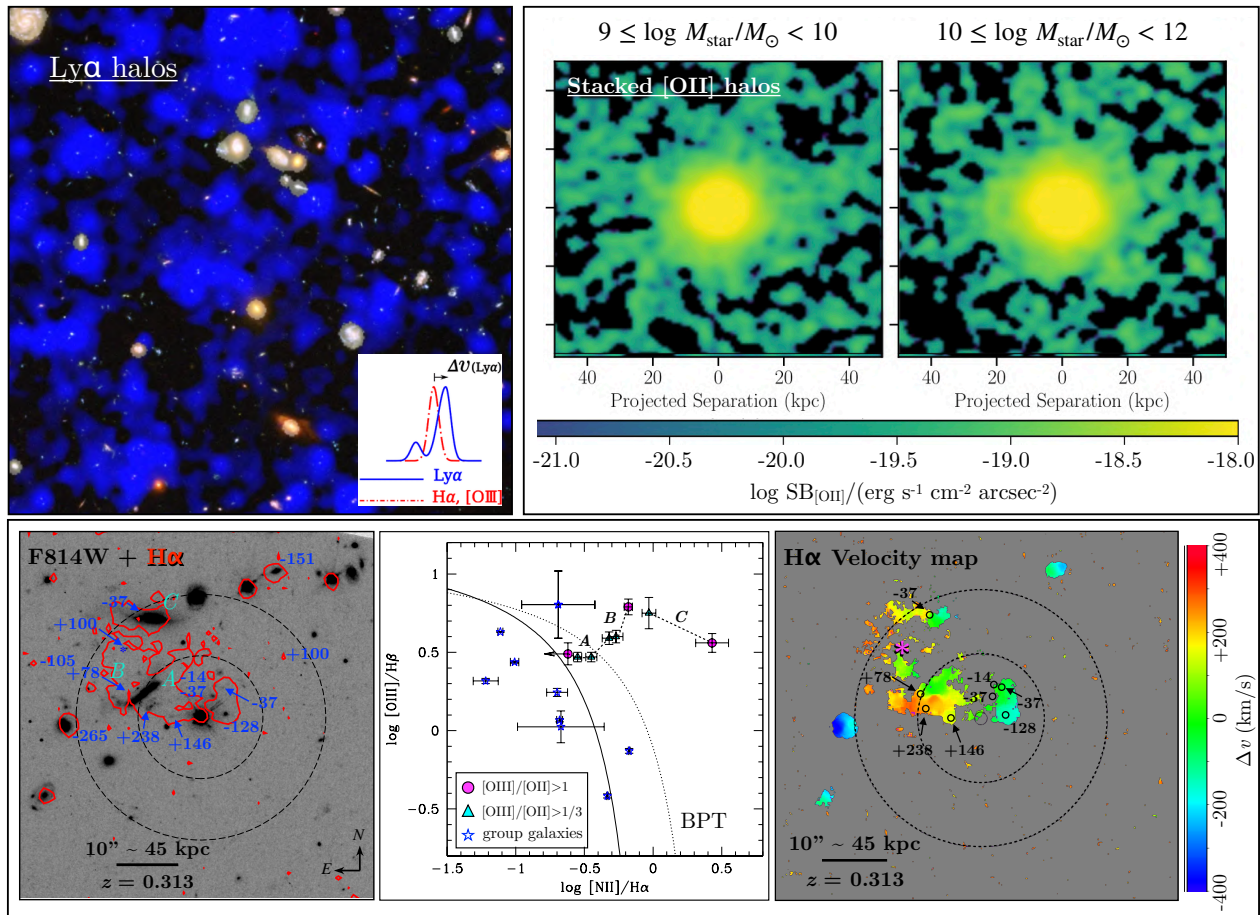


**Fig. 4** The spatial extent and ionization conditions of the diffuse galactic atmosphere revealed in two-dimensional line emission maps. Spatially extended  $\text{Ly}\alpha$  emitting nebulae (blue clouds in the *top-left* panel) are ubiquitous around high-redshift galaxies, revealing a substantial amount of gas beyond star-forming regions (reproduced from [Wisotzki et al. 2018](#); see also [Cantalupo 2017](#); [Arrigoni Battaia et al. 2019](#) for similar findings around distant quasars). Due to a high cross-section with hydrogen particles, each  $\text{Ly}\alpha$  photon is expected to undergo a sequence of random walks both in space and frequency before escaping the parent cloud resulting in a double peak profile. This is different from a single Gaussian line profile expected for non-resonant lines such as  $\text{H}\alpha$  or  $[\text{O III}]$ , resulting in an apparent offset in the observed line centroids, as illustrated in the inset (cartoon adapted from [Yang et al. 2014](#)). The two *top-right* panels (reproduced from [Dutta et al. 2024](#)) summarize the current effort in expanding such observations to lower mass over an ensemble of halos. While routine observations of individual galaxies remain challenging due to faint signals, progress is being made by stacking narrow-band images targeting nebular lines over hundreds of sources. In doing so, astronomers have detected extended line-emitting gas around galaxies with stellar mass as low as  $M_{\text{star}} \approx 10^8 M_{\odot}$  with the detected nebular size increasing with  $M_{\text{star}}$  at  $z \lesssim 1$ . The *bottom* panels display a unique case where a giant line-emitting nebula spanning  $\sim 100$  kpc in diameter is discovered in a low-mass galaxy group with an estimated total mass of  $M_h \approx 3 \times 10^{12} M_{\odot}$  at  $z = 0.3$  (adapted from [Chen et al., 2019](#)). The observed  $\text{H}\alpha$  surface brightness contours are overlaid on top of *Hubble Space Telescope* F814W image (*bottom left*). Both the velocity field (*bottom right*) and line-emission morphology of the nebula support the origin of the nebula in tidal streams connecting members of the galaxy group. This intragroup nebula is detected in multiple nebular lines, including  $[\text{O II}]$ ,  $\text{H}\beta$ ,  $[\text{O III}]$ , and  $[\text{N II}]$ , in addition to  $\text{H}\alpha$ . The observed  $[\text{O III}]/\text{H}\beta$  and  $[\text{N II}]/\text{H}\alpha$  line ratios in the BPT panel reveal an enhanced ionization in the intragroup gas (magenta circles and cyan triangles from regions A, B, and C marked in the image panel) relative to the star-forming ISM (blue star symbols) in member galaxies of the group, likely due to shocks generated by the gaseous streams moving across the unseen hot intragroup medium at supersonic speeds (e.g., [Baldwin et al., 1981](#); [Kewley et al., 2019](#)).

IGM remains out of reach (see e.g., [Hogan and Weymann, 1987](#); [Kollmeier et al., 2010](#)). In contrast, dedicated surveys on large ground-based telescopes, ultra-long integrations ( $\approx 30$ -100 hours) on the 8 m Very Large Telescopes (VLT) are beginning to uncover extended  $\text{Ly}\alpha$  emission signals of  $\text{SB}_{\text{Ly}\alpha} \approx \text{a few} \times 10^{-20} \text{ erg s}^{-1} \text{ cm}^{-2} \text{ arcsec}^{-2}$  out to  $\approx 30$  kpc from star-forming galaxies at  $z \gtrsim 3$  (Fig. 4, adapted from [Wisotzki et al. 2018](#); see also [Rauch et al. 2008](#)). In addition, giant  $\text{Ly}\alpha$  nebulae of surface brightness  $\text{SB}_{\text{Ly}\alpha} \gtrsim 10^{-18} \text{ erg s}^{-1} \text{ cm}^{-2} \text{ arcsec}^{-2}$  and spatial extent  $> 100$  kpc are also found ubiquitous around luminous quasars (e.g., [Cantalupo et al., 2014](#); [Martin et al., 2015](#); [Borisova et al., 2016](#); [Arrigoni Battaia et al., 2019](#)), suggesting a causal link between the presence of the cool gas ( $T \sim 10^4$  K) and the quasar phase.

While optically thick gas exposed to the intense ionizing radiation from a quasar is expected to glow in  $\text{Ly}\alpha$  at a much higher intensity,



constraining the gas properties based on the observed signals is challenging due to their uncertain origins. Recombination radiation, resonant scattering, cooling radiation, or a combination thereof can contribute to the observed Ly $\alpha$  signals. In addition, the large absorption cross-section expected of the Ly $\alpha$  photons ensures that in ionizing clouds with even a modest neutral hydrogen column density of  $N_{\text{HI}} > 10^{13} \text{ cm}^{-2}$ , these photons will undergo a sequence of random walk in both space and frequency before leaving the nebula (see e.g., [Dijkstra, 2017](#), for a pedagogical review). Ly $\alpha$  emission originating in infalling (outflowing) medium is expected to exhibit a blue-enhanced (red-enhanced) double-peak profile (see illustration reproduced from [Yang et al. 2014](#) in the inset of the *upper-left* panel in Fig. 4). While the strong coupling between the Ly $\alpha$  photons and the underlying gas motions make spectrally resolved Ly $\alpha$  profiles a valuable probe of gas kinematics, constraining the gas properties requires sophisticated radiative transfer models (e.g., [Verhamme et al., 2006](#); [Gronke et al., 2015](#)).

Non-resonant lines provide a valuable alternative, although the signals are notably weaker. Commonly seen optical nebular lines from H II regions include optical recombination lines such as the hydrogen Balmer series (H $\alpha$   $\lambda$  6564, H $\beta$   $\lambda$  4862, and higher-order lines), as well as “forbidden” lines such as [O II]  $\lambda\lambda$  3727, 3729, [N II]  $\lambda\lambda$  6549, 6585, and [O III]  $\lambda\lambda$  4960, 5008. In particular, the hydrogen Balmer series, produced by electron transitions between the  $n = 2$  state and the higher orbits of neutral hydrogen atoms, also serves as a good tracer of the total baryon content. Similar to Ly $\alpha$ , the anticipated H $\alpha$  emissivity of ionized nebulae is  $j_{\text{H}\alpha} = (h\nu_{\text{H}\alpha}/4\pi) C \langle n_{\text{H}} \rangle^2 \alpha_{\text{H}\alpha}^{\text{eff}}$  with a corresponding surface brightness of  $\text{SB}_{\text{H}\alpha} \approx 2 \times 10^{-15} (l_{\text{neb}}/1 \text{ kpc}) C \langle n_{\text{H}} \rangle^2 / (1+z)^4 \text{ erg s}^{-1} \text{ cm}^{-2} \text{ arcsec}^{-2}$  for  $\alpha_{\text{H}\alpha}^{\text{eff}} \approx 1.17 \times 10^{-13} \text{ cm}^3 \text{ s}^{-1}$  at  $T \approx 10^4 \text{ K}$  (e.g., [Draine, 2011](#)). Although the anticipated H $\alpha$  signals are nearly ten times fainter than Ly $\alpha$ , these photons are not strongly coupled with the gas along the line of sight and provide a robust record of the underlying gas density and velocity. The challenge associated with an inherently fainter signal from H $\alpha$  can be mitigated by targeting gaseous halos at lower redshifts where the effect of cosmological surface brightness dimming is significantly smaller (e.g., [Lokhorst et al., 2019](#)).

In addition to hydrogen, metal ions in diffuse ionized nebulae are known to be crucial in regulating the thermal state of the gas by acting as effective coolants (e.g., [Osterbrock and Ferland, 2006](#); [Draine, 2011](#)). These ions, due to their complex electron orbit configurations, possess several low-energy states. Collisional excitation of electrons between these states followed by radiative decay allows energy to be efficiently dissipated with the released photons. The so-called “forbidden” transitions occur in these metal ions when transitions between energy levels have a very low probability. As a result, the released photons from these forbidden emission lines can escape, leading to gas cooling. Such cooling radiation expected of diffuse ionized gas provides additional tracers of gaseous halos around galaxies.

Indeed, observations of galaxies and quasars at  $z \lesssim 1$ , targeting these optical nebular lines have uncovered extended emission signals far beyond previously known luminous star-forming regions (e.g., [Epinat et al., 2018](#); [Rupke et al., 2019](#); [Johnson et al., 2024](#)). Simultaneous observations of both hydrogen recombination lines and metal lines offer the additional advantage of constraining the underlying gas density, ionization condition, metallicity, and temperature based on the relative line ratios (e.g., [Baldwin et al., 1981](#); [Kewley et al., 2019](#)). An example is displayed in the *bottom* panels of Fig. 4, showcasing a giant intragroup nebula detected in multiple nebular lines, including [O II], H $\beta$ , [O III], and [N II], in addition to H $\alpha$  ([Chen et al., 2019](#)). The emission signals span  $\approx 100 \text{ kpc}$  in diameter, revealing gaseous streams connecting different members of the galaxy group. The detections of multiple nebular lines enable a detailed study of the ionization state of the gas using the Baldwin, Phillips, & Terlevich (BPT) diagram ([Baldwin et al., 1981](#)). For photo-ionized gas in star-forming regions, the line ratios are found to follow a relatively tight sequence from top-left to bottom right (solid curve from [Kauffmann et al., 2003](#)), while the presence of AGN or shocks elevate the ionization state of metal ions leading to enhanced signals of “forbidden” lines relative to hydrogen (to the right of the dotted curve in the BPT diagram from [Kewley et al. 2001](#)). In this case, a lack of AGN signatures in the group members, coupled with the emission morphology of the nebulae, supports a scenario in which the gas is shock-heated by the tidally stripped gaseous streams moving across the unseen hot intragroup medium. This example highlights how dynamic effects due to galaxy interactions can be effective in releasing metal-enriched gas from star-forming regions in the absence of galactic superwinds (see also [Fossati et al., 2016](#), for examples of gas stripping in nearby galaxy clusters).

Expanding observations of extended nebular emissions to lower-mass halos remains a significant challenge due to the faintness of the signals. Progress is being made by stacking narrow-band images targeting nebular emission lines across hundreds of sources. These efforts are beginning to shed light on the extended gas around galaxies with stellar mass as low as  $M_{\text{star}} \approx 10^8 M_{\odot}$ . For example, enhanced Mg II emission signals are detected out to 10 kpc along the polar axis in stacked images of edge-on galaxies at  $z \approx 1$  (e.g., [Guo et al., 2023](#)), revealing the role of galactic outflows in the metal transport around distant star-forming galaxies. Beyond the disks, the extent of detected nebular signals increases with increasing  $M_{\text{star}}$  in the stacked images (see the two *top-right* panels of Fig. 4, adapted from [Dutta et al., 2024](#)). While stacked narrow-band images offer a global view of extended nebulae around galaxies across a wide mass range, detailed studies of individual halos are essential to characterize the physical conditions of the gas and understand their relationship with the galaxies’ star formation histories.

### 3.2 Absorption spectroscopy

Absorption spectroscopy complements emission surveys by offering a sensitive tool for investigating diffuse, large-scale baryonic structures in the distant Universe (e.g., [Rauch 1998](#); [Wolfe et al. 2005](#)). As illustrated in Fig. 3, photons emitted by a background source interact with the material along the line of sight, resulting in distinct absorption features in the spectrum of the background source. Distant quasars have long been used to illuminate and study the diffuse gas content between the quasar and the observer, providing valuable insights into the low-density IGM and CGM properties. The strengths of these absorption features are dictated by the physical conditions of the gas, including gas density, temperature, ionization state, and metallicity. By analyzing these absorption spectra, astronomers can uniformly survey the diffuse cosmic gas structure over the vast range in density and temperature predicted by simulations (see Fig. 2).

An example of a typical optical spectrum of distant quasars is shown in Figure 5. At redshift  $z_{\text{QSO}} = 2.14$ , this quasar displays prominent broad emission lines from Ly $\alpha$ , Si IV, C IV, and C III (e.g., [Vanden Berk et al., 2001](#)), all redshifted to the optical spectral window. Notably,

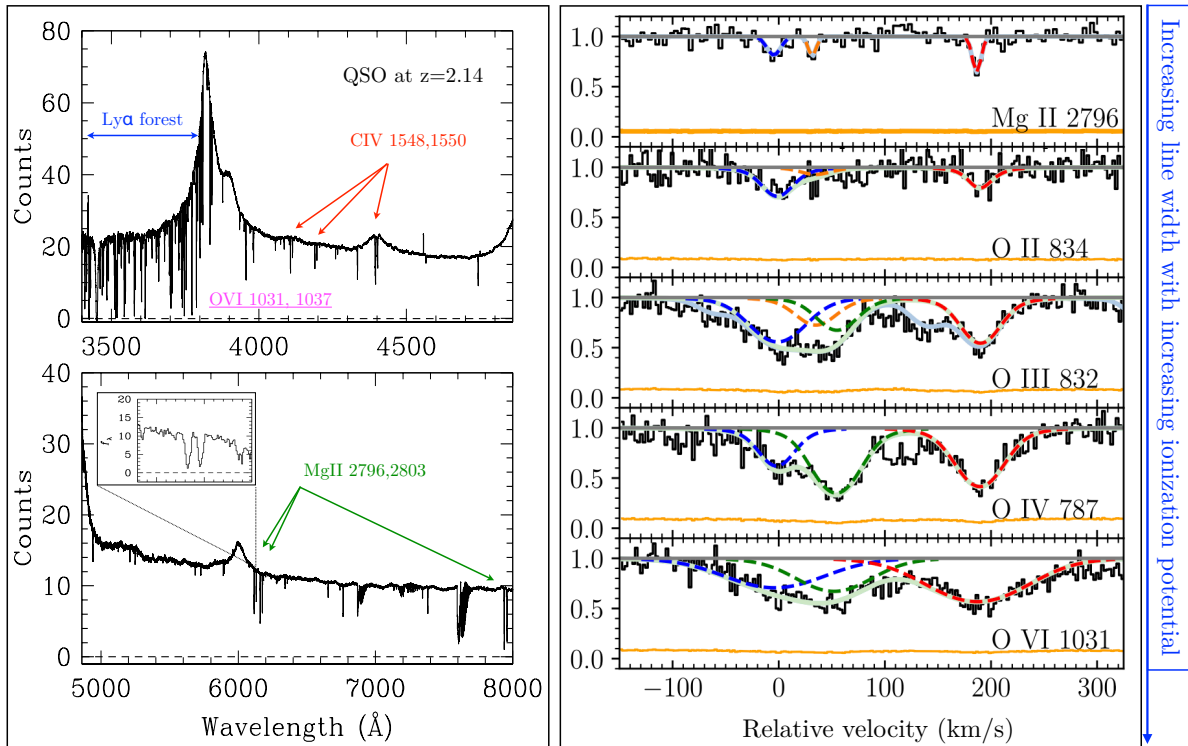


**Fig. 5** Quasar absorption spectroscopy provides a sensitive probe to uncover a wealth of information for diffuse multiphase gas in the galactic atmosphere, including gas density, temperature, ionization state, and kinematics, otherwise inaccessible to astronomers. The *left* column displays a typical optical spectrum of a distant quasar at  $z=2.14$ . In addition to broad emission lines intrinsic to the quasar, such as  $\text{Ly}\alpha$  and  $\text{N V}$  at  $\approx 3800 \text{ \AA}$ , a forest of  $\text{Ly}\alpha$  absorption lines is observed blueward of  $3800 \text{ \AA}$ , revealing overdense regions spanning over ten decades in neutral hydrogen column densities  $N_{\text{HI}}$  at  $z_{\text{abs}} < z_{\text{QSO}}$  along the line of sight. Many of the stronger  $\text{Ly}\alpha$  absorbers are accompanied with metal absorption transitions such as the  $\text{O VI } \lambda\lambda 1031, 1037$  doublet transitions, and the  $\text{C IV } \lambda\lambda 1548, 1550$  and  $\text{Mg II } \lambda\lambda 2796, 2803$  doublets (shown in the inset of the *bottom-left* panel). Together, the relative strengths between different ionic lines place strong constraints on the ionization state and chemical enrichment of the gas. In addition, high-resolution absorption spectra provide additional power to resolve multiphase gas based on the observed line profiles. In particular, the absorption line widths of individual ions, typically described by the Doppler parameter  $b_l$  to quantify the line-of-sight velocity dispersion, are often found to increase with the ionization potential (I.P.) of the ion. An example is displayed in the *right* panels, which demonstrate the progression of broader linewidths of oxygen ions at higher ionization stages (adapted from Cooper et al., 2021). The correlation between line width and ionization potential remains when incorporating all available lines from hydrogen, carbon, and oxygen through iron (e.g., Qu et al., 2022). Because different particles at different ionization stages are expected to occur in different temperature and density phases (see Fig. 2), the observed increasing line width with increasing ionization stages provides an independent confirmation for the presence of multiphase gas in the galactic atmosphere (see also Liang et al., 2016; Kumar et al., 2024).

the  $\text{Ly}\alpha$  forest appears blueward of the  $\text{Ly}\alpha$  emission line at  $4800 \text{ \AA}$ , consisting of numerous  $\text{Ly}\alpha \lambda 1215$  absorption lines of varying strengths caused by intervening overdense regions along the QSO sightline at  $z_{\text{abs}} \lesssim z_{\text{QSO}}$  (see also Fig. 3). The degree of flux attenuation in each absorption line quantifies the total gas mass in these intervening regions, following the relation  $-\ln(f_{\text{obs}}/f_{\text{intrinsic}}) = N_{\text{HI}} \sigma_{\text{Ly}\alpha}$ . Here  $N_{\text{HI}}$  is the HI column density (the number of neutral hydrogen atoms per unit area) and  $\sigma_{\text{Ly}\alpha} = 3.3 \times 10^{-14} \text{ cm}^2$  is the absorption cross-section of  $\text{Ly}\alpha$  photons at  $T \approx 10^4 \text{ K}$ . For a cloud of density  $n_{\text{H}} \approx 0.01 \text{ cm}^{-3}$  and size  $100 \text{ pc}$ , typical of the cool gas seen in the Milky Way Halo (e.g., Putman et al., 2012), a neutral fraction of 1% would lead to  $N_{\text{HI}} \approx 3 \times 10^{16} \text{ cm}^{-2}$ . The large absorption cross-section indicates that even a small fraction of neutral hydrogen particles in these clouds would lead to saturated  $\text{Ly}\alpha$  absorption lines. At the same time, the  $\text{Ly}\alpha$  forest spectrum reveals a vast range of  $N_{\text{HI}}$ , from  $N_{\text{HI}} \gtrsim 10^{20} \text{ cm}^{-2}$  resembling neutral interstellar matter, to  $N_{\text{HI}} \lesssim 10^{13} \text{ cm}^{-2}$  in the IGM, with the majority the lines showing  $N_{\text{HI}} \lesssim 10^{16} \text{ cm}^{-2}$  (e.g., Rauch, 1998). The  $N_{\text{HI}}$  distribution function of the  $\text{Ly}\alpha$  forest (e.g., Ribaldo et al., 2011) provides the clearest indication yet for a highly ionized IGM and CGM (e.g., Gunn and Peterson 1965, see also Rauch 2000 for a review).

A significant fraction of  $\text{Ly}\alpha$  absorbers with  $N_{\text{HI}} > 10^{14} \text{ cm}^{-2}$  also exhibit associated metal absorption lines, indicating that the gas has been enriched with metals (e.g., Cowie et al., 1995; Schaye et al., 2000). The most prominent metal absorption features include the  $\text{O VI } \lambda\lambda 1031, 1037$  doublet transitions within the  $\text{Ly}\alpha$  forest, as well as the  $\text{C IV } \lambda\lambda 1548, 1550$  and  $\text{Mg II } \lambda\lambda 2796, 2803$  doublets. Additionally, there is a series of low-ionization transitions such as  $\text{C II}$ ,  $\text{Si II}$ , and  $\text{Fe II}$  (e.g., Becker et al., 2015; Dey et al., 2015). These doublet transitions arise from lithium-like ions with two closely spaced fine-structure levels above the ground state. Their fixed doublet ratios, determined by the transition probabilities between the ground state and these fine-structure levels, along with precise transition wavelengths, significantly enhance the reliability of their identification (see the inset in the *lower-right* panel of Fig. 5).

The presence of metals in the diffuse CGM and IGM presents one of the greatest puzzles in modern astrophysics because elements heavier than lithium are primarily formed in stellar interiors (e.g., [Nomoto et al., 2013](#)). Transporting these heavy elements from star-forming regions on parsec scales into the gaseous halos on scales of 100 kpc and beyond over the final lifetime of the Universe would require ultra-high-speed winds from stars and supermassive black holes (SMBHs). While supergalactic winds are seen in some nearby galaxies (e.g., [Veilleux et al., 2005](#)), the extent of the signals reaches  $\approx 10\text{--}20$  kpc, far smaller than the cosmological distance required to explain the amount of metals seen beyond star-forming regions (e.g., [Scannapieco et al., 2002](#); [Peeples et al., 2014](#), see also [Fig. 1](#)). The typical size of metal-enriched halos,  $r_Z$ , necessary to explain the observed number density,  $n(z)$ , of metal absorbers per unit redshift interval per line of sight, can be estimated following a halo cross-section weighted space density of galaxies,  $n(z) = (c/H_0) E(z) \int_0^\infty \Phi(L, z) \pi r_Z^2(L) \kappa dL$ , where  $c$  is the speed of light,  $H_0$  is the Hubble constant, representing the current expansion rate of the Universe,  $L$  is the intrinsic luminosity of galaxies in the unit of the characteristic luminosity  $L_*$ ,  $\Phi(L, z)$  is the galaxy luminosity function describing the number density of galaxies per unit comoving volume per luminosity interval,  $\kappa$  is the covering fraction of metal-enriched gas in the halo, and  $E(z) \equiv (1+z)^2 / \sqrt{\Omega_M(1+z)^3 + \Omega_\Lambda}$  accounts for the cosmological expansion of the cosmos. Here, it is assumed that more luminous galaxies are on average more massive and possess larger chemically enrichment halos (e.g., [Tinker and Chen, 2008](#)), which is supported by empirical observations (e.g., [Chen et al., 2010](#); [Churchill et al., 2013](#)). Owing to the success of numerous deep galaxy surveys, the galaxy luminosity functions are well determined over a broad redshift range and star formation histories (e.g., [Behroozi et al., 2019](#)), and the expected size of metal-enriched halo from the observed number density of metal absorbers along random quasar sightlines exceeds 100 kpc for  $\kappa = 50\%$  (e.g., [Chen et al., 2017b](#)).

Irrespective of the physical processes that drive the chemical enrichment in underdense regions, the presence of metal absorption lines in the Ly $\alpha$  forest provides valuable diagnostics for the underlying physical and thermodynamic conditions of the gas (e.g., [Verner et al., 1994b](#); [Rauch et al., 1997](#); [Gnat, 2017](#)). As noted in [Section 2](#) and [Fig. 2](#), each heavy element offers multiple ionization stages, and higher ions are expected to be more dominant in warmer and lower-density CGM. The ionization state of a photoionized gas is commonly described by a single ionization parameter,  $U$ , which represents the number of incident ionizing photons per hydrogen atom. For a given radiation field characterized by a total flux of hydrogen-ionizing photons,  $\phi$ , with energy  $\geq 13.6$  eV, the  $U$  parameter is inversely proportional to the hydrogen number density,  $n_H$ , following the relation  $U \equiv \phi/c n_H$ . A higher  $U$  corresponds to a more highly ionized gas and an increased abundance of highly ionized species. Therefore, the observed ion ratios place constraints on  $U$ , and the gas density,  $n_H$ , can be inferred by assuming a fiducial ionizing spectrum (e.g., [Haardt and Madau, 2012](#); [Khairi and Srianand, 2019](#); [Faucher-Giguère, 2020](#)). Consequently, the relative abundances of different ions provide direct constraints on the gas density and ionization conditions (see e.g., [Chen et al., 2017a](#)).

In addition, the observed absorption line width, traditionally described by the Doppler parameter,  $b$ , directly measures the velocity distribution of particles within the absorbing cloud along the line of sight. The Doppler velocity width measures the particles' average relative line-of-sight velocity offset and is related to the velocity dispersion following  $b = \sqrt{2} \sigma_v$ . For pure thermal motions, the velocity dispersion reflects the gas temperature and the thermal  $b_{\text{th}}$  value is expected to be  $b_{\text{th}} = \sqrt{2k_B T/m_i}$ , where  $k_B$  is the Boltzmann constant and  $m_i$  is the mass of the ions. Therefore, it follows that under pure thermal broadening, absorption features originating in warmer gas would appear broader, while transitions from heavier ions would appear narrower. At the same time, the diffuse absorbing clouds in the CGM and IGM are part of a dynamic system characterized by a mixture of coherent flows and chaotic turbulence. These bulk motions can contribute significantly to the observed line widths in absorption spectra. All particles, regardless of their mass, are influenced by these motions, resulting in a constant non-thermal component,  $b_{\text{nt}}$ , in the observed line width. Therefore, the total observed line width,  $b_{\text{obs}}$ , is the result of both thermal and non-thermal broadening effects and can be expressed as  $b_{\text{obs}} = \sqrt{b_{\text{th}}^2 + b_{\text{nt}}^2} = \sqrt{2k_B T/m_i + b_{\text{nt}}^2}$ . Comparing the observed line widths of two ions with significantly different masses enables astronomers to disentangle the contributions of thermal and bulk flows, thereby providing robust constraints on the gas temperature and the magnitude of non-thermal motions within the absorbing structure (e.g., [Rauch et al., 1996](#); [Rudie et al., 2019](#)).

Observations have frequently shown that heavier ions produce narrower absorption line widths compared to lighter ions. For instance, [Fig. 5](#) highlights a narrower Mg II absorption line relative to the corresponding O II feature (top two right panels). Additionally, the line widths of oxygen ions increase with ionization potential,  $E_i$ . Generally, ions with ionization potentials  $E_i > 20$  eV show on average broader line widths ( $b_{\text{obs}} \gtrsim 20 \text{ km s}^{-1}$ ), while lower ionization states tend to exhibit narrower line widths ( $b_{\text{obs}} \lesssim 10 \text{ km s}^{-1}$ ; e.g., [Cooper et al. 2021](#); [Qu et al. 2022](#)). This correlation between line width and ionization potential aligns with expectations of thermal broadening, as higher-ionization species trace warmer, lower-density gas (e.g., [Fig. 2](#)).

By analyzing both the relative absorption strengths and velocity widths of ions across different ionization states and different masses, strong constraints can be placed on the physical and thermal properties of the absorbing gas. Therefore, absorption spectroscopy provides a powerful tool for characterizing the underlying structure and dynamics of diffuse multiphase gas.

## 4 Known empirical properties of the multiphase CGM

Quasar absorption spectroscopy has long been a powerful tool for obtaining detailed insights into the diffuse, multiphase CGM (e.g., [Tumlinson et al., 2017](#); [Chen, 2017](#), for reviews). These studies typically utilize detailed background quasars to probe the gas associated with galaxies along the line of sight, with absorption features revealing the properties of their extended atmosphere. However, due to the rarity of luminous quasars—approximately one bright quasar ( $g \lesssim 18$  mag) per square degree (e.g., [Richards et al. 2006](#))—these investigations have been largely restricted to a single probe per galaxy, particularly for galaxies beyond the local universe (see [Richter et al., 2017](#); [Lehner et al., 2020](#); [Zheng et al., 2020](#), for studies of the Milky Way, M31, and Local Group dwarfs). While multiply-lensed quasars offer an

exciting avenue for expanding these studies from one-dimensional to two-dimensional mapping, the number of available systems remains limited (e.g., Rauch et al. 2001; Chen et al. 2014; Zahedy et al. 2016; Rubin et al. 2018; see also Lopez et al. 2018 for an example of using a highly-magnified distant galaxy as multiple probes). Nonetheless, even with one quasar per halo, statistical studies employing a large sample of quasar-galaxy pairs allow astronomers to establish a global understanding of the diffuse CGM based on ensemble averages.

#### 4.1 Global distributions

As a first step, strong constraints on the spatial properties of the galactic atmosphere can be derived using a sample of galaxy and quasar pairs that span a range in projected separations ( $d$ ). By analyzing the absorption features imprinted in the spectra of background quasars, observers can examine the incidence and total absorption strengths of different species as a function of distance from the associated galaxies (Fig. 6). Despite being an ensemble average over many galaxies, these spatial profiles serve as a baseline characterization for the changing ionization condition and chemical enrichment in the galactic atmosphere. Investigating how these profiles vary with the galaxy mass, star formation history, and environments provides key insights into the origin and primary drivers that dictate the physical state of the gas.

For example, the observed integrated column density profiles as a function of projected distance for different atomic species offer the first look at the extent of gas around galaxies through different tracer particles. The *left* panels of Fig. 6 display the current empirical understanding of the extended HI and O VI gaseous envelopes around galaxies of  $\log M_{\text{star}}/M_{\odot} \gtrsim 9.5$ . As described in Section 3, the sizes of the gaseous atmosphere are expected to scale with halo mass (see e.g., Chen et al., 2010; Churchill et al., 2013), normalizing the projected distance by the virial radius of the halo  $R_{\text{vir}}$  removes this intrinsic mass scaling and places all galaxies of different masses on the same scale. Low ionization state species such as HI display a more rapidly declining profile with increasing distance than more highly-ionized species such as O VI from galaxies. The data points included in the panels are based on a collection of literature samples (see Qu et al., 2024, for a detailed description). Observations of additional low ions around galaxies of a wide range of star formation histories, such as Mg II, C II, and Si II, can be found in Chen et al. (2010), Werk et al. (2014), Liang and Chen (2014), and Huang et al. (2021).

The apparent difference in the projected column density profiles of HI and O VI reveals that these two species do not generally occupy the same regions within a galaxy halo. This discrepancy underscores the importance of targeting a suite of ions to develop a comprehensive and robust characterization of gaseous halos. Each ion traces gas in different ionization states and densities, meaning that no single ion can capture the full complexity of the halo. In addition, the observed differences between ions in various ionization stages point to varying ionization conditions across the halo. These spatial ionization profiles serve as key observables, helping to distinguish between competing theoretical models. Comparisons between simulations with and without cosmic ray (CR) feedback have indeed shown that models incorporating CR feedback better capture the large-scale distributions of both HI and O VI around star-forming galaxies (Ji et al. 2020; blue versus orange curves in Fig. 6). While the success suggests cosmic ray feedback may be a dominant driver in regulating the diffuse halo gas, it is not the only successful model. Other mechanisms, including AGN feedback, have also been shown to explain the observed column density profiles well (e.g., Oppenheimer et al., 2016; Nelson et al., 2018). Additional observables are therefore necessary to improve the discriminating power.

In addition to comparing the spatial profiles of different species, a clear feature in the observations that has not been accounted for is the presence of non-detections at  $d < R_{\text{vir}}$ . These sightlines pass through regions with particularly low densities of absorbing materials in galaxy halos, indicating a patchy distribution of these materials, particularly metal-enriched gas. Therefore, investigating how the mean covering fraction of metal-enriched gas changes with halo mass provides further insight into how halo gas properties are coupled with halo growth. Observations show that the covering fraction of chemically-enriched, photoionized gas traced by Mg II varies with both galaxy mass and star formation history, from  $\langle \kappa \rangle_{\text{MgII}} \approx 80\%$  in Milky-Way like star-forming halos to  $\langle \kappa \rangle_{\text{MgII}} \approx 20\%$  in massive halos hosting luminous red galaxies (*top-right* panel of Fig. 6). These luminous red galaxies (LRGs) resemble nearby elliptical galaxies with little ongoing star formation (e.g., Eisenstein et al., 2001) and represent a homogeneous sample of massive quiescent systems.

Examining the mean absorption properties of highly ionized species provides additional clues. This is shown in the *lower-right* panel of Fig. 6, which presents the mean O VI column density,  $\langle N(\text{OVI}) \rangle_{R_{\text{vir}}}$ , for various mass bins. The mean O VI column density per mass bin is an integral of the product of  $N(\text{OVI})$  and covering fraction across the projected area within the halo radius,  $\langle N(\text{OVI}) \rangle_{R_{\text{vir}}} = \int_0^{R_{\text{vir}}} N(\text{OVI}, d) \kappa_{\text{OVI}}(d) 2d \delta d / R_{\text{vir}}^2$ . For a flat column density profile that reaches a maximum of  $N_0$  (*lower-left* panel of Fig. 6), the observed mean column density translates to a mean gas covering fraction following  $\langle N(\text{OVI}) \rangle_{R_{\text{vir}}} = N_0 \langle \kappa \rangle_{\text{OVI}, R_{\text{vir}}}$ . Surveys of O VI-bearing CGM have uncovered  $\log N_0/\text{cm}^{-2} \approx 14.7$  for Milky-Way like star-forming halos, while  $\log N_0/\text{cm}^{-2} \approx 14.0$  for massive quiescent galaxies (see Tumlinson et al., 2011; Qu et al., 2024). At the same time,  $\log \langle N(\text{OVI})/\text{cm}^{-2} \rangle_{R_{\text{vir}}}$  is found to be  $\approx 14.5$  in halos of  $M_{\text{star}} \approx 10^{10} M_{\odot}$  and  $\approx 13.6$  in halos of  $M_{\text{star}} \approx 10^{11} M_{\odot}$ , indicating a rapidly declining  $\langle \kappa \rangle_{\text{OVI}, R_{\text{vir}}}$  with increasing mass. Different from Mg II-bearing gas, however, the mean O VI column density also shows a notable decline to  $\langle \log N_{\text{OVI}}/\text{cm}^{-2} \rangle \approx 13.8$  around low-mass dwarf galaxies (e.g., Qu et al., 2024). The observed decline in both  $\langle \kappa \rangle_{\text{MgII}}$  and  $\langle \kappa \rangle_{\text{OVI}}$  can be attributed to either a lack of starburst outflows in massive quiescent galaxies, a higher destruction rate of CGM clumps in massive halos, or a combination of both factors.

A key distinguishing feature of starburst-driven outflows is their non-spherical distribution in the halos of galaxies with well-formed, star-forming disks (e.g., Veilleux et al., 2005). Galactic-scale outflows are expected to travel preferentially along the polar axis where the gas experiences the least resistance, while accretion of the IGM is likely to proceed along the disk plane (e.g., Shen et al., 2013; Schneider et al., 2020). The expectation that metal absorption strengths would be enhanced along the polar axis of galaxies, if outflows predominantly drive metals, is complicated by the realities of the CGM. For example, the M81 group (Fig. 1) presents a case where stripped gas, inflows, and outflows mix in a way that doesn't align neatly with the major-minor axis distinction. Instead, the chaotic distribution of diffuse gas emission signals suggests that the interplay of multiple processes complicates our ability to isolate outflows based solely on the axis orientation. Observational studies on CGM absorption in disk galaxies have also yielded mixed results. While some observations show



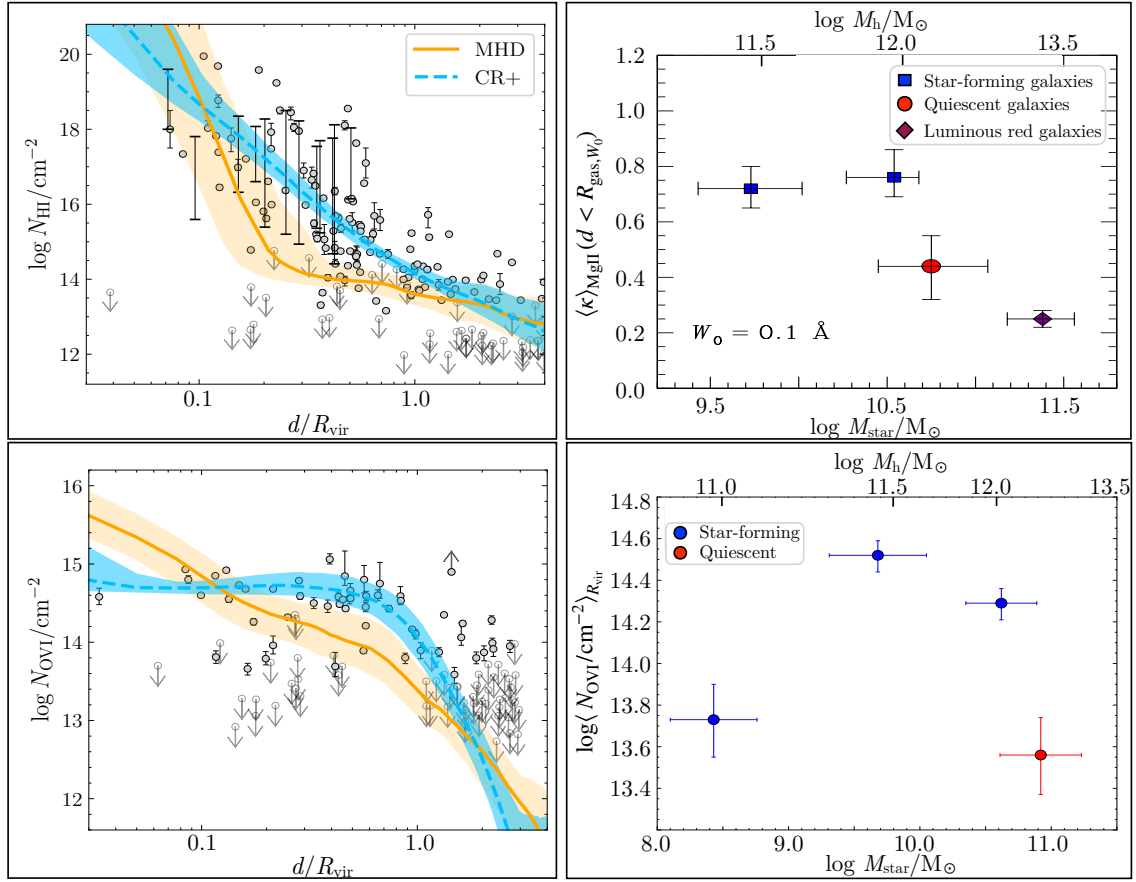


**Fig. 6** Empirical knowledge of the spatial distribution of multiphase gas in the galactic atmosphere from ensemble studies utilizing absorption spectroscopy. Using a sample of close galaxy and quasar pairs, strong constraints on the spatial properties of gaseous halos can be established based on the absorption strength imprinted in the spectrum of the background quasars. The data points in the *left* panels are compiled from a collection of literature samples for galaxies with stellar mass exceeding  $\log M_{\text{star}}/M_{\odot} = 9.5$  (e.g., Qu et al., 2024). The column densities of low ionization state species such as HI steadily decline with increasing projected distance from galaxies. In contrast, highly ionized species such as O VI display a flatter projected column density profile. The blue and orange curves are predictions from magnetohydrodynamic (MHD) simulations and simulations incorporating cosmic ray (CR) feedback, with the bands representing the 68% interval around the median values (adapted from Ji et al., 2020). In addition to the radial profiles of different atomic species in gaseous halos, an important observation is a non-unity covering fraction of these species, as indicated by the non-detections with downward arrows in the *left* panels. The *upper-right* panel displays the mean covering fraction of Mg II absorber with rest-frame absorption equivalent width greater than  $W_0 = 0.1 \text{ \AA}$  within a fiducial gaseous  $R_{\text{gas}}$ . A general declining trend is seen with increasing mass and reduced star formation activities over the galaxy population (e.g. Huang et al., 2021). A reduced covering fraction would translate directly to a reduced mean absorption column density. This is seen in the *lower-right* panel for the observed mean O VI column density, which declines from  $\log(N(\text{OVI})/\text{cm}^{-2}) \approx 14.5$  in halos of  $\log M_{\text{star}}/M_{\odot} \approx 9.7$  to  $\log(N(\text{OVI})/\text{cm}^{-2}) \approx 13.6$  in halos of  $\log M_{\text{star}}/M_{\odot} \approx 11$  (e.g., Qu et al. 2024; see also Zahedy et al. 2019, Tchernyshyov et al. 2022). The observed partial covering of different species as a function of galaxy mass and star formation history provides independent constraints for the baryon cycle in the galactic atmosphere.

enhanced metal absorption along the polar axes (e.g., Bordoloi et al. 2011, and recall such anisotropic distribution of metal-enriched gas detected in emission from Guo et al. 2023), consistent with outflow-driven models, others have found more isotropic distributions or stronger absorption along the galaxy’s plane (e.g., Martin et al., 2019). This discrepancy may result from differences in galactic environments and/or measurement uncertainties. To establish a comprehensive understanding of the diffuse galactic atmosphere, it is necessary to go beyond a simple cross-section analysis and spatially and spectrally resolve detailed physical properties of the multiphase gas. While this is still challenging with current facilities (see Section 5), significant progress has been made with spectrally resolved absorption-line studies.

## 4.2 Resolved density, size, and metallicity structures

In recent years, high-resolution absorption spectroscopy of the diffuse CGM has enabled astronomers to resolve small-scale features in galaxy halos and examine how the complex multiphase gas physics on small scales is influencing galaxy growth. Recall that the observed line width is characterized by the Doppler velocity width,  $b_{\text{obs}} = \sqrt{2} \sigma_v$  and both thermal and non-thermal motions contribute to the ob-

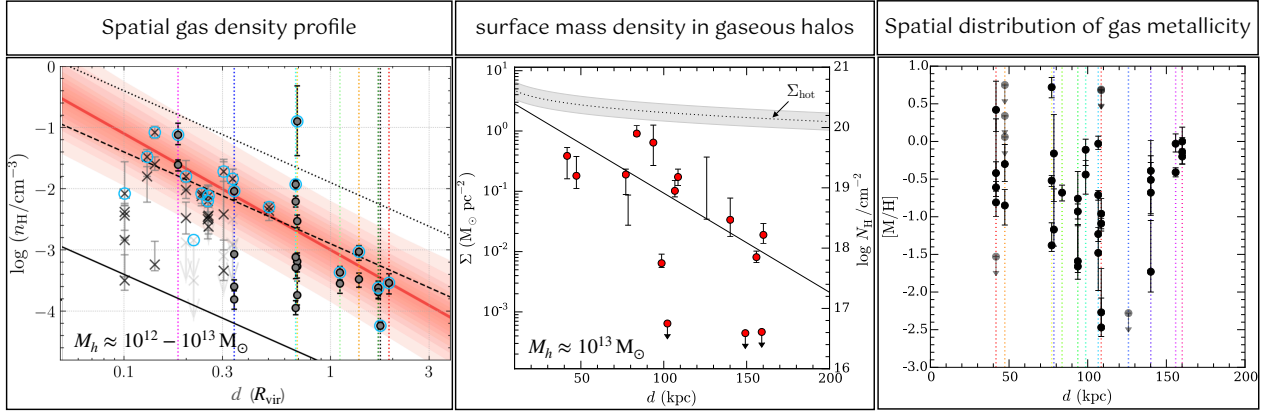


**Fig. 7** Global density (pressure), mass, and chemical enrichment profiles established for the diffuse galaxy halos at  $z \lesssim 1$  from absorption-line observations. The *left* panel shows the density fluctuations resolved in absorption spectroscopy for the cool gas of temperature  $T \sim 10^4$  K along individual sightlines (data points connected by a vertical, dotted line) as a function of projected distance in units of halo radius  $R_{\text{vir}}$  (adapted from Qu et al. 2023; see also Zahedy et al. 2019). The large dispersion in gas density between resolved clumps can be understood by the projection effect of different clumps at different radii intercepted by each quasar sightline. Such an explanation is supported by the gradual decline of the upper envelope of the density distribution (red curves), with quasar sightlines at large  $d$  probing the low-density outskirts of galaxy halos. It is also consistent with the density profile inferred for the hot phase (black solid line; e.g., Li and Bregman, 2017; Singh et al., 2018). With a typical temperature of  $T \sim 10^4$  expected for the cool photoionized gas and  $T \sim 10^6$  K for the hot medium, the observed factor of  $\sim 100$  difference in the global density profiles between the two phases suggests that the galactic atmosphere is in a quasi-equilibrium pressure balance, following the ideal gas law  $P = n_{\text{H}}k_{\text{B}}T$  (see e.g., Fig. 2). Independent of the adopted scenario to explain the observed scatter in cool gas density, the observed density distributions over an ensemble of halos translate directly to the mean gas surface mass density in the cool phase. The *middle* panel shows a comparison between the inferred surface mass density profiles of the cool (red circles and solid line) and hot ( $T \gtrsim 10^6$  K; dotted curve) CGM of high-mass quiescent galaxies from Zahedy et al. (2019), showing a diminishing presence of cool gas toward the outskirts of these massive halos. For massive galaxies residing in halos with  $M_h \approx 10^{13} M_{\odot}$ , the vast majority ( $\gtrsim 90\%$ ) of the mass of the CGM resides in the hot phase. Similar to gas density, the inferred gas metallicity in the cool CGM also exhibits a large scatter (*right* panel, reproduced from Zahedy et al. 2019; see also Zahedy et al. 2021; Cooper et al. 2021; Kumar et al. 2024). Measurements of gas clouds identified along a single sightline are connected by a vertical dotted line to guide the visual inspection. The wide range of metallicities seen in the CGM of individual galaxies underscores the complex chemical enrichment history in individual galaxy halos.

served line broadening. For a fiducial gas temperature of  $T \sim 10^4$  K, the expected thermal line width is  $b_{\text{th}} = \sqrt{2k_{\text{B}}T/m_1} \approx 12.9 \text{ km s}^{-1}$  for hydrogen, which translates to a required spectral resolution in velocity of full-width-at-half-maximum ( $\text{FWHM}_{\nu}$ )  $\approx 20 \text{ km s}^{-1}$  to resolve individual hydrogen components and  $\text{FWHM}_{\nu} \approx 6 \text{ km s}^{-1}$  for heavier ions in the absence of bulk motions. The recent progress in resolved component studies is enabled by combining optical echelle spectroscopy on large ground-based telescopes with high-resolution far-ultraviolet spectra obtained using the *Hubble Space Telescope* to cover a large number of elements in different ionization stages expected in the diffuse multiphase gas (e.g., Fig. 2; see also Verner et al. 1994b) and to provide the maximal dynamic range in particle mass for decomposing the multiphase components.

An example is shown in Fig. 5, where an absorption system is resolved into four distinct components within a line-of-sight velocity interval of  $\approx 200 \text{ km s}^{-1}$  (highlighted in blue, orange, green, and red from 0 to  $\approx +200 \text{ km s}^{-1}$  in relative velocities). While all four components exhibit progressively broader velocity widths with increasing ionization stages of oxygen ions as noted in Section 3.2, the corresponding Mg II components are notably narrower than O II, a lighter element sharing a similar ionization potential, indicating that the observed line widths of these low-ionization species are driven by thermal motions with a relatively cool phase of  $T \approx 10^4$  K. The broader widths observed in O III and O IV suggest the presence of a warmer phase. Indeed a spectrally-resolved photoionization analysis showed that these intermediate ions likely originate in low densities of  $\log n_{\text{H}}/\text{cm}^{-3} \approx -3.9$ , while the lower ions trace higher-density regions of  $\log n_{\text{H}}/\text{cm}^{-3} \approx -2.3$  (Cooper et al., 2021). The much broader line widths observed in O VI indicate the presence of a third phase at a significantly higher temperature of  $T \gtrsim 10^6$  K in at least three of the four components. This example illustrates how a careful analysis of the absorption profiles of different ions allows astronomers to deblend and decompose multiphase gas, although the connections between these phases remain uncertain. While the matching velocity centroids between the cool and warm phases observed in the blue and red components suggest that they share the same density structures with the warm phase arising in the interface between the dense core and the ambient hot halo, it is also possible that the warm phase arises in a physically distinct region, likely in the halo outskirts, along the line of sight (see the cartoon illustration in Fig. 2).

Spectrally-resolved photoionization analyses of the multiphase CGM have uncovered remarkable insights into its complex structure (e.g. Zahedy et al., 2019, 2021; Cooper et al., 2021; Kumar et al., 2024). A common feature is the detection of multiple clumps along each sightline with a characteristic density of  $n_{\text{H}} \sim 10^{-2} \text{ cm}^{-3}$ , while a large spread of nearly two orders of magnitude between clumps is also observed (*left* panel of Fig. 7). Such a large dispersion in gas density can be understood as the result of the projection effect, where quasar

sightlines pass through clumps located at different distances from the galaxy center (e.g., Zahedy et al., 2019; Voit et al., 2019; Qu et al., 2023). The general trend shows that closer sightlines encounter gas across a broad range of densities, while those probing the outer CGM uncover mostly lower-density gas. This physical picture is corroborated by the observed general decline in the upper envelope of the density profile. Moreover, this explanation is also consistent with the inferred density profile of hot CGM (black solid line; e.g., Li and Bregman, 2017; Singh et al., 2018). With typical temperatures of  $T \sim 10^4$  K for the cool CGM gas (see Section 2) and  $T \sim 10^6$  K expected for the hot medium, the observed factor of  $\sim 100$  difference in the global density profiles between the two phases suggests that the CGM is in roughly in thermal pressure equilibrium, following  $n_{\text{H}}^{\text{cool}} T_{\text{cool}} \approx n_{\text{H}}^{\text{hot}} T_{\text{hot}}$ . However, the data are sufficiently noisy that the presence of non-pressure support in the multiphase gas from the magnetic field and cosmic rays cannot be ruled out (e.g., Ji et al., 2020; Ruszkowski and Pfrommer, 2023), particularly for the intermediate phase with a possible origin in the boundary layers.

The inferred density distributions directly translate to the mean gas surface mass density of the cool CGM, as shown in the *middle* panel of Fig. 7 for a sample of massive quiescent galaxies (Zahedy et al., 2019). For these high-mass galaxies, the radial profile of surface mass densities exhibits a strongly declining presence of cool gas toward larger radii in the halo. In contrast, the surface mass densities of the hot halo inferred from a joint analysis of X-ray and Sunyaev-Zel'dovich signals (e.g., Sunyaev and Zeldovich, 1980) appear to be significantly flatter (Singh et al. 2018; light grey band in the *middle* panel of Fig. 7), suggesting that the hot halo is more spatially extended than the cool gas. Integrating the surface mass density profile over the projected area directly constrains the gas mass in the cold and hot phases. Within  $d \approx 160$  kpc, it was found that the cool phase contains a total mass of  $M_{\text{cool}} \sim 1.5 \times 10^{10} M_{\odot}$ , which is about 10% of the total mass in the hot phase (Zahedy et al., 2019). For massive galaxies residing in halos of  $M_h \approx 10^{13} M_{\odot}$ , the vast majority of the mass of the CGM resides in the hot phase, with the cool phase contributing  $\lesssim 10$  percent of the total mass of the CGM. This stands in contrast to the CGM mass distribution observed in smaller halos of  $10^{12} M_{\odot}$  (see Fig. 2), where the cool phase comprises a larger fraction of the total gas mass. It indicates a shift in the balance between the hot and cool phases as galaxy halos grow in mass.

Spectrally-resolved photoionization analyses offer a range of utilities beyond inferring density and gas mass. Each best-fit ionization model provides predictions of the ionization fraction of different species. Combining the observed neutral hydrogen column density  $N_{\text{HI}}$  and the anticipated neutral fraction of hydrogen,  $f_{\text{HI}}$ , yields a size estimate of the absorbing clump along the line of sight, following  $l_{\text{cl}} = N_{\text{HI}}/(f_{\text{HI}} n_{\text{H}})$ . Similarly, combining the observed column densities of metal ions and their anticipated ionization fraction leads to estimates of the elemental abundances.

Most resolved absorbing clumps are found to range in size from approximately 10 pc to 1 kpc, with a mode around  $\langle l_{\text{cl}} \rangle_{\text{mode}} = 100$  pc, in halos surrounding both star-forming and massive quiescent galaxies (e.g., Zahedy et al., 2019, 2021). Cool CGM clumps as small as  $l_{\text{cl}} \approx 1$  pc have also been reported (e.g., Muzahid et al., 2018; Chen et al., 2023a), revealing fine-grain details of the diffuse gas in distant galaxy halos, similar to what is found in nearby star-forming galaxies (see e.g., Fig. 1). While uncertainties in the ionizing radiation flux ( $\phi$ ) place a fundamental limit in the inferred density (a higher  $\phi$  translates to higher  $n_{\text{H}}$  and smaller  $l_{\text{cl}}$ ; see e.g., Zahedy et al. 2019 and Section 3.2 above), the clump sizes inferred from the best-fit photoionization models are consistent with those derived for Mg II-absorbing from comparing the absorption profiles across multiply-lensed quasar sightlines (e.g., Rauch et al., 2002). The consistency lends strong support for the robustness of the spectrally resolved photoionization analysis. Given known gas density, one can compute the Jeans length, which determines the maximum extent over which the clumps are stable against gravitational collapse, following the relation  $l_{\text{J}} \equiv c_s / \sqrt{G \mu m_{\text{H}} n_{\text{H}}}$  (e.g., Binney and Tremaine, 2008). Here  $G$  is the gravitational constant,  $c_s$  is the sound speed and  $\mu$  is the mean molecular weight. For a typical gas density of  $n_{\text{H}} \sim 0.01 \text{ cm}^{-3}$ , the corresponding Jeans length is  $l_{\text{J}} \approx 20$  kpc, which is significantly larger than the inferred clump sizes. Therefore, while these cool photoionized clumps are relatively small, thermal pressure is sufficient to support them against gravity.

Similar to gas densities, CGM metallicity—measuring the abundance of elements heavier than helium—also exhibits a large spread along individual sightlines, from less than 1% solar to super solar values (*right* panel of Fig. 7). The large scatter implies that chemical enrichment may be localized and mixing is inefficient (e.g., Schaye et al., 2007). Because outflowing materials from star-forming regions are expected to be enriched by metals while newly accreted gas from the IGM is expected to be low in its metal content (e.g., Péroux and Howk, 2020), the simultaneous presence of metal-poor and metal-rich gas also supports the notion of a dynamic halo being regulated by inflows and outflows at once (see e.g., Fig. 1). However, detecting near-solar to super-solar clumps at  $d \gtrsim 100$  kpc is surprising. Comparing the elemental abundance pattern with different enrichment sources may provide key insights into the origin of these highly enriched clumps (see Section 4.4 below).

### 4.3 Thermodynamics and energy balance

In addition to resolving small-scale density variations (see Fig. 7) and revealing the complex multiphase structure of the CGM (Fig. 5), high-resolution absorption spectroscopy has enabled detailed investigations into gas kinematics—specifically, the relative motion of gaseous clumps along the line of sight in the rest frame of their host galaxies. In a multiphase CGM where cool, dense gas clouds are confined by pressure with a more rarified and volume-filling hot gas (Fig. 2), the motions of a population of these cool clouds convey critical information about how the different phases of the CGM interact with each other, as well as the physical mechanisms with which such interactions operate. At a fundamental level, these line-of-sight kinematics provide critical insights into the origin and ultimate fate of the gas. In turn, the answer informs the overall understanding of how galaxies of varying masses contribute to the enrichment of the IGM and, by extension, the Universe with heavy elements over cosmic time.

For example, under hydrostatic equilibrium, the absorbing clumps are expected to follow the virial motion dictated by the dark matter halo. The velocity dispersion of these absorbing clumps should align with the halo's virial velocity,  $v_{\text{vir}} \approx 130 \text{ km s}^{-1} (M_h/10^{12} M_{\odot})^{1/3} (1 + z)^{1/2}$  (e.g., Mo et al., 2010). Accordingly, the observed velocity dispersion projected along the line of sight should follow  $\sigma_v = v_{\text{vir}}/\sqrt{3}$ . In addition, whether or not the gas remains gravitationally bound to the host halo or escapes into the IGM depends on how deep the gas clumps

are in the potential. This can be evaluated based on the escape velocity  $v_{\text{esc}}(r) = \sqrt{2|\Phi(r)|}$  expected at the distance  $r$  from the halo center, which is defined as the velocity necessary to compensate for the gravitational potential  $\Phi(r)$  for the gas to escape. Although simplified, comparing the observed line-of-sight velocity offset of the clumps from the host galaxy with the predicted  $v_{\text{esc}}$  for a given  $r$  and  $\Phi$ , typically modeled using the (Navarro et al., 1997, NFW) profile, provides an initial assessment for the likelihood of the absorber being unbound.

As a starting point, the *top-left* panel of Fig. 8 displays the line-of-sight velocity offsets between Mg II-traced CGM absorption complexes and their host galaxies versus host galaxy mass at  $z \approx 0.25$  (Huang et al., 2021). The line-of-sight velocities are compared directly with the expected escape velocity (projected along the line of sight) of the dark-matter halo, and they are evaluated at various distances in the CGM. This comparison reveals that, in the low-redshift CGM, most observed absorbers are consistent with being gravitationally bound to their host halos. Interestingly, an analysis of a sample of seven star-forming galaxies at  $z \approx 2$  with associated metal absorption components has revealed that five of these galaxies ( $\approx 70\%$ ) exhibit CGM clouds with velocities exceeding the escape speeds of their halos, as shown in the *top-right* panel of Fig. 8 from Rudie et al. 2019)

The contrasting CGM kinematics between low- and high-redshift galaxies can be understood by considering two key factors. At higher redshifts ( $z \geq 2$ ), typical galaxies are less massive and experience more intense star formation compared to their low-redshift counterparts. In contrast, galaxies at lower redshifts are more massive and quiescent in star formation, possess deeper potential wells, and drive less powerful outflows, leading to more bound gas in the CGM and less metal enrichment of the surrounding IGM. These differences in mass and star formation rates across cosmic time naturally lead to varying CGM kinematics between high- and low-redshift galaxies. The expectation of high-redshift low-mass galaxies driving vigorous outflows to push metal-enriched gas out of the galaxies and into the surrounding medium is qualitatively consistent with the observations of IGM being enriched to a mean metallicity of  $Z \approx 10^{-3} Z_{\odot}$  as early as  $z \approx 4 - 5$  (e.g., Schaye et al., 2003).

A particularly informative diagnostic for evaluating whether the observed clump motions align with the virial velocities of their host galaxies is the velocity dispersion between absorbers and galaxies over an ensemble of absorber and galaxy pairs. The *bottom-left* panel of Fig. 8) displays histograms of line-of-sight velocity distribution, normalized by the escape velocity  $v_{\text{esc}}$ , for Mg II-traced cool CGM clouds in separate samples of Milky-Way like ( $M_h \sim 10^{12} M_{\odot}$ ) star-forming and more massive ( $M_h \sim 10^{13} M_{\odot}$ ) quiescent (LRG) halos. Normalizing by the escape velocity allows for a direct comparison of internal halo dynamics across galaxies of widely varying mass, placing them on a comparable scale. One particularly striking feature in this plot is the significant differences in cloud motions between massive quiescent LRG halos and lower-mass star-forming halos. Cool CGM clouds around high-mass LRGs exhibit sub-virial motion characterized by a velocity dispersion that is only  $\approx 50 - 60\%$  of what is expected from virial motion, whereas clouds around lower-mass ( $M_h \sim 10^{11-12} M_{\odot}$ ) star-forming galaxies show a velocity dispersion that is consistent with virial motion expected for their host halos (e.g., Huang et al., 2021; Anand et al., 2021).

The suppressed line-of-sight velocity of cool CGM clouds in high-mass halos has important implications for halo gas dynamics, suggesting that these clouds are affected by physical processes beyond gravitational interactions (e.g., Huang et al., 2016; Zahedy et al., 2019; Afruni et al., 2019). Specifically, in the presence of a volume-filling hot CGM, moving cool clouds are subject to a ram-pressure drag force that slows them down (e.g., Gunn and Gott, 1972), until they eventually reach terminal speeds that are less than the virial velocity of the halo. For these dissipative hydrodynamic interactions to slow down the cool gas appreciably on timescales shorter than the orbital time (which is required by the observations), these cool clumps cannot be too massive to begin with, with a mass upper limit that has been estimated to be  $\sim 10^4 M_{\odot}$  (e.g., Zahedy et al., 2019; Afruni et al., 2019). At the same time, thermal interactions via conduction with the surrounding hot CGM will cause the cool clouds to evaporate over time, as heat is gradually transferred from the hot to the cool phase. For a  $\sim 10^4 M_{\odot}$  cool cloud, the expected evaporation time is significantly shorter than the dynamical timescale of the halo (e.g., Huang et al., 2016). While these calculations are highly uncertain due to the unknown cloud geometry and the details of thermal conduction, the most likely outcome is that cool clumps in massive LRG halos traverse only a relatively small distance in the CGM during their lifetimes, and most of these clouds will evaporate before reaching the massive galaxies at the center of the halos.

Further insight into the thermodynamic state of the CGM can be obtained by examining gas motions within individual gas clouds themselves, which is afforded by high-resolution spectroscopy from both ground and space. As described in Section 3.2, both thermal and non-thermal motions of atoms and ions in a gas cloud contribute to the observed line broadening. The mass-dependent line broadening from thermal motion and the mass-independent line broadening due to non-thermal motion (e.g., turbulence) can be distinguished by observing two or more ions of different atomic masses. These observations provide a quantitative measure of the internal energetics of these clouds. In particular, energetic processes such as supernova and AGN feedbacks are expected to inject thermal energy into the CGM while also increasing gas turbulence, which may limit the ability of the CGM to infall, replenish the ISM, and fuel future star formation (e.g., Gaspari et al., 2018; Schneider et al., 2020).

By decomposing the observed total kinetic energy into thermal and non-thermal contributions, one can compute the thermal energy fraction following the relation  $E_{\text{th}}/E_{\text{tot}} = b_{\text{th,HI}}^2 / (b_{\text{th,HI}}^2 + \mu b_{\text{nt}}^2)$ , where  $\mu = 0.6$  is the mean molecular weight for ionized gas (e.g., Qu et al., 2022). It is straightforward to show that the thermal energy fraction is related to the Mach number of the gas,  $\mathcal{M} \equiv v_{\text{nt}}/c_s$ , following  $E_{\text{th}}/E_{\text{tot}} = (1 + \gamma(\gamma - 1)\mathcal{M}^2/2)^{-1}$  (e.g., Rudie et al., 2019), where  $\gamma$  is the adiabatic index and  $\gamma = 5/3$  for monatomic gas. As shown in the *bottom-right* panel of Fig. 8, examining the internal energetics of CGM clouds in different galaxy samples has uncovered a striking difference between lower-mass star-forming galaxies and high-mass quiescent LRGs. Specifically, while the majority of cool clumps are subsonic with the velocity field driven by thermal motions, an appreciable fraction of cool gas in the CGM massive quiescent galaxies (LRGs) displays non-thermal and supersonic turbulence. While these results are intriguing, it should be noted that this comparison was performed for galaxy halos of significantly different masses, with LRG halos being on average an order of magnitude more massive than star-forming halos. Despite this caveat, the increased turbulence of cool clouds in LRG halos, in addition to their observed sub-virial



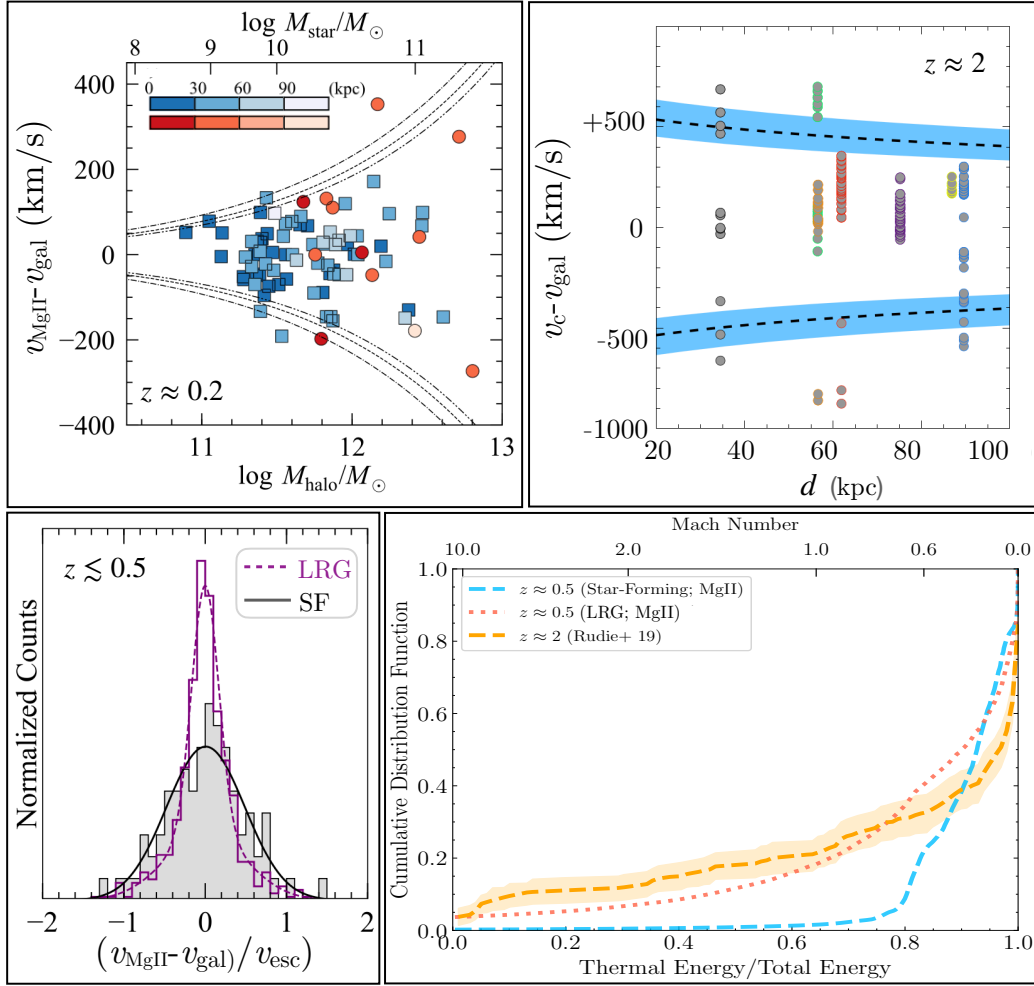


**Fig. 8** Gas kinematics in the galactic atmosphere revealed in absorption line profiles provide independent clues for the physical origin and fate of the observed cool CGM clouds. The relative velocity offsets between the systemic velocity of the host galaxy,  $v_{\text{gal}}$ , and the column density weighted velocity centroid of the associated Mg II absorption complex ( $v_{\text{MgII}}$ , *top-left*) over an ensemble of Mg II-galaxy pairs at  $z \approx 0.25$  show that the majority of these absorbers are consistent with being gravitationally bound to the host galaxies (adapted from Huang et al. 2021). The curves represent the expected escape velocity projected along the line of sight at distances of 30, 60, and 90 kpc. A similar finding has also been reported for individual metal absorption components ( $v_c$ ) detected in the vicinities of star-forming galaxies at  $z \approx 2$  (*top-right*; adapted from Rudie et al. 2019). These observations demonstrate that the majority of these metal ions do not escape their host halos (cf., Ho et al., 2021). Separating galaxies into sub-samples based on their star formation properties has further uncovered intriguing differences in the cloud motions with absorbing clouds in the vicinities of luminous red galaxies (LRGs; massive quiescent galaxies) displaying sub-virial motions (e.g., Huang et al., 2016), while those around star-forming (SF) galaxies showing velocity dispersions consistent with virial motions in the host halos (*lower-left*; adapted from Huang et al. 2021). At the same time, a non-negligible fraction ( $\approx 20\%$ ) of cool gas identified around LRGs, massive quiescent galaxies, exhibits predominantly supersonic turbulence. In contrast, the majority of cool clumps identified in star-forming halos exhibit thermally driven random motions (*lower-right*; adapted from Qu et al. 2022).

motions, provides a tantalizing hint for a lack of star formation in these quiescent galaxies, despite the presence of significant amounts of cool gas in their CGM.

#### 4.4 Chemical enrichment

Observations of diffuse gas in the CGM have traditionally relied on detecting the presence of heavy elements at large distances from galaxies. As discussed in Section 2 and illustrated in Fig. 2, various metal ions have been identified, each tracing different density and temperature regimes in the CGM. The presence of these ions has direct implications for the thermal and chemical states of the gas. For example, the radiative cooling function depends sensitively on the gas metallicity (e.g., Mo et al., 2010), with higher-metallicity gas cooling more rapidly under the same radiation field for a fixed density. Gas metallicity is also strongly correlated with the total dust content, with higher-metallicity gas showing a higher fraction of dust at a given gas mass (e.g., De Cia et al., 2016). Gas metallicity is, therefore, a key

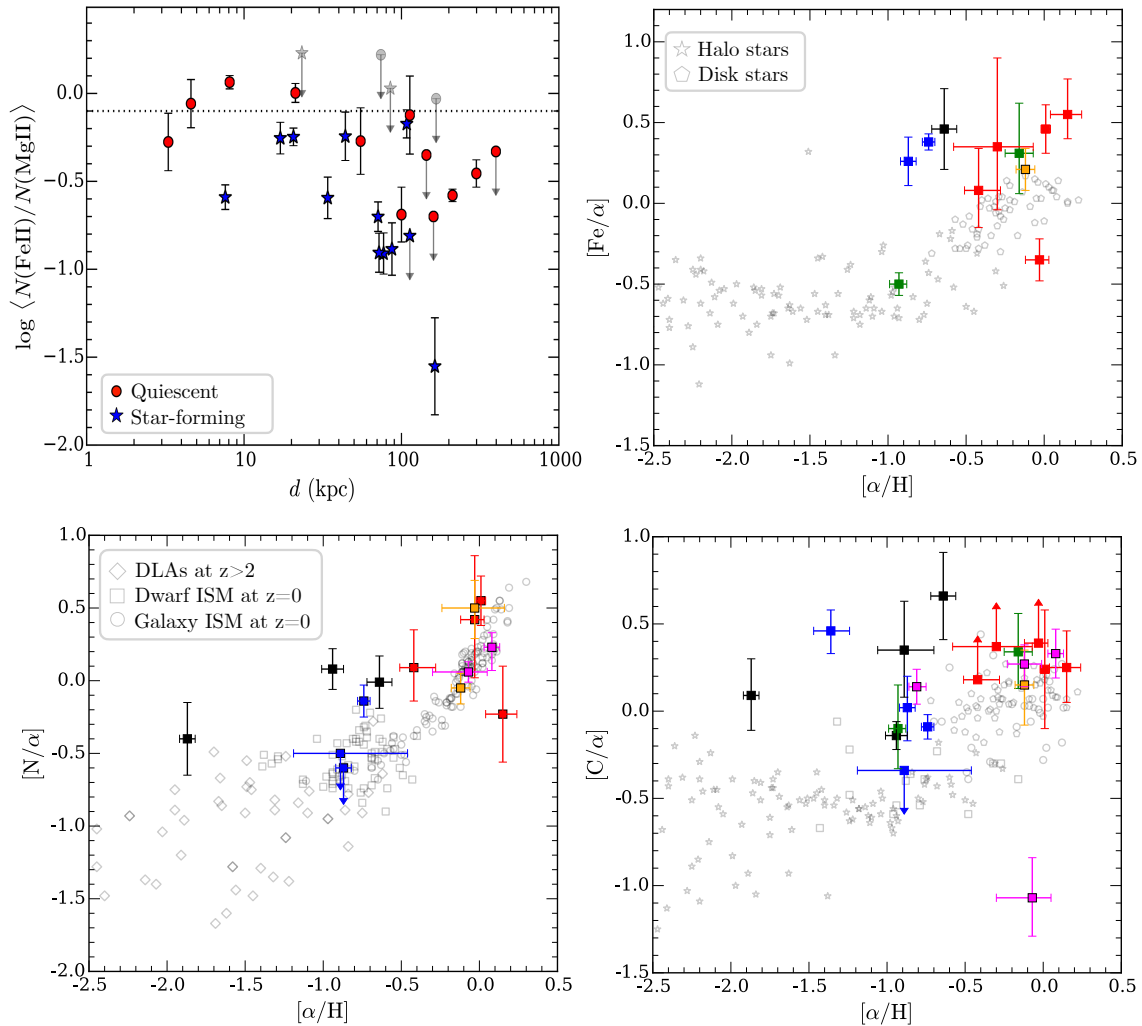


**Fig. 9** Chemical tagging based on the relative abundances of different elements provides a timing clock for identifying the enrichment sources, thereby constraining the physical origin of the gas. Specifically, the abundance ratios between  $\alpha$ -elements (e.g., Mg, O), produced promptly over short ( $\sim$  Myr) timescales in massive stars and core-collapse supernovae (SNe), and elements produced in Type Ia SNe (e.g., Fe) and intermediate-mass stars (e.g., N, C) over longer ( $\geq 0.1$  Gyr) timescales have long been used to chronicle the chemical enrichment history in Galactic stars and the ISM of other galaxies (e.g., McWilliam, 1997; Weinberg et al., 2019). In the CGM, these measurements reflect the chemical enrichment sources and timing of heavy element ejection from galaxies. Indeed, the cool CGM generally displays a declining observed Fe/Mg relative abundance ratio with distance, indicating a chemical enrichment history driven by massive stars in halo outskirts (upper-left panel Zahedy et al., 2017). At the same time, quiescent galaxies display enhanced Fe abundances, comparable to the solar value (dotted line in the upper-left panel) in the inner halos of quiescent galaxies, suggesting significant contributions from evolved stellar populations. In addition, while the observed spread in metallicity (see Fig. 7) suggests that chemical mixing is inefficient, the observed spread of  $[\text{Fe}/\alpha]$ ,  $[\text{N}/\alpha]$ , and  $[\text{C}/\alpha]$  within a single halo (points sharing a common color in the upper-right and bottom panels) indicates that chemical mixing is a complex physical process (e.g., Zahedy et al., 2021; Cooper et al., 2021). In particular, the presence of a handful of metal-poor gas ( $[\alpha/\text{H}] \lesssim -0.1$ ) with otherwise enhanced Fe, C, and N abundances suggests dilution of stellar ejecta by recently accreted, chemically primitive gas from the IGM.

quantity that determines the physical conditions of gaseous clouds in a wide range of astronomical environments (e.g., Draine, 2011).

Since heavy elements are produced by stars in galaxies, gas metallicity also serves as a key measure of a galaxy’s overall production of heavy elements. Large-scale spectroscopic surveys of local galaxies have shown that galaxies follow a well-established mass-metallicity relationship, with more massive galaxies exhibiting higher stellar (e.g., Kirby et al., 2013) and gas-phase (ISM; e.g., Tremonti et al., 2004) metallicities compared to their lower-mass counterparts. As a result, gas ejected from high-mass central galaxies is expected to be more metal-enriched than gas stripped from lower-mass satellite galaxies. Moreover, recently accreted gas from the IGM should have even lower metallicity, given its chemically primitive nature (e.g., van de Voort et al., 2012; Anglés-Alcázar et al., 2017).

However, these straightforward expectations are complicated by the poorly understood chemical mixing processes and heavy element transport in the baryon cycle. If chemical mixing is efficient, with mixing timescales shorter than the dynamical time of the halo, high-

metallicity gas expelled from the ISM can rapidly combine with lower-metallicity gas in the outskirts of the CGM, diluting the mixture and reducing its overall metallicity. In such cases, the observed metallicity would no longer reflect the source of the gas in a chemically evolved environment. In contrast, if chemical mixing is highly inefficient, CGM gas could retain its original metallicity long after being ejected from galaxies, leading to significant variations in metallicity within the same galaxy halo. Indeed, as shown in the right panel of Fig. 7 and in Fig. 9, large metallicity spreads—ranging from factors of 10 to 100—are commonly observed in the CGM of individual galaxies across a broad range of masses (e.g., Zahedy et al., 2019, 2021; Sameer et al., 2024), highlighting the complex chemical enrichment history of CGM gas. Therefore, gas metallicity alone is an incomplete diagnostic of the physical origins of CGM gas.

Elemental abundance ratios in gas serve as an archaeological record of the various sources of heavy element production. For instance,  $\alpha$ -process elements (e.g., O, Mg, Si, and S) are produced through the rapid capture of  $\alpha$  particles (helium nuclei), a process that occurs predominantly in the late evolutionary stages of massive stars ( $M \gtrsim 10 M_{\odot}$ ) and their subsequent core-collapse supernovae (SNe CC). This relatively prompt origin of  $\alpha$  elements contrasts with that of Fe-peak elements (e.g., Fe, Ni, Mn), which are produced in large quantities by Type Ia supernovae (SNe Ia Kobayashi et al., 2020). SNe Ia arise from white dwarf remnants of lower-mass stars ( $\lesssim 8 M_{\odot}$ ), whose longer lifetimes delay the release of Fe-peak elements compared to the more rapid enrichment from SNe CC (e.g., Maoz et al., 2012). As a result, the observed  $[\text{Fe}/\alpha]$  abundance ratio is particularly valuable, as it not only traces the relative contributions of SNe CC and SNe Ia to chemical enrichment but also provides a timing ‘clock’ for the release of heavy elements from galaxies, offering insights into the physical origins of the gas.

The utility of investigating CGM chemistry is illustrated in Fig. 9. The *top-left* panel shows the radial profile of Fe/Mg elemental abundance ratio in the cool CGM of intermediate-redshift star-forming and quiescent galaxies (Zahedy et al., 2017), and several noteworthy features are immediately apparent. First, the cool CGM exhibits a general trend of declining Fe/Mg abundance ratio with increasing distance from galaxies. In the outskirts of the CGM at  $d \gtrsim 100$  kpc, Mg-rich gas with  $[\text{Fe}/\text{Mg}] < -0.3$  is relatively common, which is consistent with an early chemical enrichment history that is dominated by massive stars and SNe CC. Secondly, the CGM of quiescent galaxies displays Fe enhancement relative to star-forming galaxies, especially at small projected radii of  $d \lesssim 10$  kpc, where solar or supersolar Fe/Mg values are commonly observed. The observed Fe enhancement can be understood as a result of significant contributions from evolved stellar populations in quiescent galaxies, leading to a higher proportion of SNe Ia than seen in the solar neighborhood (Zahedy et al., 2016, 2017).

While the large spread in CGM metallicity shown in Fig. 7 indicates that chemical mixing in the CGM is an inefficient process, further insight into chemical mixing can be obtained by examining various elemental abundance ratios in the CGM as a function of gas metallicity. This exercise is illustrated in the remaining three panels of Fig. 9, which displays the observed  $[\text{Fe}/\alpha]$ ,  $[\text{N}/\alpha]$ , and  $[\text{C}/\alpha]$  abundance ratios in the CGM as a function of metallicity  $[\alpha/\text{H}]$ , in comparison with existing constraints on these quantities for Galactic stars as well as ISM gas at low and high redshifts (Zahedy et al., 2021; Cooper et al., 2021). In contrast to  $\alpha$ -process elements primarily produced in massive stars and SNe CC and Fe-group elements produced largely in SNe Ia, nitrogen and carbon owe their existence largely from intermediate-mass asymptotic giant branch (AGB) stars (e.g., Romano, 2022).

The complex nature of chemical enrichment in the CGM is evident in the substantial spread ( $> 1$  dex) in both the absolute gas metallicity  $[\alpha/\text{H}]$  and relative elemental abundance ratios. At the same time, investigations of the observed variations in  $[\alpha/\text{H}]$ ,  $[\text{Fe}/\alpha]$ ,  $[\text{N}/\alpha]$ , and  $[\text{C}/\alpha]$  within *individual* galaxy halos are also instructive. First, a clear majority ( $\gtrsim 60\%$ ) of detected CGM clouds have chemical properties (metallicity and elemental abundance ratios) consistent, to within the measurement uncertainties, with the observed metallicities and abundance ratios in stars and the ISM. Taken at face value, a lack of dilution would be a natural consequence of inefficient chemical mixing in the CGM. On the other hand, the presence of a handful of metal-poor gas clouds ( $[\alpha/\text{H}] \lesssim -0.1$ ) with otherwise elevated Fe, N, and C abundances suggests the dilution of chemically evolved gas (stellar ejecta or ISM gas) by more recently accreted gas from the chemically more primitive IGM. While this type of detailed chemical study has been performed for a relatively small number of diffuse CGM clouds to date, these investigations highlight the power of using CGM chemistry to resolve the physical origins of halo gas observed at large distances from galaxies.

## 5 Future outlook

Observational studies have revealed the CGM as part of a dynamic, complex, and multiphase ecosystem. Theory predicts that this gas reservoir plays a crucial role in regulating star formation and chemical enrichment in galaxies across cosmic time (e.g., Somerville and Davé, 2015; Naab and Ostriker, 2017; Crain and van de Voort, 2023). Despite significant advancements in our empirical understanding of the CGM’s global content and its physical and chemical properties, many fundamental questions remain. These open questions highlight the missing physics in our current understanding of the origin of the multiphase gas, its role in regulating the cosmic baryon cycle, and its connection to galaxy growth and evolution over time.

Using high-resolution absorption spectroscopy, astronomers have been able to resolve detailed density, thermodynamic, and chemical enrichment structures over a large dynamic range in spatial scales from  $\approx 1$  pc to  $\approx 1$  kpc in the diffuse CGM to density as low as  $n_{\text{H}} \sim 10^{-4} \text{ cm}^{-3}$  (Section 3.2). However, these studies have largely been limited to one-dimensional (1D) probes, making establishing direct connections to galaxy properties along transverse directions to the absorbers challenging. On the other hand, detections of line-emitting signals from the diffuse CGM provide two-dimensional (2D) morphologies for establishing direct connections between star formation and AGN activities in galaxies and the extent, kinematics, and ionization conditions of the gas (Section 3.1). However, emission measures are biased toward the highest-density clumps and severely affected by the  $(1+z)^4$  cosmological dimming. Current emission observations are largely limited to detecting Ly $\alpha$  photons, which are challenging to interpret due to their resonant scattering nature.

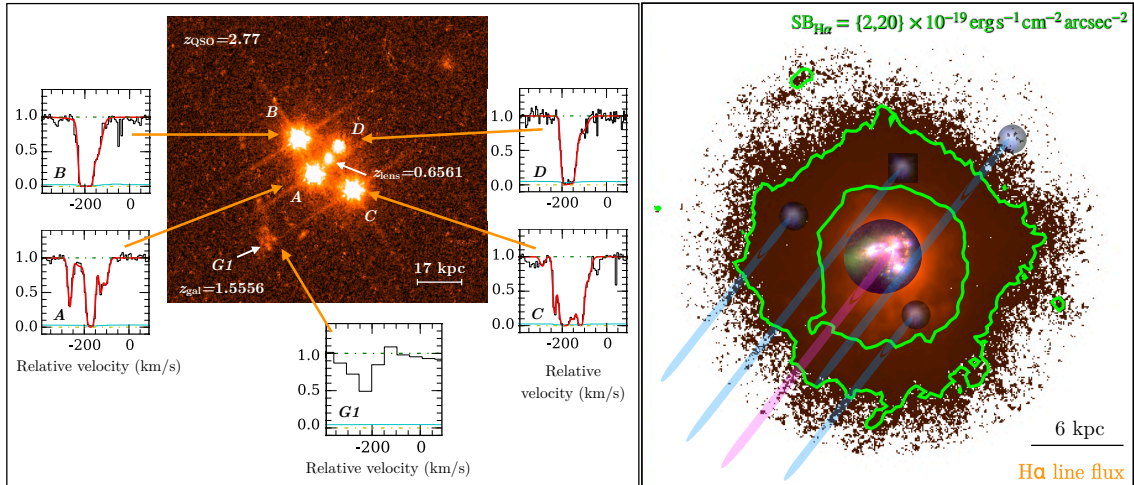


**Fig. 10** Mapping the multi-scale and multiphase galactic atmosphere in absorption *and* emission. The *left* panel showcases an example of spatially and spectral resolving gas flows in the CGM of a star-forming galaxy at  $z_{\text{gal}} = 1.556$ , using a combination of a quadruply-lensed quasar at  $z_{\text{QSO}} = 2.77$  and stars in the galaxy itself (Zahedy et al. in preparation). The presence of a blueshifted absorption profile in the galaxy’s spectrum (*G1* panel) confirms that the galaxy is actively driving outflows (zero velocity corresponds to the galaxy’s systemic redshift determined from [O II] emission lines), while the four lensed quasar sightlines (*A* to *D*) probe the galaxy’s CGM as projected distances between  $d = 39$  and  $d = 45$  kpc. The high spectral resolving power afforded by the lensed quasar has helped reveal chaotic gas motions with velocity dispersion exceeding  $100 \text{ km s}^{-1}$  across all four sightlines. The *right* panel showcases a spatially extended  $\text{H}\alpha$  line emitting halo uncovered around a low-mass starburst galaxy with sensitive IFS observations. The size of the  $\text{H}\alpha$  halo is  $\approx 5$  times larger than the stellar body, revealing remnants of tidal interactions that triggered the starburst phase (see also Menacho et al., 2019). Because the emission signals scale with gas density according to  $n_{\text{H}}^2$ , the intensity map is most sensitive to high-density peaks. Applying absorption spectroscopy of multiple background sources with future large telescopes will enable a dense sampling of the low-density gas missed by the emission-line maps.

### 5.1 Spatially and spectrally resolve the multiscale and multiphase CGM in absorption and emission

Spatially and spectrally resolved maps of the CGM around galaxies of different star formation history and over a broad redshift range hold the promise to resolve the complex multiscale physics and establish a direct connection between gas and stars in the cosmic ecosystems. This can be achieved with upcoming surveys using several different techniques, including emission observations using high-throughput wide-area integral field spectrographs (IFSs) on large ground-based telescopes and high-resolution absorption spectroscopy of multiply-lensed quasars uncovered from deep all-sky surveys. Combining 2D emission maps with high-resolution absorption spectra of multiply-lensed background objects enables a full exploration of this cosmic gas reservoir based on a high-definition 3D view of its density, velocity, and chemical enrichment structures.

Luminous quasars, multiply lensed by a foreground object, expand traditional quasar absorption spectroscopy from 1D to 2D probes, and provide additional spatial resolving power for constraining the size and velocity (de)coherence of absorbing gas (e.g., Rauch et al., 2001; Zahedy et al., 2016). A gravitationally lensed QSO occurs when the strong gravitational field of a massive galaxy situated directly between the observer and a distant QSO produces multiple lines of sight corresponding to the multiple images of the quasar, as shown in the *left* panel of Fig. 10. As a result of this serendipitous alignment, the multiple images (usually two to four) of a lensed QSO act as independent probes to resolve the CGM and represent a powerful means to measure the kinematic and chemical coherence scales in the CGM and identify different gas flows and constrain their properties based on the additional spatial information.

The example displayed in Fig. 10 showcases a quadruply-lensed QSO at  $z_{\text{QSO}} = 2.77$  and a star-forming galaxy *G1* at  $z_{\text{gal}} = 1.556$ . This foreground galaxy *G1* is driving a strong outflow, as evidenced by the presence of a blueshifted absorption profile in its spectrum. The four lensed lines of sight (*A* to *D*) each probes the gaseous halo of the galaxy at projected distances of between 39 and 45 kpc (Zahedy et al. in preparation). High-resolution absorption spectra of these sightlines all show the abundant presence of cool gas around this galaxy. At the same time, significant differences are seen in the absorption profiles among four sightlines separated by only a few kpc. Specifically, while the gas exhibits kinematically complex with large velocity spreads ( $\geq 200 \text{ km s}^{-1}$ ) along sightlines *A* and *C* at  $d \approx 40$  kpc, the observed kinematics are comparatively simpler with smaller velocity spreads along *B* and *D* probing distances a few kpc farther from *G1*. These observations suggest that the outflowing material from *G1* either decelerates and/or becomes more disrupted and less well-collimated with increasing distance. A quantitative analysis will provide strong constraints on the outflow geometry and energetics, and investigating the observed variations in gas chemistry across the four sightlines will provide critical insight into the physical origins of the gas.

Since the discovery of the first doubly imaged lensed quasar in 1979 (Walsh et al., 1979), nearly 300 have been discovered to date (Lemon et al., 2024), and around a few dozen are bright enough to obtain high-resolution spectra of with current facilities. The upcoming all-sky Legacy Survey of Space and Time (LSST) at the Rubin Observatory is expected to discover approximately 8000 new lensed quasars (e.g., Oguri and Marshall, 2010) during the survey’s duration. Among these, at least 500 will be bright enough for high-resolution observations



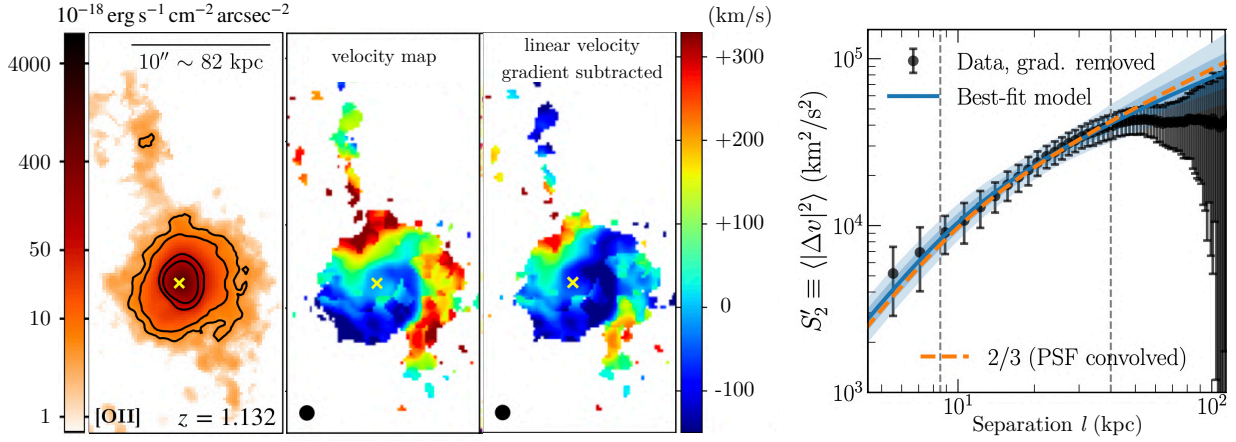


**Fig. 11** Turbulent energy transfer across different spatial scales from  $\geq 50$  kpc to  $\leq 10$  kpc in a giant quasar nebulae (adapted from Chen et al., 2023b). The three left panels display the 2D maps of [O II] surface brightness, observed line-of-sight velocities, and residual velocities after a best-fit linear gradient is subtracted (from left to right; see also Johnson et al., 2022). This central [O II]-emitting nebula with surface brightness exceeding  $10^{-18} \text{ erg s}^{-1} \text{ cm}^{-2} \text{ arcsec}^{-2}$  spans nearly 100 kpc in diameter with fluctuating line-of-sight velocities ranging from  $< -100 \text{ km s}^{-1}$  to  $> +300 \text{ km s}^{-1}$  from the systemic redshift of the quasar at  $z_{\text{QSO}} = 1.132$ . The right panel displays the residual velocity variance after subtracting a linear velocity gradient,  $\langle |\Delta v(l)|^2 \rangle$ , versus projected separation  $l$ , representing the 2nd-order velocity structure function (VSF). Accounting for the atmospheric seeing effects that smooth ground-based data and progressively suppress noise at smaller scales, the best-fit model (blue solid curve) aligns well with the Kolmogorov expectation (orange dashed curve), which predicts a slope of  $2/3$  for isotropic, homogeneous, and incompressible fluids. This agreement suggests subsonic turbulence and a constant energy transfer across spatial scales within the quasar nebula.

with future Extremely Large Telescopes (ELTs), representing a more than tenfold increase over the current state of the field.

In parallel, IFS observations, targeting non-resonant emission lines to a surface brightness limit of  $\approx 10^{-19} \text{ erg s}^{-1} \text{ cm}^{-2} \text{ arcsec}^{-2}$  or fainter, will begin to probe the density and velocity structures in diffuse halo gas around typical star-forming galaxies (e.g., Corlies et al., 2020; Dutta et al., 2024). The right panel of Fig. 10 showcases extended  $\text{H}\alpha$  line emitting signals around Haro 11, a starburst galaxy at  $z \approx 0.02$  (e.g., Grimes et al., 2009), uncovered in moderately deep IFS observations. The line-emitting gas covers an area that is five times the size of the stellar body (see also Menacho et al., 2019). The gas is detected in multiple nebular lines, placing strong constraints on the gas density and ionization conditions. It is found that the gas is primarily photoionized by the young star clusters with a relatively high density in the immediate proximity of the central star clusters with  $n_{\text{H}} \approx 100 \text{ cm}^{-3}$ . The gas density declines toward the outskirts with a loose constraint of  $n_{\text{H}} < 40 \text{ cm}^{-3}$ . The emission morphology shows that the gas is clumpy and reveals clear tidal features extending outward from the nuclear star clusters.

A promising new avenue these spatially resolved maps enable is investigating turbulent energy transfer across spatial scales. This approach offers an empirical framework to understand how feedback energy from massive stars and SMBHs on parsec scales couples to diffuse gaseous halos extending over 100 kpc or more, influencing their thermal state. Specifically, energetic processes associated with stellar activity, SMBHs, and satellite accretion events are expected to stir the surrounding medium, disrupting bulk flows and driving turbulence (see e.g., Fig. 1). In addition, a cool, ionized plasma of density  $n_{\text{H}} \approx 0.01 \text{ cm}^{-3}$  and temperature  $T \approx 10^4 \text{ K}$  (see Section 2) is expected to have an effective mean free path of  $\sim 10^{14} \text{ cm}$  and kinematic viscosity of  $\approx 10^{20} \text{ cm}^2 \text{ s}^{-1}$  (e.g., Spitzer, 1962; Sarazin, 1986). For clumps of size 100 pc (e.g. Zahedy et al., 2021), moving at speeds of  $100 \text{ km s}^{-1}$  in galaxy halos (e.g., Huang et al., 2021), the associated Reynolds number is large,  $Re \sim 3 \times 10^7$  (cf. Marchal et al., 2021, for neutral medium observed in Milky Way high-velocity clouds). This high Reynolds number suggests that the cool CGM clouds are likely turbulent (see also Burkhart, 2021).

A classical approach in fluid dynamics for characterizing the degree of this decorrelation is to measure the velocity structure functions (VSFs), which are moments of velocity fluctuations ( $S_n$ ) as a function of spatial scales  $l$  for quantifying the velocity power spectrum (e.g., Frisch, 1995; Boldyrev, 2002). In particular, the second-order VSF,  $S_2(l)$ , represents the scale-dependent variance of the turbulent medium  $|\Delta v(l)|^2$ , which translates directly to the turbulent energy on different scales, and the energy transfer between different scales is expected to be conserved in a homogeneous, isotropic, and incompressible fluid. From dimensional analysis, it is straightforward to demonstrate that a constant energy transfer rate would lead to a constant  $\Delta v^2(l) \times \Delta v(l)/l$ . In turn, it gives a power-law relation of  $\langle |\Delta v(l)|^2 \rangle \propto l^{2/3}$  and an energy transfer rate per unit mass of  $\epsilon = (5/4) \langle |\Delta v(l)|^3 \rangle / l$  (e.g., Kolmogorov, 1941). For subsonic turbulence, kinetic energy injected on large scales is expected to propagate to small scales at a constant rate ( $\epsilon$ ), eventually dissipating at the smallest scale when viscosity transforms the kinetic energy into heat. Observations of scale-dependent velocity dispersion, therefore, place direct constraints on turbulent heating in the diffuse CGM.

By targeting multiply-lensed QSOs, Rauch et al. (2001) presented the first VSF measurements of the intergalactic medium at  $z \approx 3$  on spatial scales between 30 pc and 30 kpc. However, the measurements were limited by a small sample of C IV absorbers found along multiply-lensed QSOs, which led to large uncertainties. Recent IFS observations of spatially extended line-emitting nebulae have reinvigorated interest in investigating turbulence within the diffuse halo gas through VSF measurements (e.g., Li et al., 2020; Chen et al., 2023b).

Initial results have generated new surprises and puzzles.

Fig. 11 showcases a giant luminous quasar nebula at  $z_{\text{QSO}} = 1.132$  with [O II] surface brightness exceeding  $10^{-18} \text{ erg s}^{-1} \text{ cm}^{-2} \text{ arcsec}^{-2}$  and a central body spanning nearly 100 kpc in diameter. While the velocity map exhibits apparent organized motions in different parts of the nebula, no single coherent flow model, either a rotational, radial, or linear velocity field, can capture these features at once. The 2nd-order VSF determined based on residual velocities after a best-fit linear velocity gradient is subtracted across the nebula exhibits a spectacular agreement with the Kolmogorov expectation, implying subsonic turbulence and a constant energy transfer rate over the spatial scales covered by the measurements (Chen et al., 2023b). The surprising agreement between the observed  $S_2(l)$  and the Kolmogorov expectation has profound implications for the nature of the quasar nebula. First, subsonic turbulence is at odds with the observed large velocity fluctuations, greater than  $100 \text{ km s}^{-1}$ , exceeding the sound speed  $c_s \approx 10 \text{ km s}^{-1}$  expected for cool, photoionized gas of  $T \sim 10^4 \text{ K}$ . Such discrepancy suggests that the gas is condensed out of the ambient hot halo of  $T \gtrsim 10^6 \text{ K}$  inheriting the turbulent energy of the hot halo, rather than being driven out by fast outflows from the central SMBH. Secondly, the observed turbulent power on the scale of 50 kpc implies a turbulent heating time scale of  $\approx 200\text{--}300 \text{ Myr}$ , which is much longer than the lifetime of the active quasar phase ( $< 10 \text{ Myr}$ ) (e.g., Schawinski et al., 2015; Sun et al., 2017). In contrast, many of these quasars reside in an overdense environment with numerous gas-rich satellites found and a correlation between the presence of close companions and the presence of strong, extended nebular line emission has been reported (e.g., Stockton and MacKenty, 1987; Johnson et al., 2024). The dynamical time of satellites orbiting in quasar host halos is comparable to the inferred turbulent heating time scale, making satellite interactions a likely turbulence driver in quasar nebulae.

The example presented in Fig. 11 illustrates the potential of VSF measurements to place crucial constraints on the turbulent nature of the CGM, offering illuminating insights into the physics of feedback processes. At the same time, it also highlights the limitation both in terms of the detectability of extended line-emitting nebulae and the dynamic range in spatial scales over which the VSF slopes can be robustly measured. As noted in Section 3.1, line-emission signals from the diffuse gas are highly dependent on gas density, with the intensity scaling as  $n_{\text{H}}^2$ . This means that emission-line maps primarily highlight regions of high-density gas, making it challenging to capture low-density areas. However, future large telescopes present a promising opportunity to address this limitation. Meanwhile, absorption spectroscopy provides a valuable tool to expand the reach both to lower-mass, non-quasar host halos and to spatial scales as small as  $\sim 1 \text{ pc}$  (e.g., Chen et al., 2023a). In addition, astronomers can densely sample and detect lower-density gas that emission-line maps may miss by employing absorption spectroscopy on multiple bright background sources (e.g., Newman et al., 2019). Based on the galaxy number counts from deep surveys (e.g., Metcalfe et al., 2001), it is expected that there will be on average two background sources brighter than  $B \approx 24 \text{ mag}$  and four such sources brighter than  $B \approx 24.5 \text{ mag}$  per square arcminute to enable such multiple absorption probes to complement emission measures. Combining emission line maps and multiple absorption line probes will provide spatially and spectrally resolved maps of the multiphase gas to constrain the extent, geometry, and energetics of galactic outflows and accretion over a wide range of galaxy masses and much of cosmic evolution.

## 5.2 Independent constraints from Sunyaev-Zel'dovich signals and fast radio bursts

Moving beyond UV and optical wavelengths, radio and sub-millimeter observations offer exciting avenues for studying the cosmic baryon content. One example is through the Sunyaev-Zel'dovich (SZ) effect (Sunyaev and Zeldovich, 1980), resulting from the scattering of cosmic microwave background (CMB) photons by high-energy electrons in the intracluster medium (ICM) of galaxy clusters. This inverse Compton scattering boosts the energy of the CMB photons by  $\approx k_B T_e / m_e c^2$ , shifting the CMB spectrum in a way that decreases intensity at frequencies below 218 GHz and increases intensity at higher frequencies. The anticipated signal strength expressed in terms of the CMB blackbody temperature is proportional to the thermal pressure of the ionized gas integrated along the line of sight,  $\Delta T_{\text{SZ}} / T_{\text{CMB}} \propto \int n_e (k_B T_e / m_e c^2) \sigma_T dl$ , where  $\sigma_T$  is the Thomson scattering cross-section. Unlike X-ray observations, which place stronger weights toward denser regions of the ICM, the SZ signals provide a more unbiased measure of ionized gas pressure and offer a means of tracing the baryonic content of the universe throughout cosmic history. The redshift insensitivity of SZ signals presents both advantages and disadvantages. On the positive side, this property allows SZ observations to probe sources at any distance, unrestricted to nearby objects. However, the downside is that SZ signals alone lack the discriminative capability to investigate the cosmic evolution of ionized plasma. Such limitations can be mitigated by cross-correlating the SZ signals with galaxies identified in all-sky spectroscopic surveys (e.g., Chiang et al., 2020).

As the detector technology advances, CMB telescopes become increasingly sensitive to detect the SZ signals beyond the ICM and into the intragroup gas of lower mass galaxy groups. This makes the SZ effect a powerful tool for probing the diffuse ionized gas associated with overdense galaxy environments. Although the angular resolution of SZ observations remains poor,  $\gtrsim 1'$ , these data still provide sensitive constraints for the pressure profile beyond the nominal size of massive halos (e.g., Schaan et al., 2021). The Cosmic Microwave Background Stage Four (CMB-S4) experiment, when completed, will have much-improved sensitivities for probing ionized gas associated with lower mass halos, approaching the Milky-Way halo scale (Abazajian et al., 2019). These data will enable direct comparisons between CGM observations from different techniques and provide the most stringent constraints on theoretical models.

Independently, fast radio bursts (FRBs Petroff et al., 2022) offer a unique tool for probing the cosmic baryon content. These brief, intense flashes of radio waves originating from distant galaxies are dispersed as they travel through an ionized medium, resulting in a delay in the signal's arrival time. The time it takes for the pulse to arrive is frequency dependent, following the relation  $t_{\text{arrival}} \propto (\nu/\text{GHz})^{-2} (\text{DM}/\text{cm}^{-3} \text{ pc})$ . Here DM is the dispersion measure, an integral of electron density along the path to the observer,  $\text{DM} = \int n_e dl$ . This provides a direct probe of the diffuse ionized gas, that is difficult to detect by other means. While each DM measurement includes all electrons integrated along the line of sight, from the host ISM and CGM of the FRB itself to the CGM associated with intervening galactic halos and the unbound IGM, and to the Milky Way ISM, it is possible to separate the contributions of the IGM and CGM from the host and the Milky Way by incorporating available constraints for the Milky Way ISM and the FRB host (e.g., Macquart et al., 2020). With several radio projects

underway globally, such as CHIME (CHIME/FRB Collaboration et al., 2021), ASKAP (Day et al., 2020), and HIRAX (Newburgh et al., 2016), FRB DM studies hold significant promise for measuring cosmic mean baryon content.

## Acknowledgments

The authors express their deep appreciation for the many insightful discussions with colleagues that contributed to shaping the ideas presented in this article. Special thanks are extended to Michael Rauch and John Mulchaey for their invaluable guidance, inspiration, and thoughtful input throughout the authors' careers, and to Zhijie Qu for helpful comments on an earlier draft of this article and for his assistance in preparing the mass budget panel in Figure 2 and the column density profiles in Figure 6. The authors would also like to thank Suoqing Ji for providing updated simulation predictions of the column density profiles in Figure 6.

**See Also:** Advanced readers are referred to Saas-fee lecture notes by Fumagalli (2024) and comprehensive reviews by Donahue and Voit (2022); Faucher-Giguère and Oh (2023) for detailed descriptions of relevant multi-scale physical processes that regulate the observed CGM properties. Earlier reviews on this subject include Tumlinson et al. (2017); Péroux and Howk (2020).

## References

- Abazajian K, Addison G, Adshead P, Ahmed Z, Allen SW, Alonso D, Alvarez M, Anderson A, Arnold KS, Baccigalupi C, Bailey K, Barkats D, Barron D, Barry PS, Bartlett JG, Basu Thakur R, Battaglia N, Baxter E, Bean R, Bebek C, Bender AN, Benson BA, Berger E, Bhimani S, Bischoff CA, Bleem L, Bocquet S, Boddy K, Bonato M, Bond JR, Borrill J, Bouchet FR, Brown ML, Bryan S, Burkhart B, Buza V, Byrum K, Calabrese E, Calafut V, Caldwell R, Carlstrom JE, Carron J, Cecil T, Challinor A, Chang CL, Chinone Y, Cho HMS, Cooray A, Crawford TM, Crites A, Cukierman A, Cyr-Racine FY, de Haan T, de Zotti G, Delabrouille J, Demartean M, Devlin M, Di Valentino E, Dobbs M, Duff S, Duivenvoorden A, Dvorkin C, Edwards W, Eimer J, Errard J, Essinger-Hileman T, Fabbian G, Feng C, Ferraro S, Filippini JP, Flaughner B, Fraisse AA, Frolov A, Galitzki N, Galli S, Ganga K, Gerbino M, Gilchriese M, Gluscevic V, Green D, Grin D, Grohs E, Gualtieri R, Guarino V, Gudmundsson JE, Habib S, Haller G, Halpern M, Halverson NW, Hanany S, Harrington K, Hasegawa M, Hasselfield M, Hazumi M, Heitmann K, Henderson S, Henning JW, Hill JC, Hlozek R, Holder G, Holzappel W, Hubmayr J, Huppenberger KM, Huffer M, Hui H, Irwin K, Johnson BR, Johnstone D, Jones WC, Karkare K, Katayama N, Kerby J, Kernovsky S, Kesikitalo R, Kisman T, Knox L, Kosowsky A, Kovac J, Kovetz ED, Kuhlmann S, Kuo CI, Kurita N, Kusaka A, Lahteenmaki A, Lawrence CR, Lee AT, Lewis A, Li D, Linder E, Loverde M, Lowitz A, Madhavacheril MS, Mantz A, Matsuda F, Mauskopf P, McMahon J, McQuinn M, Meerburg PD, Melin JB, Meyers J, Millea M, Mohr J, Moncelsi L, Mroczkowski T, Mukherjee S, Münchmeyer M, Nagai D, Nagy J, Namikawa T, Nati F, Natoli T, Negrello M, Newburgh L, Niemack MD, Nishino H, Nordby M, Novosad V, O'Connor P, Obied G, Padin S, Pandey S, Partridge B, Pierpaoli E, Pogosian L, Pryke C, Puglisi G, Racine B, Raghunathan S, Rahlin A, Rajagopalan S, Raveri M, Reichanadter M, Reichardt CL, Remazeilles M, Rocha G, Roe NA, Roy A, Ruhl J, Salatino M, Saliwanchik B, Schaan E, Schillaci A, Schmittfull MM, Scott D, Sehgal N, Shandera S, Sheehy C, Sherwin BD, Shirokoff E, Simon SM, Slosar A, Somerville R, Spergel D, Staggs ST, Stark A, Stompór R, Story KT, Stoughton C, Suzuki A, Tajima O, Teply GP, Thompson K, Timbie P, Tomasi M, Treu JI, Tristram M, Tucker G, Umiltà C, van Engelen A, Vieira JD, Vieregg AG, Vogelsberger M, Wang G, Watson S, White M, Whitehorn N, Wollack EJ, Kimmy Wu WL, Xu Z, Yasini S, Yeck J, Yoon KW, Young E and Zonca A (2019), Jul. CMB-S4 Science Case, Reference Design, and Project Plan. *arXiv e-prints*, arXiv:1907.04473doi:10.48550/arXiv.1907.04473. 1907.04473.
- Afruni A, Fraternali F and Pezzulli G (2019), May. Cool circumgalactic gas of passive galaxies from cosmological inflow. *A&A* 625, A11. doi:10.1051/0004-6361/201835002. 1903.06182.
- Anand A, Nelson D and Kauffmann G (2021), Jun. Characterizing the abundance, properties, and kinematics of the cool circumgalactic medium of galaxies in absorption with SDSS DR16. *MNRAS* 504 (1): 65–88. doi:10.1093/mnras/stab871. 2103.15842.
- Anglés-Alcázar D, Faucher-Giguère CA, Kereš D, Hopkins PF, Quataert E and Murray N (2017), Oct. The cosmic baryon cycle and galaxy mass assembly in the FIRE simulations. *MNRAS* 470 (4): 4698–4719. doi:10.1093/mnras/stx1517. 1610.08523.
- Arrigoni Battaia F, Hennawi JF, Prochaska JX, Oñorbe J, Farina EP, Cantalupo S and Lusso E (2019), Jan. QSO MUSEUM I: a sample of 61 extended Ly  $\alpha$ -emission nebulae surrounding  $z \sim 3$  quasars. *MNRAS* 482 (3): 3162–3205. doi:10.1093/mnras/sty2827. 1808.10857.
- Bahcall JN and Salpeter EE (1965), Nov. On the Interaction of Radiation from Distant Sources with the Intervening Medium. *ApJ* 142: 1677–1680. doi:10.1086/148460.
- Bahcall JN and Salpeter EE (1966), May. Absorption Lines in the Spectra of Distant Sources. *ApJ* 144: 847. doi:10.1086/148675.
- Bahcall JN and Spitzer Lyman J (1969), May. Absorption Lines Produced by Galactic Halos. *ApJL* 156: L63. doi:10.1086/180350.
- Bahcall JN, Sargent WLW and Schmidt M (1967), Jul. An Analysis of the Absorption Spectrum of 3c 191. *ApJL* 149: L11. doi:10.1086/180042.
- Baldwin JA, Phillips MM and Terlevich R (1981), Feb. Classification parameters for the emission-line spectra of extragalactic objects. *PASP* 93: 5–19. doi:10.1086/130766.
- Becker GD, Bolton JS and Lidz A (2015), Dec. Reionisation and High-Redshift Galaxies: The View from Quasar Absorption Lines. *PASA* 32, e045. doi:10.1017/pasa.2015.45. 1510.03368.
- Behroozi P, Wechsler RH, Hearin AP and Conroy C (2019), Sep. UNIVERSEMACHINE: The correlation between galaxy growth and dark matter halo assembly from  $z = 0-10$ . *MNRAS* 488 (3): 3143–3194. doi:10.1093/mnras/stz1182. 1806.07893.
- Bergeron J (1986), Jan. The MG II absorption system in the QSO PKS 2128-12 : a galaxy disc/halo with a radius of 65 kpc. *A&A* 155: L8–L11.
- Bigiel F, Leroy AK, Walter F, Brinks E, de Blok WJG, Kramer C, Rix HW, Schrubba A, Schuster KF, Usero A and Wiesemeyer HW (2011), Apr. A Constant Molecular Gas Depletion Time in Nearby Disk Galaxies. *ApJL* 730 (2), L13. doi:10.1088/2041-8205/730/2/L13. 1102.1720.
- Binney J and Tremaine S (2008). *Galactic Dynamics: Second Edition*, Princeton University Press.
- Boksenberg A and Sargent WLW (1978), Feb. The existence of Ca II absorption lines in the spectrum of the quasar 3C 232 due to the galaxy NGC 3067. *ApJ* 220: 42–46. doi:10.1086/155880.
- Boksenberg A, Danziger IJ, Fosbury RAE and Goss WM (1980), Dec. Ca II absorption lines in the spectrum of the quasar PKS 2020-370 due to galactic material in the group Klemola 31. *ApJL* 242: L145–L148. doi:10.1086/183420.
- Boldyrev S (2002), Apr. Kolmogorov-Burgers Model for Star-forming Turbulence. *ApJ* 569 (2): 841–845. doi:10.1086/339403. astro-ph/0108300.

- Bordoloi R, Lilly SJ, Knobel C, Bolzonella M, Kampczyk P, Carollo CM, Iovino A, Zucca E, Contini T, Kneib JP, Le Fevre O, Mainieri V, Renzini A, Scodreggio M, Zamorani G, Balestra I, Bardelli S, Bongiorno A, Caputi K, Cucciati O, de la Torre S, de Ravel L, Garilli B, Kovač K, Lamareille F, Le Borgne JF, Le Brun V, Maier C, Mignoli M, Pello R, Peng Y, Perez Montero E, Presotto V, Scarlata C, Silverman J, Tanaka M, Tasca L, Tresse L, Vergani D, Barnes L, Cappi A, Cimatti A, Coppa G, Diener C, Franzetti P, Koekemoer A, López-Sanjuan C, McCracken HJ, Moresco M, Nair P, Oesch P, Pozzetti L and Welikala N (2011), Dec. The Radial and Azimuthal Profiles of Mg II Absorption around 0.5  $z$   $\pm$  0.9 zCOSMOS Galaxies of Different Colors, Masses, and Environments. *ApJ* 743 (1), 10. doi:10.1088/0004-637X/743/1/10. 1106.0616.
- Borisova E, Cantalupo S, Lilly SJ, Marino RA, Gallego SG, Bacon R, Blaizot J, Bouché N, Brinchmann J, Carollo CM, Caruana J, Finley H, Herenz EC, Richard J, Schaye J, Straka LA, Turner ML, Urrutia T, Verhamme A and Wisotzki L (2016), Nov. Ubiquitous Giant Ly $\alpha$  Nebulae around the Brightest Quasars at  $z \sim 3.5$  Revealed with MUSE. *ApJ* 831 (1), 39. doi:10.3847/0004-637X/831/1/39. 1605.01422.
- Bregman JN (2007), Sep. The Search for the Missing Baryons at Low Redshift. *ARAA* 45 (1): 221–259. doi:10.1146/annurev.astro.45.051806.110619.0706.1787.
- Bullock JS and Boylan-Kolchin M (2017), Aug. Small-Scale Challenges to the  $\Lambda$ CDM Paradigm. *ARAA* 55 (1): 343–387. doi:10.1146/annurev-astro-091916-055313.1707.04256.
- Burbidge EM, Lynds CR and Burbidge GR (1966), Apr. ON the Measurement and Interpretation of Absorption Features in the Spectrum of the Quasi-Stellar Object 3c 191. *ApJ* 144: 447. doi:10.1086/148629.
- Burkhart B (2021), Oct. Diagnosing Turbulence in the Neutral and Molecular Interstellar Medium of Galaxies. *PASP* 133 (1028), 102001. doi:10.1088/1538-3873/ac25cf.2106.02239.
- Cantalupo S (2017), Jan, Gas Accretion and Giant Ly $\alpha$  Nebulae, Fox A and Davé R, (Eds.), Gas Accretion onto Galaxies, Astrophysics and Space Science Library, 430, pp. 195, 1612.00491.
- Cantalupo S, Arrigoni-Battaia F, Prochaska JX, Hennawi JF and Madau P (2014), Feb. A cosmic web filament revealed in Lyman- $\alpha$  emission around a luminous high-redshift quasar. *Nature* 506 (7486): 63–66. doi:10.1038/nature12898.1401.4469.
- Carlstrom JE, Holder GP and Reese ED (2002), Jan. Cosmology with the Sunyaev-Zel'dovich Effect. *ARAA* 40: 643–680. doi:10.1146/annurev.astro.40.060401.093803.astro-ph/0208192.
- Chen HW (2017). Outskirts of Distant Galaxies in Absorption. doi:10.1007/978-3-319-56570-5\_9.
- Chen HW, Lanzetta KM, Webb JK and Barcons X (1998), May. The Gaseous Extent of Galaxies and the Origin of Ly $\alpha$  Absorption Systems. III. Hubble Space Telescope Imaging of Ly $\alpha$ -absorbing Galaxies at  $z \lesssim 1$ . *ApJ* 498 (1): 77–94. doi:10.1086/305554.astro-ph/9710310.
- Chen HW, Lanzetta KM and Webb JK (2001), Jul. The Origin of C IV Absorption Systems at Redshifts  $z \lesssim 1$ : Discovery of Extended C IV Envelopes around Galaxies. *ApJ* 556 (1): 158–163. doi:10.1086/321537.astro-ph/0104403.
- Chen HW, Helsby JE, Gauthier JR, Shectman SA, Thompson IB and Tinker JL (2010), May. An Empirical Characterization of Extended Cool Gas Around Galaxies Using Mg II Absorption Features. *ApJ* 714 (2): 1521–1541. doi:10.1088/0004-637X/714/2/1521.1004.0705.
- Chen HW, Gauthier JR, Sharon K, Johnson SD, Nair P and Liang CJ (2014), Feb. Spatially resolved velocity maps of halo gas around two intermediate-redshift galaxies. *MNRAS* 438 (2): 1435–1450. doi:10.1093/mnras/stt2288.1312.0016.
- Chen HW, Johnson SD, Zahedy FS, Rauch M and Mulchaey JS (2017a), Jun. Gauging Metallicity of Diffuse Gas under an Uncertain Ionizing Radiation Field. *ApJL* 842 (2), L19. doi:10.3847/2041-8213/aa762d.1706.04645.
- Chen SFS, Simcoe RA, Torrey P, Bañados E, Cooksey K, Cooper T, Furesz G, Matejek M, Miller D, Turner M, Venemans B, Decarli R, Farina EP, Mazzucchelli C and Walter F (2017b), Dec. Mg II Absorption at  $2 < z < 7$  with Magellan/Fire. III. Full Statistics of Absorption toward 100 High-redshift QSOs. *ApJ* 850 (2), 188. doi:10.3847/1538-4357/aa9707.1612.02829.
- Chen HW, Boettcher E, Johnson SD, Zahedy FS, Rudie GC, Cooksey KL, Rauch M and Mulchaey JS (2019), Jun. A Giant Intragroup Nebula Hosting a Damped {Ly}alpha Absorber at  $z = 0.313$ . *ApJL* 878 (2), L33. doi:10.3847/2041-8213/ab25ec.1906.00005.
- Chen HW, Qu Z, Rauch M, Chen MC, Zahedy FS, Johnson SD, Schaye J, Rudie GC, Boettcher E, Cantalupo S, Faucher-Giguere CA, Greene JE, Lopez S and Simcoe RA (2023a), Sep. The Cosmic Ultraviolet Baryon Survey: Empirical Characterization of Turbulence in the Cool Circumgalactic Medium. *arXiv e-prints*, arXiv:2309.05699doi:10.48550/arXiv.2309.05699.2309.05699.
- Chen MC, Chen HW, Rauch M, Qu Z, Johnson SD, Li JH, Schaye J, Rudie GC, Zahedy FS, Boettcher E, Cooksey KL and Cantalupo S (2023b), Jan. Empirical constraints on the turbulence in QSO host nebulae from velocity structure function measurements. *MNRAS* 518 (2): 2354–2372. doi:10.1093/mnras/stac3193.2209.04344.
- Chiang YK, Makiya R, Ménard B and Komatsu E (2020), Oct. The Cosmic Thermal History Probed by Sunyaev-Zeldovich Effect Tomography. *ApJ* 902 (1), 56. doi:10.3847/1538-4357/abb403.2006.14650.
- CHIME/FRB Collaboration, Amiri M, Andersen BC, Bandura K, Berger S, Bhardwaj M, Boyce MM, Boyle PJ, Brar C, Breitman D, Cassanelli T, Chawla P, Chen T, Cliche JF, Cook A, Cubranic D, Curtin AP, Deng M, Dobbs M, Dong FA, Eadie G, Fandino M, Fonseca E, Gaensler BM, Giri U, Good DC, Halpern M, Hill AS, Hinshaw G, Josephy A, Kaczmarek JF, Kader Z, Kania JW, Kaspi VM, Landecker TL, Lang D, Leung C, Li D, Lin HH, Masui KW, McKinven R, Mena-Parra J, Merryfield M, Meyers BW, Michilli D, Milutinovic N, Mirhosseini A, Münchmeyer M, Naidu A, Newburgh L, Ng C, Patel C, Pen UL, Petroff E, Pinsonneault-Marotte T, Pleunis Z, Rafiei-Ravandi M, Rahman M, Ransom SM, Renard A, Sanghavi P, Scholz P, Shaw JR, Shin K, Siegel SR, Sikora AE, Singh S, Smith KM, Stairs I, Tan CM, Tendulkar SP, Vanderlinde K, Wang H, Wulf D and Zwaniga AV (2021), Dec. The First CHIME/FRB Fast Radio Burst Catalog. *ApJS* 257 (2), 59. doi:10.3847/1538-4365/ac33ab.2106.04352.
- Churchill CW, Nielsen NM, Kacprzak GG and Trujillo-Gomez S (2013), Feb. The Self-similarity of the Circumgalactic Medium with Galaxy Virial Mass: Implications for Cold-mode Accretion. *ApJL* 763 (2), L42. doi:10.1088/2041-8205/763/2/L42.1211.1008.
- Cooper TJ, Rudie GC, Chen HW, Johnson SD, Zahedy FS, Chen MC, Boettcher E, Walth GL, Cantalupo S, Cooksey KL, Faucher-Giguere CA, Greene JE, Lopez S, Mulchaey JS, Penton SV, Petitjean P, Putman ME, Rafelski M, Rauch M, Schaye J and Simcoe RA (2021), Dec. The Cosmic Ultraviolet Baryon Survey (CUBS) - IV. The complex multiphase circumgalactic medium as revealed by partial Lyman limit systems. *MNRAS* 508 (3): 4359–4384. doi:10.1093/mnras/stab2869.2110.13933.
- Corlies L, Peeples MS, Tumlinson J, O'Shea BW, Lehner N, Howk JC, O'Meara JM and Smith BD (2020), Jun. Figuring Out Gas & Galaxies in Enzo (FOGGIE). II. Emission from the  $z = 3$  Circumgalactic Medium. *ApJ* 896 (2), 125. doi:10.3847/1538-4357/ab9310.1811.05060.
- Cowie LL, Songaila A, Kim TS and Hu EM (1995), Apr. The Metallicity and Internal Structure of the Lyman-Alpha Forest Clouds. *AJ* 109: 1522. doi:10.1086/117381.
- Crain RA and van de Voort F (2023), Aug. Hydrodynamical Simulations of the Galaxy Population: Enduring Successes and Outstanding Challenges. *ARAA* 61: 473–515. doi:10.1146/annurev-astro-041923-043618.2309.17075.
- Day CK, Deller AT, Shannon RM, Qiu H, Bannister KW, Bhandari S, Ekers R, Flynn C, James CW, Macquart JP, Mahony EK, Phillips CJ and Xavier Prochaska J (2020), Sep. High time resolution and polarization properties of ASKAP-localized fast radio bursts. *MNRAS* 497 (3): 3335–3350. doi:10.1093/mnras/staa2138.2005.13162.
- de Blok WJG, Walter F, Ferguson AMN, Bernard EJ, van der Hulst JM, Neeleman M, Leroy AK, Ott J, Zschaechner LK, Zwaan MA, Yun MS, Langston G and Keating KM (2018), Sep. A High-resolution Mosaic of the Neutral Hydrogen in the M81 Triplet. *ApJ* 865 (1), 26. doi:10.3847/1538-4357/aad557.1808.02840.



- De Cia A, Ledoux C, Mattsson L, Petitjean P, Srianand R, Gavignaud I and Jenkins EB (2016), Dec. Dust-depletion sequences in damped Lyman- $\alpha$  absorbers. A unified picture from low-metallicity systems to the Galaxy. *A&A* 596, A97. doi:10.1051/0004-6361/201527895. 1608.08621.
- de Graaff A, Cai YC, Heymans C and Peacock JA (2019), Apr. Probing the missing baryons with the Sunyaev-Zel'dovich effect from filaments. *A&A* 624, A48. doi:10.1051/0004-6361/201935159. 1709.10378.
- Dey A, Torrey P, Rubin KHR, Zhu GB and Suresh J (2015), Aug. On the cosmic evolution of Fe/Mg in QSO absorption line systems. *MNRAS* 451 (2): 1806–1814. doi:10.1093/mnras/stv604. 1503.06792.
- Dijkstra M (2017), Apr. Saas-Fee Lecture Notes: Physics of Lyman Alpha Radiative Transfer. *arXiv e-prints*, arXiv:1704.03416v1[astro-ph]. 03416.
- Donahue M and Voit GM (2022), Aug. Baryon cycles in the biggest galaxies. *PhR* 973: 1–109. doi:10.1016/j.physrep.2022.04.005. 2204.08099.
- Draine BT (2011), Physics of the Interstellar and Intergalactic Medium, Princeton University Press.
- Dutta R, Fumagalli M, Fossati M, Rafelski M, Revalski M, Arrigoni Battaia F, D'Odorico V, Peroux C, Prichard LJ and Swinbank AM (2024), Sep. Metal line emission around  $z \sim 1$  galaxies. *arXiv e-prints*, arXiv:2409.02182doi:10.48550/arXiv.2409.02182. 2409.02182.
- Eisenstein DJ, Annis J, Gunn JE, Szalay AS, Connolly AJ, Nichol RC, Bahcall NA, Bernardi M, Burles S, Castander FJ, Fukugita M, Hogg DW, Ivezić Ž, Knapp GR, Lupton RH, Narayanan V, Postman M, Reichart DE, Richmond R, Schneider M, Schlegel DJ, Strauss MA, SubbaRao M, Tucker DL, Vanden Berk D, Vogeley MS, Weinberg DH and Yanny B (2001), Nov. Spectroscopic Target Selection for the Sloan Digital Sky Survey: The Luminous Red Galaxy Sample. *AJ* 122 (5): 2267–2280. doi:10.1086/323717. astro-ph/0108153.
- Epinat B, Contini T, Finley H, Boogaard LA, Guérou A, Brinchmann J, Carton D, Michel-Dansac L, Bacon R, Cantalupo S, Carollo M, Hamer S, Kollatschny W, Krajnović D, Marino RA, Richard J, Soucail G, Weibacher PM and Wisotzki L (2018), Jan. Ionised gas structure of 100 kpc in an over-dense region of the galaxy group COSMOS-Gr30 at  $z \sim 0.7$ . *A&A* 609, A40. doi:10.1051/0004-6361/201731877. 1710.11225.
- Faerman Y and Werk JK (2023), Oct. The Cool Circumgalactic Medium of Low-redshift Star-forming Galaxies. I. Empirical Model and Mean Properties. *ApJ* 956 (2), 92. doi:10.3847/1538-4357/ac217. 2302.00692.
- Fang T, Marshall HL, Lee JC, Davis DS and Canizares CR (2002), Jun. Chandra Detection of O VIII Ly $\alpha$  Absorption from an Overdense Region in the Intergalactic Medium. *ApJL* 572 (2): L127–L130. doi:10.1086/341665. astro-ph/0206264.
- Faucher-Giguère CA (2020), Apr. A cosmic UV/X-ray background model update. *MNRAS* 493 (2): 1614–1632. doi:10.1093/mnras/staa302. 1903.08657.
- Faucher-Giguère CA and Oh SP (2023), Aug. Key Physical Processes in the Circumgalactic Medium. *ARAA* 61: 131–195. doi:10.1146/annurev-astro-052920-125203. 2301.10253.
- Ferreras I, Lisker T, Pasquali A, Khochfar S and Kaviraj S (2009), Jul. On the formation of massive galaxies: a simultaneous study of number density, size and intrinsic colour evolution in GOODS. *MNRAS* 396 (3): 1573–1578. doi:10.1111/j.1365-2966.2009.14828.x. 0901.4555.
- Fossati M, Fumagalli M, Boselli A, Gavazzi G, Sun M and Wilman DJ (2016), Jan. MUSE sneaks a peek at extreme ram-pressure stripping events - II. The physical properties of the gas tail of ESO137-001. *MNRAS* 455 (2): 2028–2041. doi:10.1093/mnras/stv2400. 1510.04283.
- Frisch U (1995), Turbulence. The legacy of A.N. Kolmogorov, Cambridge University Press.
- Fumagalli M (2024), Aug. The multiphase circumgalactic medium and its relation to galaxies: an observational perspective. *arXiv e-prints*, arXiv:2409.00174doi:10.48550/arXiv.2409.00174. 2409.00174.
- Gaspari M, McDonald M, Hamer SL, Brighenti F, Temi P, Gendron-Marsolaïs M, Hlavacek-Larrondo J, Edge AC, Werner N, Tozzi P, Sun M, Stone JM, Tremblay GR, Hogan MT, Eckert D, Ettori S, Yu H, Biffi V and Planelles S (2018), Feb. Shaken Snow Globes: Kinematic Tracers of the Multiphase Condensation Cascade in Massive Galaxies, Groups, and Clusters. *ApJ* 854 (2), 167. doi:10.3847/1538-4357/aaa1b. 1709.06564.
- Gnat O (2017), Feb. Time-dependent Cooling in Photoionized Plasma. *ApJS* 228 (2), 11. doi:10.3847/1538-4365/228/2/11. 1706.09220.
- Greenstein JL and Schmidt M (1967), Apr. The Two Absorption-Line Redshifts in Parkes 0237-23. *ApJL* 148: L13. doi:10.1086/180003.
- Grimes JP, Heckman T, Aloisi A, Calzetti D, Leitherer C, Martin CL, Meurer G, Sembach K and Strickland D (2009), Mar. Observations of Starburst Galaxies With Far-Ultraviolet Spectrographic Explorer: Galactic Feedback in the Local Universe. *ApJS* 181 (1): 272–320. doi:10.1088/0067-0049/181/1/272.
- Gronke M, Bull P and Dijkstra M (2015), Oct. A Systematic Study of Lyman- $\alpha$  Transfer through Outflowing Shells: Model Parameter Estimation. *ApJ* 812 (2), 123. doi:10.1088/0004-637X/812/2/123. 1506.03836.
- Gunn JE and Gott J. Richard I (1972), Aug. On the Infall of Matter Into Clusters of Galaxies and Some Effects on Their Evolution. *ApJ* 176: 1. doi:10.1086/151605.
- Gunn JE and Peterson BA (1965), Nov. On the Density of Neutral Hydrogen in Intergalactic Space. *ApJ* 142: 1633–1636. doi:10.1086/148444.
- Guo Y, Bacon R, Bouché NF, Wisotzki L, Schaye J, Blaizot J, Verhamme A, Cantalupo S, Boogaard LA, Brinchmann J, Cherrey M, Kusakabe H, Langan I, Leclercq F, Matthee J, Michel-Dansac L, Schroetter I and Wendt M (2023), Dec. Bipolar outflows out to 10 kpc for massive galaxies at redshift  $z \approx 1$ . *Nature* 624 (7990): 53–56. doi:10.1038/s41586-023-06718-w. 2312.05167.
- Haardt F and Madau P (2012), Feb. Radiative Transfer in a Clumpy Universe. IV. New Synthesis Models of the Cosmic UV/X-Ray Background. *ApJ* 746 (2), 125. doi:10.1088/0004-637X/746/2/125. 1105.2039.
- Hadzhiyska B, Ferraro S, Ried Guachalla B, Schaan E, Aguilar J, Battaglia N, Bond JR, Brooks D, Calabrese E, Choi SK, Claybaugh T, Coulton WR, Dawson K, Devlin M, Dey B, Doel P, Duivenvoorden AJ, Dunkley J, Farren GS, Font-Ribera A, Forero-Romero JE, Gallardo PA, Gaztañaga E, Gontcho Gontcho S, Gralla M, Le Guillou L, Gutierrez G, Guy J, Hill JC, Hložek R, Honscheid K, Juneau S, Kisner T, Kremin A, Landriau M, Liu RH, Louis T, MacCrann N, de Macorra A, Madhavacheril M, Manera M, Meisner A, Miquel R, Moodley K, Moustakas J, Mroczkowski T, Naess S, Newman J, Niemack MD, Niz G, Page L, Palanque-Delabrouille N, Partridge B, Percival WJ, Prada F, Qu FJ, Rossi G, Sanchez E, Schlegel D, Schubnell M, Sehgal N, Seo H, Sifón C, Spergel D, Sprayberry D, Staggs S, Tarlé G, Vargas C, Vavagiakis EM, Weaver BA, Wollack EJ, Zhou R and Zou H (2024), Jul. Evidence for large baryonic feedback at low and intermediate redshifts from kinematic Sunyaev-Zel'dovich observations with ACT and DESI photometric galaxies. *arXiv e-prints*, arXiv:2407.07152doi:10.48550/arXiv.2407.07152. 2407.07152.
- Hand N, Appel JW, Battaglia N, Bond JR, Das S, Devlin MJ, Dunkley J, Dünner R, Essinger-Hileman T, Fowler JW, Hajian A, Halpern M, Hasselfield M, Hilton M, Hincks AD, Hložek R, Hughes JP, Irwin KD, Klein J, Kosowsky A, Lin YT, Marriage TA, Marsden D, McLaren M, Menanteau F, Moodley K, Niemack MD, Nolte MR, Page LA, Parker L, Partridge B, Plimpton R, Reese ED, Rojas F, Sehgal N, Sherwin BD, Sievers JL, Spergel DN, Staggs ST, Swetz DS, Switzer ER, Thornton R, Trac H, Visnjic K and Wollack E (2011), Jul. The Atacama Cosmology Telescope: Detection of Sunyaev-Zel'dovich Decrement in Groups and Clusters Associated with Luminous Red Galaxies. *ApJ* 736 (1), 39. doi:10.1088/0004-637X/736/1/39. 1101.1951.
- Ho SH, Martin CL and Schaye J (2021), Dec. How Identifying Circumgalactic Gas by Line-of-sight Velocity instead of the Location in 3D Space Affects O VI Measurements. *ApJ* 923 (2), 137. doi:10.3847/1538-4357/ac2c73. 2110.01633.
- Hogan CJ and Weymann RJ (1987), Mar. Lyman-alpha emission from the Lyman-alpha forest. *MNRAS* 225: 1P–5P. doi:10.1093/mnras/225.1.1P.
- Huang YH, Chen HW, Johnson SD and Weiner BJ (2016), Jan. Characterizing the chemically enriched circumgalactic medium of  $\sim 38$  000 luminous red galaxies in SDSS DR12. *MNRAS* 455 (2): 1713–1727. doi:10.1093/mnras/stv2327. 1510.01336.
- Huang YH, Chen HW, Shectman SA, Johnson SD, Zahedy FS, Helsby JE, Gauthier JR and Thompson IB (2021), Apr. A complete census of circumgalactic Mg II at redshift  $z \lesssim 0.5$ . *MNRAS* 502 (4): 4743–4761. doi:10.1093/mnras/stab360. 2009.12372.

- Hui L and Gnedin NY (1997), Nov. Equation of state of the photoionized intergalactic medium. *MNRAS* 292 (1): 27–42. doi:10.1093/mnras/292.1.27. astro-ph/9612232.
- Ji S, Chan TK, Hummels CB, Hopkins PF, Stern J, Kereš D, Quataert E, Faucher-Giguère CA and Murray N (2020), Aug. Properties of the circumgalactic medium in cosmic ray-dominated galaxy haloes. *MNRAS* 496 (4): 4221–4238. doi:10.1093/mnras/staa1849. 1909.00003.
- Johnson SD, Schaye J, Walth GL, Li JH, Rudie GC, Chen HW, Chen MC, Epinat B, Gaspari M, Cantalupo S, Kollatschny W, Liu ZW and Muzahid S (2022), Dec. Directly Tracing Cool Filamentary Accretion over  $\zeta$ 100 kpc into the Interstellar Medium of a Quasar Host at  $z = 1$ . *ApJ* 940 (2), L40. doi:10.3847/2041-8213/aca28e.
- Johnson SD, Liu ZW, Li JH, Schaye J, Greene JE, Cantalupo S, Rudie GC, Qu Z, Chen HW, Rafelski M, Muzahid S, Chen MC, Contini T, Kollatschny W, Mishra N, Pettigean P, Rauch M and Zahedy FS (2024), May. Discovery of Optically Emitting Circumgalactic Nebulae around the Majority of UV-luminous Quasars at Intermediate Redshift. *ApJ* 966 (2), 218. doi:10.3847/1538-4357/ad3911. 2404.00088.
- Karachentsev ID and Kashibadze OG (2006), Jan. Masses of the local group and of the M81 group estimated from distortions in the local velocity field. *Astrophysics* 49 (1): 3–18. doi:10.1007/s10511-006-0002-6.
- Kauffmann G, Heckman TM, Tremonti C, Brinchmann J, Charlot S, White SDM, Ridgway SE, Brinkmann J, Fukugita M, Hall PB, Ivezić Ž, Richards GT and Schneider DP (2003), Dec. The host galaxies of active galactic nuclei. *MNRAS* 346 (4): 1055–1077. doi:10.1111/j.1365-2966.2003.07154.x. astro-ph/0304239.
- Kennicutt RC and Evans NJ (2012), Sep. Star Formation in the Milky Way and Nearby Galaxies. *ARAAS* 50: 531–608. doi:10.1146/annurev-astro-081811-125610. 1204.3552.
- Kewley LJ, Dopita MA, Sutherland RS, Heisler CA and Trevena J (2001), Jul. Theoretical Modeling of Starburst Galaxies. *ApJ* 556 (1): 121–140. doi:10.1086/321545. astro-ph/0106324.
- Kewley LJ, Nicholls DC and Sutherland RS (2019), Aug. Understanding Galaxy Evolution Through Emission Lines. *ARAAS* 57: 511–570. doi:10.1146/annurev-astro-081817-051832. 1910.09730.
- Khairi V and Srianand R (2019), Apr. New synthesis models of consistent extragalactic background light over cosmic time. *MNRAS* 484 (3): 4174–4199. doi:10.1093/mnras/stz174. 1801.09693.
- Kirby EN, Cohen JG, Guhathakurta P, Cheng L, Bullock JS and Gallazzi A (2013), Dec. The Universal Stellar Mass-Stellar Metallicity Relation for Dwarf Galaxies. *ApJ* 779 (2), 102. doi:10.1088/0004-637X/779/2/102. 1310.0814.
- Kobayashi C, Karakas AI and Lugaro M (2020), Sep. The Origin of Elements from Carbon to Uranium. *ApJ* 900 (2), 179. doi:10.3847/1538-4357/abae65. 2008.04660.
- Kollmeier JA, Zheng Z, Davé R, Gould A, Katz N, Miralda-Escudé J and Weinberg DH (2010), Jan. Ly $\alpha$  Emission from Cosmic Structure. I. Fluorescence. *ApJ* 708 (2): 1048–1075. doi:10.1088/0004-637X/708/2/1048. 0907.0704.
- Kolmogorov A (1941), Jan. The Local Structure of Turbulence in Incompressible Viscous Fluid for Very Large Reynolds' Numbers. *Akademiia Nauk SSSR Doklady* 30: 301–305.
- Kravtsov AV, Vikhlinin AA and Meshcheryakov AV (2018), Jan. Stellar Mass—Halo Mass Relation and Star Formation Efficiency in High-Mass Halos. *Astronomy Letters* 44 (1): 8–34. doi:10.1134/S1063773717120015. 1401.7329.
- Kumar S, Chen HW, Qu Z, Chen MC, Zahedy FS, Johnson SD, Muzahid S and Cantalupo S (2024), Aug. On the Nature of the C IV-bearing Circumgalactic Medium at  $z=1$ . *arXiv e-prints*, arXiv:2408.15824doi:10.48550/arXiv.2408.15824. 2408.15824.
- Lanzetta KM, Bowen DV, Tytler D and Webb JK (1995), Apr. The Gaseous Extent of Galaxies and the Origin of Lyman-Alpha Absorption Systems: A Survey of Galaxies in the Fields of Hubble Space Telescope Spectroscopic Target QSOs. *ApJ* 442: 538. doi:10.1086/175459.
- Lehner N, Berek SC, Howk JC, Wakker BP, Tumlinson J, Jenkins EB, Prochaska JX, Augustin R, Ji S, Faucher-Giguère CA, Hafen Z, Peebles MS, Barger KA, Berg MA, Bordoloi R, Brown TM, Fox AJ, Gilbert KM, Guhathakurta P, Kalirai JS, Lockman FJ, O'Meara JM, Pisano DJ, Ribaudo J and Werk JK (2020), Sep. Project AMIGA: The Circumgalactic Medium of Andromeda. *ApJ* 900 (1), 9. doi:10.3847/1538-4357/aba49c. 2002.07818.
- Lemon C, Courbin F, More A, Schechter P, Cañameras R, Delchambre L, Leung C, Shu Y, Spiniello C, Hezaveh Y, Klüter J and McMahon R (2024), Feb. Searching for Strong Gravitational Lenses. *Space Sci. Rev.* 220 (2), 23. doi:10.1007/s11214-024-01042-9. 2310.13466.
- Li Y and Bregman J (2017), Nov. The Properties of the Galactic Hot Gaseous Halo from X-Ray Emission. *ApJ* 849 (2), 105. doi:10.3847/1538-4357/aa92c6. 1710.02116.
- Li Y, Gendron-Marsolais ML, Zhuravleva I, Xu S, Simionescu A, Tremblay GR, Lochhaas C, Bryan GL, Quataert E, Murray NW, Boselli A, Hlavacek-Larrondo J, Zheng Y, Fossati M, Li M, Emsellem E, Sarzi M, Arzamasskiy L and Vishniac ET (2020), Jan. Direct Detection of Black Hole-driven Turbulence in the Centers of Galaxy Clusters. *ApJL* 889 (1), L1. doi:10.3847/2041-8213/ab65c7. 1911.06329.
- Liang CJ and Chen HW (2014), Dec. Mining circumgalactic baryons in the low-redshift universe. *MNRAS* 445 (2): 2061–2081. doi:10.1093/mnras/stu1901. 1402.3602.
- Liang CJ, Kravtsov AV and Agertz O (2016), May. Column density profiles of multiphase gaseous haloes. *MNRAS* 458 (2): 1164–1187. doi:10.1093/mnras/stw375. 1507.07002.
- Lokhorst D, Abraham R, van Dokkum P, Wijers N and Schaye J (2019), May. On the Detectability of Visible-wavelength Line Emission from the Local Circumgalactic and Intergalactic Medium. *ApJ* 877 (1), 4. doi:10.3847/1538-4357/ab184e. 1904.07874.
- Lopez S, Tejos N, Ledoux C, Barrientos LF, Sharon K, Rigby JR, Gladders MD, Bayliss MB and Pessa I (2018), Feb. A clumpy and anisotropic galaxy halo at redshift 1 from gravitational-arc tomography. *Nature* 554 (7693): 493–496. doi:10.1038/nature25436. 1801.10175.
- Macquart JP, Prochaska JX, McQuinn M, Bannister KW, Bhandari S, Day CK, Deller AT, Ekers RD, James CW, Marnoch L, Osłowski S, Phillips C, Ryder SD, Scott DR, Shannon RM and Tejos N (2020), May. A census of baryons in the Universe from localized fast radio bursts. *Nature* 581 (7809): 391–395. doi:10.1038/s41586-020-2300-2. 2005.13161.
- Madau P (1995), Mar. Radiative Transfer in a Clumpy Universe: The Colors of High-Redshift Galaxies. *ApJ* 441: 18. doi:10.1086/175332.
- Maller AH and Bullock JS (2004), Dec. Multiphase galaxy formation: high-velocity clouds and the missing baryon problem. *MNRAS* 355 (3): 694–712. doi:10.1111/j.1365-2966.2004.08349.x. astro-ph/0406632.
- Maizumi D, Mannucci F and Brandt TD (2012), Nov. The delay-time distribution of Type Ia supernovae from Sloan II. *MNRAS* 426 (4): 3282–3294. doi:10.1111/j.1365-2966.2012.21871.x. 1206.0465.
- Marchal A, Martin PG and Gong M (2021), Nov. Resolving the Formation of Cold H I Filaments in the High-velocity Cloud Complex C. *ApJ* 921 (1), 11. doi:10.3847/1538-4357/ac0e9d. 2106.12683.
- Martin DC, Matuszewski M, Morrissey P, Neill JD, Moore A, Cantalupo S, Prochaska JX and Chang D (2015), Aug. A giant protogalactic disk linked to the cosmic web. *Nature* 524 (7564): 192–195. doi:10.1038/nature14616.
- Martin CL, Ho SH, Kacprzak GG and Churchill CW (2019), Jun. Kinematics of Circumgalactic Gas: Feeding Galaxies and Feedback. *ApJ* 878 (2), 84. doi:10.3847/1538-4357/ab18ac. 1901.09123.
- McQuinn M (2016), Sep. The Evolution of the Intergalactic Medium. *ARAAS* 54: 313–362. doi:10.1146/annurev-astro-082214-122355. 1512.00086.
- McWilliam A (1997), Jan. Abundance Ratios and Galactic Chemical Evolution. *ARAAS* 35: 503–556. doi:10.1146/annurev.astro.35.1.503.
- Menacho V, Östlin G, Bik A, Della Bruna L, Melinder J, Adamo A, Hayes M, Herenz EC and Bergvall N (2019), Aug. The impact of stellar feedback

- from velocity-dependent ionized gas maps - a MUSE view of Haro 11. *MNRAS* 487 (3): 3183–3198. doi:10.1093/mnras/stz1414. 1903.11662.
- Metcalf N, Shanks T, Campos A, McCracken HJ and Fong R (2001), May. Galaxy number counts - V. Ultradeep counts: the Herschel and Hubble Deep Fields. *MNRAS* 323 (4): 795–830. doi:10.1046/j.1365-8711.2001.04168.x. astro-ph/0010153.
- Mo HJ and Miralda-Escude J (1996), Oct. Gaseous Galactic Halos and Quasi-stellar Object Absorption-Line Systems. *ApJ* 469: 589. doi:10.1086/177808. astro-ph/9603027.
- Mo H, van den Bosch FC and White S (2010). *Galaxy Formation and Evolution*.
- Morris SL, Weymann RJ, Dressler A, McCarthy PJ, Smith BA, Terile R, Giovanelli R and Irwin M (1993), Dec. The Environment of Lyman-alpha Absorbers in the Sight Line toward 3C 273. *ApJ* 419: 524. doi:10.1086/173505. astro-ph/9307005.
- Mulchaey JS, Mushotzky RF, Burstein D and Davis DS (1996), Jan. High-Ionization Quasar Absorption Lines: A Test of the Existence of Hot Gas in Spiral-rich Groups. *ApJL* 456: L5. doi:10.1086/309861.
- Münch G and Zirin H (1961), Jan. Interstellar Matter at Large Distances from the Galactic Plane. *ApJ* 133: 11. doi:10.1086/146999.
- Muzahid S, Fonseca G, Roberts A, Rosenwasser B, Richter P, Narayanan A, Churchill C and Charlton J (2018), Jun. COS-Weak: probing the CGM using analogues of weak Mg II absorbers at  $z \lesssim 0.3$ . *MNRAS* 476 (4): 4965–4986. doi:10.1093/mnras/sty529. 1709.03999.
- Naab T and Ostriker JP (2017), Aug. Theoretical Challenges in Galaxy Formation. *ARAA* 55 (1): 59–109. doi:10.1146/annurev-astro-081913-040019. 1612.06891.
- National Academies of Sciences, Engineering, and Medicine (2021). *Pathways to Discovery in Astronomy and Astrophysics for the 2020s*, The National Academies Press. doi:10.17226/26141.
- Navarro JF, Frenk CS and White SDM (1997), Dec. A Universal Density Profile from Hierarchical Clustering. *ApJ* 490 (2): 493–508. doi:10.1086/304888. astro-ph/9611107.
- Nelson D, Kauffmann G, Pillepich A, Genel S, Springel V, Pakmor R, Hernquist L, Weinberger R, Torrey P, Vogelsberger M and Marinacci F (2018), Jun. The abundance, distribution, and physical nature of highly ionized oxygen O VI, O VII, and O VIII in IllustrisTNG. *MNRAS* 477 (1): 450–479. doi:10.1093/mnras/sty656. 1712.00016.
- Newburgh LB, Bandura K, Bucher MA, Chang TC, Chiang HC, Cliche JF, Davé R, Dobbs M, Clarkson C, Ganga KM, Gogo T, Gumba A, Gupta N, Hilton M, Johnstone B, Karastergiou A, Kunz M, Lokhorst D, Maartens R, Macpherson S, Mdialose M, Moodley K, Ngwenya L, Parra JM, Peterson J, Reznik O, Saliwanchik B, Santos MG, Sievers JL, Smirnov O, Stronkhorst P, Taylor R, Vanderlinde K, Van Vuuren G, Weltman A and Witzemann A (2016), Aug., HIRAX: a probe of dark energy and radio transients, Hall HJ, Gilmozzi R and Marshall HK, (Eds.), *Ground-based and Airborne Telescopes VI*, Society of Photo-Optical Instrumentation Engineers (SPIE) Conference Series, 9906, pp. 99065X, 1607.02059.
- Newman A, Bezanson R, Johnson S, Rudie G, Greene J, Hummels C, Bundy K, Giallisco M, Kartaltepe J, Kriek M, Law D, Lemoine-Busserolle M, Malkan M, Marchesini D, Nelson E, Pierce M, Ravindranath S, Strom A, Tran KV and Whitaker K (2019), May. Resolving Galaxy Formation at Cosmic Noon. *Bull. Am. Astron. Soc.* 51 (3), 145.
- Nomoto K, Kobayashi C and Tominaga N (2013), Aug. Nucleosynthesis in Stars and the Chemical Enrichment of Galaxies. *ARAA* 51 (1): 457–509. doi:10.1146/annurev-astro-082812-140956.
- Oguri M and Marshall PJ (2010), Jul. Gravitationally lensed quasars and supernovae in future wide-field optical imaging surveys. *MNRAS* 405 (4): 2579–2593. doi:10.1111/j.1365-2966.2010.16639.x. 1001.2037.
- Oke JB and Schmidt M (1963), Sep. Optical Observations of the Radio Source 3C 273. *AJ* 68: 288–288. doi:10.1086/109103.
- Oppenheimer BD, Crain RA, Schaye J, Rahmati A, Richings AJ, Trayford JW, Tumlinson J, Bower RG, Schaller M and Theuns T (2016), Aug. Bimodality of low-redshift circumgalactic O VI in non-equilibrium EAGLE zoom simulations. *MNRAS* 460 (2): 2157–2179. doi:10.1093/mnras/stw1066. 1603.05984.
- Osterbrock DE and Ferland GJ (2006). *Astrophysics of gaseous nebulae and active galactic nuclei*, University Science Books.
- O’Sullivan E, Ponman TJ, Kolokythas K, Raychaudhury S, Babul A, Vrtilek JM, David LP, Giacintucci S, Gitti M and Haines CP (2017), Dec. The Complete Local Volume Groups Sample - I. Sample selection and X-ray properties of the high-richness subsample. *MNRAS* 472 (2): 1482–1505. doi:10.1093/mnras/stx2078. 1708.03555.
- Parkash V, Brown MJI, Jarrett TH and Bonne NJ (2018), Sep. Relationships between HI Gas Mass, Stellar Mass, and the Star Formation Rate of HICAT+WISE (H I-WISE) Galaxies. *ApJ* 864 (1), 40. doi:10.3847/1538-4357/aad3b9. 1807.06246.
- Payne CH (1925), Jan. *Stellar Atmospheres; a Contribution to the Observational Study of High Temperature in the Reversing Layers of Stars*. Ph.D. thesis, RADCLIFFE COLLEGE.
- Peebles MS, Werk JK, Tumlinson J, Oppenheimer BD, Prochaska JX, Katz N and Weinberg DH (2014), May. A Budget and Accounting of Metals at  $z \sim 0$ : Results from the COS-Halos Survey. *ApJ* 786 (1), 54. doi:10.1088/0004-637X/786/1/54. 1310.2253.
- Péroux C and Howk JC (2020), Aug. The Cosmic Baryon and Metal Cycles. *ARAA* 58: 363–406. doi:10.1146/annurev-astro-021820-120014. 2011.01935.
- Petroff E, Hessels JWT and Lorimer DR (2022), Dec. Fast radio bursts at the dawn of the 2020s. *A&ARv* 30 (1), 2. doi:10.1007/s00159-022-00139-w. 2107.10113.
- Planck Collaboration, Aghanim N, Akrami Y, Arroja F, Ashdown M, Aumont J, Baccigalupi C, Ballardini M, Banday AJ, Barreiro RB, Bartolo N, Basak S, Battye R, Benabed K, Bernard JP, Bersanelli M, Bielewicz P, Bock JJ, Bond JR, Borrill J, Bouchet FR, Boulanger F, Bucher M, Burigana C, Butler RC, Calabrese E, Cardoso JF, Carron J, Casaponsa B, Challinor A, Chiang HC, Colombo LPL, Combet C, Contreras D, Crill BP, Cuttaia F, de Bernardis P, de Zotti G, Delabrouille J, Delouis JM, Désert FX, Di Valentino E, Dickinson C, Diego JM, Donzelli S, Doré O, Douspis M, Ducout X, Dupac X, Efstathiou G, Elsner F, Enßlin TA, Eriksen HK, Falgarone E, Fantaye Y, Fergusson J, Fernandez-Cobos R, Finelli F, Forastieri F, Frailis M, Franceschi E, Frolov A, Galeotta S, Galli S, Ganga K, Génova-Santos RT, Gerbino M, Ghosh T, González-Nuevo J, Górski KM, Gratton S, Gruppiso A, Gudmundsson JE, Hamann J, Handley W, Hansen FK, Helou G, Herranz D, Hildebrandt SR, Hivon E, Huang Z, Jaffe AH, Jones WC, Karaki A, Keihänen E, Keskitalo R, Kiiveri K, Kim J, Kisner TS, Knox L, Krachmalnicoff N, Kunz M, Kurki-Suonio H, Lagache G, Lagarde JM, Langer M, Langer M, Lasenby A, Lattanzi M, Lawrence CR, Le Jeune M, Leahy JP, Lesgourgues J, Levrier F, Lewis A, Liguori M, Lilje PB, Lilley M, Lindholm V, López-Caniiego M, Lubin PM, Ma YZ, Macías-Pérez JF, Maggio G, Maino D, Mandolesi N, Mangilli A, Marcos-Caballero A, Maris M, Martin PG, Martinelli M, Martínez-González E, Matarrese S, Mauri N, McEwen JD, Meerburg PD, Meinhold PR, Melchiorri A, Mennella A, Migliaccio M, Millea M, Mitra S, Miville-Deschênes MA, Molinari D, Moneti A, Montier L, Morgante G, Moss A, Mottet S, Münchmeyer M, Natoli P, Nørgaard-Nielsen HU, Oxborrow CA, Pagano L, Paoletti D, Partridge B, Patanchon G, Pearson TJ, Peel M, Peiris HV, Perrotta F, Pettorino V, Piacentini F, Polastri L, Polenta G, Puget JL, Rachen JP, Reinecke M, Remazeilles M, Renault C, Renzi A, Rocha G, Rosset C, Roudier G, Rubiño-Martín JA, Ruiz-Granados B, Salvati L, Sandri M, Savelainen M, Scott D, Shellard EPS, Shiraishi M, Sirignano C, Sirri G, Spencer LD, Sunyaev R, Suur-Uski AS, Tauber JA, Tavagnacco D, Tenti M, Terenzi L, Toffolatti L, Tomasi M, Trombetti T, Valiviita J, Van Tent B, Vibert L, Vielva P, Villa F, Vittorio N, Wandelt BD, Wehus IK, White M, White SDM, Zacchei A and Zonca A (2020a), Sep. Planck 2018 results. I. Overview and the cosmological legacy of Planck. *A&A* 641, A1. doi:10.1051/0004-6361/201833880. 1807.06205.
- Planck Collaboration, Aghanim N, Akrami Y, Ashdown M, Aumont J, Baccigalupi C, Ballardini M, Banday AJ, Barreiro RB, Bartolo N, Basak S,

- Battye R, Benabed K, Bernard JP, Bersanelli M, Bielewicz P, Bock JJ, Bond JR, Borrill J, Bouchet FR, Boulanger F, Bucher M, Burigana C, Butler RC, Calabrese E, Cardoso JF, Carron J, Challinor A, Chiang HC, Chluba J, Colombo LPL, Combet C, Contreras D, Crill BP, Cuttaia F, de Bernardis P, de Zotti G, Delabrouille J, Delouis JM, Di Valentino E, Diego JM, Doré O, Douspis M, Ducout A, Dupac X, Dusini S, Efstathiou G, Elsner F, Enßlin TA, Eriksen HK, Fantaye Y, Farhang M, Fergusson J, Fernandez-Cobos R, Finelli F, Forastieri F, Fraiis M, Fresse AA, Franceschi E, Frolov A, Galeotta S, Galli S, Ganga K, Génova-Santos RT, Gerbino M, Ghosh T, González-Nuevo J, Górski KM, Gratton S, Gruppuso A, Gudmundsson JE, Hamann J, Handley W, Hansen FK, Herranz D, Hildebrandt SR, Hivon E, Huang Z, Jaffe AH, Jones WC, Karakci A, Keihänen E, Kesikitalo R, Kiiveri K, Kim J, Kisner TS, Knox L, Krachmalnicoff N, Kunz M, Kurki-Suonio H, Lagache G, Lamarre JM, Lasenby A, Lattanzi M, Lawrence CR, Le Jeune M, Lemos P, Lesgourgues J, Levrier F, Lewis A, Liguori M, Lilje PB, Lilley M, Lindholm V, López-Caniego M, Lubin PM, Ma YZ, Macías-Pérez JF, Maggio G, Maino D, Mandolesi N, Mangilli A, Marcos-Caballero A, Maris M, Martin PG, Martinelli M, Martínez-González E, Matarrese S, Mauri N, McEwen JD, Meinhold PR, Melchiorri A, Mennella A, Migliaccio M, Millea M, Mitra S, Miville-Deschênes MA, Molinari D, Montier L, Morgante G, Moss A, Natoli P, Nørgaard-Nielsen HU, Pagano L, Paoletti D, Partridge B, Patanchon G, Peiris HV, Perrotta F, Pettorino V, Piacentini F, Polastri L, Polenta G, Puget JL, Rachen JP, Reinecke M, Remazeilles M, Renzi A, Rocha G, Rosset C, Roudier G, Rubiño-Martín JA, Ruiz-Granados B, Salvati L, Sandri M, Savelainen M, Scott D, Shellard EPS, Sirignano C, Sirri G, Spencer LD, Sunyaev R, Suur-Uski AS, Tauber JA, Tavagnacco D, Tenti M, Toffolatti L, Tomasi M, Trombetti T, Valenziano L, Valiviita J, Van Tent B, Vibert L, Vielva P, Villa F, Vittorio N, Wandelt BD, Wehus IK, White M, White SDM, Zacchei A and Zonca A (2020b), Sep. Planck 2018 results. VI. Cosmological parameters. *A&A* 641, A6. doi:10.1051/0004-6361/201833910. 1807.06209.
- Pratt CT, Qu Z and Bregman JN (2021), Oct. The Resolved Sunyaev-Zel'dovich Profiles of Nearby Galaxy Groups. *ApJ* 920 (2), 104. doi:10.3847/1538-4357/ac1796. 2105.01123.
- Putman ME, Peek JEG and Joung MR (2012), Sep. Gaseous Galaxy Halos. *ARAA* 50: 491–529. doi:10.1146/annurev-astro-081811-125612. 1207.4837.
- Qu Z, Chen HW, Rudie GC, Zahedy FS, Johnson SD, Boettcher E, Cantalupo S, Chen MC, Cooksey KL, DePalma D, Faucher-Giguère CA, Rauch M, Schaye J and Simcoe RA (2022), Nov. The Cosmic Ultraviolet Baryon Survey (CUBS) V: on the thermodynamic properties of the cool circumgalactic medium at  $z \leq 1$ . *MNRAS* 516 (4): 4882–4897. doi:10.1093/mnras/stac2528. 2209.01228.
- Qu Z, Chen HW, Rudie GC, Johnson SD, Zahedy FS, DePalma D, Boettcher E, Cantalupo S, Chen MC, Cooksey KL, Faucher-Giguère CA, Li JIH, Lopez S, Schaye J and Simcoe RA (2023), Sep. The Cosmic Ultraviolet Baryon Survey (CUBS) - VI. Connecting physical properties of the cool circumgalactic medium to galaxies at  $z \approx 1$ . *MNRAS* 524 (1): 512–528. doi:10.1093/mnras/stad1886. 2306.11274.
- Qu Z, Chen HW, Johnson SD, Rudie GC, Zahedy FS, DePalma D, Schaye J, Boettcher ET, Cantalupo S, Chen MC, Faucher-Giguère CA, Li JIH, Mulchaey JS, Petitjean P and Rafelski M (2024), Jun. The Cosmic Ultraviolet Baryon Survey (CUBS). VII. On the Warm-hot Circumgalactic Medium Probed by O VI and Ne VIII at  $0.4 \leq z \leq 0.7$ . *ApJ* 968 (1), 8. doi:10.3847/1538-4357/ad410b. 2402.08016.
- Rauch M (1998), Jan. The Lyman Alpha Forest in the Spectra of QSOs. *ARAA* 36: 267–316. doi:10.1146/annurev.astro.36.1.267. astro-ph/9806286.
- Rauch M (2000), Lyman Alpha Forest, Murdin P, (Ed.), *Encyclopedia of Astronomy and Astrophysics*, Bristol: Institute of Physics Publishing, pp. 2140.
- Rauch M, Sargent WLW, Womble DS and Barlow TA (1996), Aug. Temperature and Kinematics of C IV Absorption Systems. *ApJL* 467: L5. doi:10.1086/310187. astro-ph/9606041.
- Rauch M, Haehnelt MG and Steinmetz M (1997), May. QSO Metal Absorption Systems at High Redshift and the Signature of Hierarchical Galaxy Formation. *ApJ* 481 (2): 601–624. doi:10.1086/304085. astro-ph/9609083.
- Rauch M, Sargent WLW and Barlow TA (2001), Jun. Small-Scale Structure at High Redshift. II. Physical Properties of the C IV Absorbing Clouds. *ApJ* 554 (2): 823–840. doi:10.1086/321402. astro-ph/0104216.
- Rauch M, Sargent WLW, Barlow TA and Simcoe RA (2002), Sep. Small-Scale Structure at High Redshift. IV. Low-Ionization Gas Intersecting Three Lines of Sight to Q2237+0305. *ApJ* 576 (1): 45–60. doi:10.1086/341267. astro-ph/0204461.
- Rauch M, Haehnelt M, Bunker A, Becker G, Marleau F, Graham J, Cristiani S, Jarvis M, Lacey C, Morris S, Peroux C, Röttgering H and Theuns T (2008), Jul. A Population of Faint Extended Line Emitters and the Host Galaxies of Optically Thick QSO Absorption Systems. *ApJ* 681 (2): 856–880. doi:10.1086/525846. 0711.1354.
- Rees MJ and Ostriker JP (1977), Jun. Cooling, dynamics and fragmentation of massive gas clouds: clues to the masses and radii of galaxies and clusters. *MNRAS* 179: 541–559. doi:10.1093/mnras/179.4.541.
- Rees MJ and Sciama DW (1967), Jan. The Detection of Heavy Elements in Intergalactic Space. *ApJ* 147: 353. doi:10.1086/149005.
- Ribaudo J, Lehner N and Howk JC (2011), Jul. A Hubble Space Telescope Study of Lyman Limit Systems: Census and Evolution. *ApJ* 736 (1), 42. doi:10.1088/0004-637X/736/1/42. 1105.0659.
- Richards GT, Lacy M, Storrie-Lombardi LJ, Hall PB, Gallagher SC, Hines DC, Fan X, Papovich C, Vanden Berk DE, Trammell GB, Schneider DP, Vestergaard M, York DG, Jester S, Anderson SF, Budavári T and Szalay AS (2006), Oct. Spectral Energy Distributions and Multiwavelength Selection of Type 1 Quasars. *ApJS* 166 (2): 470–497. doi:10.1086/506525. astro-ph/0601558.
- Richter P, Nuza SE, Fox AJ, Wakker BP, Lehner N, Ben Bekhti N, Fechner C, Wendt M, Howk JC, Muzahid S, Ganguly R and Charlton JC (2017), Nov. An HST/COS legacy survey of high-velocity ultraviolet absorption in the Milky Way's circumgalactic medium and the Local Group. *A&A* 607, A48. doi:10.1051/0004-6361/201630081. 1611.07024.
- Romano D (2022), Dec. The evolution of CNO elements in galaxies. *A&ARv* 30 (1), 7. doi:10.1007/s00159-022-00144-z. 2210.04350.
- Rubin KHR, O'Meara JM, Cooksey KL, Matuszewski M, Rizzi L, Doppmann G, Kwok S, Martin DC, Moore AM, Morrissey P and Neill JD (2018), Jun. Andromeda's Parachute: A Bright Quadruply Lensed Quasar at  $z = 2.377$ . *ApJ* 859 (2), 146. doi:10.3847/1538-4357/aaaeb7. 1707.05873.
- Rudie GC, Steidel CC, Pettini M, Trainor RF, Strom AL, Hummels CB, Reddy NA and Shapley AE (2019), Nov. Column Density, Kinematics, and Thermal State of Metal-bearing Gas within the Virial Radius of  $z \sim 2$  Star-forming Galaxies in the Keck Baryonic Structure Survey. *ApJ* 885 (1), 61. doi:10.3847/1538-4357/ab4255. 1903.00004.
- Rupke DSN, Coil A, Geach JE, Tremonti C, Diamond-Stanic AM, George ER, Hickox RC, Kepley AA, Leung G, Moustakas J, Rudnick G and Sell PH (2019), Oct. A 100-kiloparsec wind feeding the circumgalactic medium of a massive compact galaxy. *Nature* 574 (7780): 643–646. doi:10.1038/s41586-019-1686-1. 1910.13507.
- Ruszkowski M and Pfrommer C (2023), Dec. Cosmic ray feedback in galaxies and galaxy clusters. *A&ARv* 31 (1), 4. doi:10.1007/s00159-023-00149-2. 2306.03141.
- Sameer, Charlton JC, Wakker BP, Kacprzak GG, Nielsen NM, Churchill CW, Richter P, Muzahid S, Ho SH, Nateghi H, Rosenwasser B, Narayanan A and Ganguly R (2024), Jun. Cloud-by-cloud multiphase investigation of the circumgalactic medium of low-redshift galaxies. *MNRAS* 530 (4): 3827–3854. doi:10.1093/mnras/stae962. 2403.05617.
- Sarazin CL (1986), Jan. X-ray emission from clusters of galaxies. *Reviews of Modern Physics* 58 (1): 1–115. doi:10.1103/RevModPhys.58.1.
- Scannapieco E, Ferrara A and Madau P (2002), Aug. Early Enrichment of the Intergalactic Medium and Its Feedback on Galaxy Formation. *ApJ* 574 (2): 590–598. doi:10.1086/341114. astro-ph/0201463.
- Schaan E, Ferraro S, Amodeo S, Battaglia N, Aiola S, Austermann JE, Beall JA, Bean R, Becker DT, Bond RJ, Calabrese E, Calafut V, Choi SK,



- Denison EV, Devlin MJ, Duff SM, Duivenvoorden AJ, Dunkley J, Dünner R, Gallardo PA, Guan Y, Han D, Hill JC, Hilton GC, Hilton M, Hložek R, Hubmayr J, Huppenberger KM, Hughes JP, Koopman BJ, MacInnis A, McMahon J, Madhavacheril MS, Moodley K, Mroczkowski T, Naess S, Nati F, Newburgh LB, Niemack MD, Page LA, Partridge B, Salatino M, Sehgal N, Schillaci A, Sifón C, Smith KM, Spergel DN, Staggs S, Storer ER, Trac H, Ullom JN, Van Lanen J, Vale LR, van Engelen A, Magaña MV, Vavagiakis EM, Wollack EJ, Xu Z and Atacama Cosmology Telescope Collaboration (2021), Mar. Atacama Cosmology Telescope: Combined kinematic and thermal Sunyaev-Zel'dovich measurements from BOSS CMASS and LOWZ halos. *PRD* 103 (6), 063513. doi:10.1103/PhysRevD.103.063513. 2009.05557.
- Schawinski K, Koss M, Berney S and Sartori LF (2015), Aug. Active galactic nuclei flicker: an observational estimate of the duration of black hole growth phases of  $\sim 10^5$  yr. *MNRAS* 451 (3): 2517–2523. doi:10.1093/mnras/stv1136. 1505.06733.
- Schaye J, Rauch M, Sargent WLW and Kim TS (2000), Sep. The Detection of Oxygen in the Low-Density Intergalactic Medium. *ApJL* 541 (1): L1–L4. doi:10.1086/312892. astro-ph/0008011.
- Schaye J, Aguirre A, Kim TS, Theuns T, Rauch M and Sargent WLW (2003), Oct. Metallicity of the Intergalactic Medium Using Pixel Statistics. II. The Distribution of Metals as Traced by C IV. *ApJ* 596 (2): 768–796. doi:10.1086/378044. astro-ph/0306469.
- Schaye J, Carswell RF and Kim TS (2007), Aug. A large population of metal-rich, compact, intergalactic CIV absorbers - evidence for poor small-scale metal mixing. *MNRAS* 379 (3): 1169–1194. doi:10.1111/j.1365-2966.2007.12005.x. astro-ph/0701761.
- Schmidt M (1963), Mar. 3C 273 : A Star-Like Object with Large Red-Shift. *Nature* 197 (4872): 1040. doi:10.1038/1971040a0.
- Schneider EE, Ostriker EC, Robertson BE and Thompson TA (2020), May. The Physical Nature of Starburst-driven Galactic Outflows. *ApJ* 895 (1), 43. doi:10.3847/1538-4357/ab8ae8. 2002.10468.
- Shen S, Madau P, Guedes J, Mayer L, Prochaska JX and Wadsley J (2013), Mar. The Circumgalactic Medium of Massive Galaxies at  $z \sim 3$ : A Test for Stellar Feedback, Galactic Outflows, and Cold Streams. *ApJ* 765 (2), 89. doi:10.1088/0004-637X/765/2/89. 1205.0270.
- Shull JM, Smith BD and Danforth CW (2012), Nov. The Baryon Census in a Multiphase Intergalactic Medium: 30% of the Baryons May Still be Missing. *ApJ* 759 (1), 23. doi:10.1088/0004-637X/759/1/23. 1112.2706.
- Singh P, Majumdar S, Nath BB and Silk J (2018), Aug. X-ray and SZ constraints on the properties of hot CGM. *MNRAS* 478 (3): 2909–2914. doi:10.1093/mnras/sty1276. 1801.06557.
- Somerville RS and Davé R (2015), Aug. Physical Models of Galaxy Formation in a Cosmological Framework. *ARAA* 53: 51–113. doi:10.1146/annurev-astro-082812-140951. 1412.2712.
- Spitzer Lyman J (1956), Jul. On a Possible Interstellar Galactic Corona. *ApJ* 124: 20. doi:10.1086/146200.
- Spitzer L (1962). Physics of Fully Ionized Gases, Interscience Publishers.
- Steidel CC, Dickinson M, Meyer DM, Adelberger KL and Sembach KR (1997), May. Quasar Absorbing Galaxies at  $z \sim 1$ : Deep Imaging and Spectroscopy in the Field of 3C 336. *ApJ* 480 (2): 568–588. doi:10.1086/303994. astro-ph/9610230.
- Stockton A and MacKenty JW (1987), May. Extended Emission-Line Regions around QSOs. *ApJ* 316: 584. doi:10.1086/165227.
- Sun M, Voit GM, Donahue M, Jones C, Forman W and Vikhlinin A (2009), Mar. Chandra Studies of the X-Ray Gas Properties of Galaxy Groups. *ApJ* 693 (2): 1142–1172. doi:10.1088/0004-637X/693/2/1142. 0805.2320.
- Sun AL, Greene JE and Zakamska NL (2017), Feb. Sizes and Kinematics of Extended Narrow-line Regions in Luminous Obscured AGN Selected by Broadband Images. *ApJ* 835 (2), 222. doi:10.3847/1538-4357/835/2/222. 1611.04469.
- Sunyaev RA and Zeldovich IB (1980), Jan. Microwave background radiation as a probe of the contemporary structure and history of the universe. *ARAA* 18: 537–560. doi:10.1146/annurev.aa.18.090180.002541.
- Tchernyshyov K, Werk JK, Wilde MC, Prochaska JX, Tripp TM, Burchett JN, Bordoloi R, Howk JC, Lehner N, O'Meara JM, Tejos N and Tumlinson J (2022), Mar. The CGM<sup>2</sup> Survey: Circumgalactic O VI from Dwarf to Massive Star-forming Galaxies. *ApJ* 927 (2), 147. doi:10.3847/1538-4357/ac450c. 2110.13167.
- Tinker JL and Chen HW (2008), Jun. On The Halo Occupation of Dark Baryons. *ApJ* 679 (2): 1218–1231. doi:10.1086/587432. 0709.1470.
- Tojeiro R, Percival WJ, Heavens AF and Jimenez R (2011), May. The stellar evolution of luminous red galaxies, and its dependence on colour, redshift, luminosity and modelling. *MNRAS* 413 (1): 434–460. doi:10.1111/j.1365-2966.2010.18148.x. 1011.2346.
- Torrey P, Vogelsberger M, Marinacci F, Pakmor R, Springel V, Nelson D, Naiman J, Pillepich A, Genel S, Weinberger R and Hernquist L (2019), Apr. The evolution of the mass-metallicity relation and its scatter in IllustrisTNG. *MNRAS* 484 (4): 5587–5607. doi:10.1093/mnras/stz243. 1711.05261.
- Tremonti CA, Heckman TM, Kauffmann G, Brinchmann J, Charlot S, White SDM, Seibert M, Peng EW, Schlegel DJ, Uomoto A, Fukugita M and Brinkmann J (2004), Oct. The Origin of the Mass-Metallicity Relation: Insights from 53,000 Star-forming Galaxies in the Sloan Digital Sky Survey. *ApJ* 613 (2): 898–913. doi:10.1086/423264. astro-ph/0405537.
- Tumlinson J, Thom C, Werk JK, Prochaska JX, Tripp TM, Weinberg DH, Peebles MS, O'Meara JM, Oppenheimer BD, Meiring JD, Katz NS, Davé R, Ford AB and Sembach KR (2011), Nov. The Large, Oxygen-Rich Halos of Star-Forming Galaxies Are a Major Reservoir of Galactic Metals. *Science* 334 (6058): 948. doi:10.1126/science.1209840. 1111.3980.
- Tumlinson J, Peebles MS and Werk JK (2017), Aug. The Circumgalactic Medium. *ARAA* 55 (1): 389–432. doi:10.1146/annurev-astro-091916-055240. 1709.09180.
- van de Voort F, Schaye J, Altay G and Theuns T (2012), Apr. Cold accretion flows and the nature of high column density H I absorption at redshift 3. *MNRAS* 421 (4): 2809–2819. doi:10.1111/j.1365-2966.2012.20487.x. 1109.5700.
- Vanden Berk DE, Richards GT, Bauer A, Strauss MA, Schneider DP, Heckman TM, York DG, Hall PB, Fan X, Knapp GR, Anderson SF, Annis J, Bahcall NA, Bernardi M, Briggs JW, Brinkmann J, Brunner R, Burles S, Carey L, Castander FJ, Connolly AJ, Crocker JH, Csabai I, Doi M, Finkbeiner D, Friedman S, Frieman JA, Fukugita M, Gunn JE, Hennessy GS, Ivezić Ž, Kent S, Kunszt PZ, Lamb DQ, Leger RF, Long DC, Loveday J, Lupton RH, Meiksin A, Merelli A, Munn JA, Newberg HJ, Newcomb M, Nichol RC, Owen R, Pier JR, Pope A, Rockosi CM, Schlegel DJ, Siegmund WA, Smee S, Snir Y, Stoughton C, Stubbs C, SubbaRao M, Szalay AS, Szokoly GP, Tremonti C, Uomoto A, Waddell P, Yanny B and Zheng W (2001), Aug. Composite Quasar Spectra from the Sloan Digital Sky Survey. *AJ* 122 (2): 549–564. doi:10.1086/321167. astro-ph/0105231.
- Veilleux S, Cecil G and Bland-Hawthorn J (2005), Sep. Galactic Winds. *ARAA* 43 (1): 769–826. doi:10.1146/annurev.astro.43.072103.150610. astro-ph/0504435.
- Verhamme A, Schaerer D and Maselli A (2006), Dec. 3D Ly $\alpha$  radiation transfer. I. Understanding Ly $\alpha$  line profile morphologies. *A&A* 460 (2): 397–413. doi:10.1051/0004-6361:20065554. astro-ph/0608075.
- Verner DA, Barthel PD and Tytler D (1994a), Dec. Atomic data for absorption lines from the ground level at wavelengths greater than 228Å. *A&AS* 108: 287–340.
- Verner DA, Tytler D and Barthel PD (1994b), Jul. Far-Ultraviolet Absorption Spectra of Quasars: How to Find Missing Hot Gas and Metals. *ApJ* 430: 186. doi:10.1086/174392.
- Voit GM, Meece G, Li Y, O'Shea BW, Bryan GL and Donahue M (2017), Aug. A Global Model for Circumgalactic and Cluster-core Precipitation. *ApJ* 845 (1), 80. doi:10.3847/1538-4357/aa7d04. 1607.02212.
- Voit GM, Donahue M, Zahedy F, Chen HW, Werk J, Bryan GL and O'Shea BW (2019), Jul. Circumgalactic Pressure Profiles Indicate Precipitation-

- limited Atmospheres for  $M_* \sim 10^9 - 10^{11.5} M_\odot$ . *ApJL* 879 (1), L1. doi:10.3847/2041-8213/ab2766. 1903.00084.
- Walsh D, Carswell RF and Weymann RJ (1979), May. 0957+561 A, B: twin quasistellar objects or gravitational lens? *Nature* 279: 381–384. doi:10.1038/279381a0.
- Weinberg DH, Holtzman JA, Hasselquist S, Bird JC, Johnson JA, Shetrone M, Sobeck J, Allende Prieto C, Bizyaev D, Carrera R, Cohen RE, Cunha K, Ebelke G, Fernandez-Trincado JG, García-Hernández DA, Hayes CR, Jönsson H, Lane RR, Majewski SR, Malanushenko V, Mészáros S, Nidever DL, Nitschelm C, Pan K, Rix HW, Rybizki J, Schiavon RP, Schneider DP, Wilson JC and Zamora O (2019), Mar. Chemical Cartography with APOGEE: Multi-element Abundance Ratios. *ApJ* 874 (1), 102. doi:10.3847/1538-4357/ab07c7. 1810.12325.
- Werk JK, Prochaska JX, Tumlinson J, Peebles MS, Tripp TM, Fox AJ, Lehner N, Thom C, O’Meara JM, Ford AB, Bordoloi R, Katz N, Tejos N, Oppenheimer BD, Davé R and Weinberg DH (2014), Sep. The COS-Halos Survey: Physical Conditions and Baryonic Mass in the Low-redshift Circumgalactic Medium. *ApJ* 792 (1), 8. doi:10.1088/0004-637X/792/1/8. 1403.0947.
- White SDM and Rees MJ (1978), May. Core condensation in heavy halos: a two-stage theory for galaxy formation and clustering. *MNRAS* 183: 341–358. doi:10.1093/mnras/183.3.341.
- Wisotzki L, Bacon R, Brinchmann J, Cantalupo S, Richter P, Schaye J, Schmidt KB, Urrutia T, Weilbacher PM, Akhlaghi M, Bouché N, Contini T, Guiderdoni B, Herenz EC, Inami H, Kerutt J, Leclercq F, Marino RA, Maseda M, Monreal-Ibero A, Nanayakkara T, Richard J, Saust R, Steinmetz M and Wendt M (2018), Oct. Nearly all the sky is covered by Lyman- $\alpha$  emission around high-redshift galaxies. *Nature* 562 (7726): 229–232. doi:10.1038/s41586-018-0564-6. 1810.00843.
- Wolfe AM, Gawiser E and Prochaska JX (2005), Sep. Damped Ly  $\alpha$  Systems. *ARAAS* 43 (1): 861–918. doi:10.1146/annurev.astro.42.053102.133950. astro-ph/0509481.
- Yang Y, Zabludoff A, Jahnke K and Davé R (2014), Oct. The Properties of Ly $\alpha$  Nebulae: Gas Kinematics from Nonresonant Lines. *ApJ* 793 (2), 114. doi:10.1088/0004-637X/793/2/114. 1407.6801.
- York DG, Adelman J, Brinchmann J, Anderson John E. J, Anderson SF, Annis J, Bahcall NA, Bakken JA, Barkhouser R, Bastian S, Berman E, Boroski WN, Bracker S, Briegel C, Briggs JW, Brinkmann J, Brunner R, Burles S, Carey L, Carr MA, Castander FJ, Chen B, Colestock PL, Connolly AJ, Crocker JH, Csabai I, Czarapata PC, Davis JE, Doi M, Dombeck T, Eisenstein D, Ellman N, Elms BR, Evans ML, Fan X, Federwitz GR, Fiscelli L, Friedman S, Frieman JA, Fukugita M, Gillespie B, Gunn JE, Gurubani VK, de Haas E, Haldeman M, Harris FH, Hayes J, Heckman TM, Hennessy GS, Hindsley RB, Holm S, Holmgren DJ, Huang Ch, Hull C, Husby D, Ichikawa SI, Ichikawa T, Ivezić Ž, Kent S, Kim RSJ, Kinney E, Klaene M, Kleinman AN, Kleinman S, Knapp GR, Korienek J, Kron RG, Kunszt PZ, Lamb DQ, Lee B, Leger RF, Limmongkol S, Lindenmeyer C, Long DC, Loomis C, Loveday J, Lucinio R, Lupton RH, MacKinnon B, Mannery EJ, Mantsch PM, Margon B, McGehee P, McKay TA, Meiksin A, Merelli A, Monet DG, Munn JA, Narayanan VK, Nash T, Neilsen E, Neswold R, Newberg HJ, Nichol RC, Nicinski T, Nonino M, Okada N, Okamura S, Ostriker JP, Owen R, Pauls AG, Peoples J, Peterson RL, Petravick D, Pier JR, Pope A, Pordes R, Prosapio A, Rechenmacher R, Quinn TR, Richards GT, Richmond MW, Rivetta CH, Rockosi CM, Ruthmansdorfer K, Sandford D, Schlegel DJ, Schneider DP, Sekiguchi M, Sergey G, Shimasaku K, Siegmund WA, Smee S, Smith JA, Snedden S, Stone R, Stoughton C, Strauss MA, Stubbs C, SubbaRao M, Szalay AS, Szapudi I, Szokoly GP, Thakar AR, Tremonti C, Tucker DL, Uomoto A, Vanden Berk D, Vogeley MS, Waddell P, Wang Si, Watanabe M, Weinberg DH, Yanny B, Yasuda N and SDSS Collaboration (2000), Sep. The Sloan Digital Sky Survey: Technical Summary. *AJ* 120 (3): 1579–1587. doi:10.1086/301513. astro-ph/0006396.
- Zahedy FS, Chen HW, Rauch M, Wilson ML and Zabludoff A (2016), May. Probing the cool interstellar and circumgalactic gas of three massive lensing galaxies at  $z = 0.4-0.7$ . *MNRAS* 458 (3): 2423–2442. doi:10.1093/mnras/stw484. 1510.04307.
- Zahedy FS, Chen HW, Gauthier JR and Rauch M (2017), Apr. On the radial profile of gas-phase Fe/ $\alpha$  ratio around distant galaxies. *MNRAS* 466 (1): 1071–1081. doi:10.1093/mnras/stw3124. 1611.09874.
- Zahedy FS, Chen HW, Johnson SD, Pierce RM, Rauch M, Huang YH, Weiner BJ and Gauthier JR (2019), Apr. Characterizing circumgalactic gas around massive ellipticals at  $z \sim 0.4$  - II. Physical properties and elemental abundances. *MNRAS* 484 (2): 2257–2280. doi:10.1093/mnras/sty3482. 1809.05115.
- Zahedy FS, Chen HW, Cooper TM, Boettcher E, Johnson SD, Rudie GC, Chen MC, Cantalupo S, Cooksey KL, Faucher-Giguère CA, Greene JE, Lopez S, Mulchaey JS, Penton SV, Petitjean P, Putman ME, Rafelski M, Rauch M, Schaye J, Simcoe RA and Walth GL (2021), Sep. The Cosmic Ultraviolet Baryon Survey (CUBS) - III. Physical properties and elemental abundances of Lyman-limit systems at  $z \geq 1$ . *MNRAS* 506 (1): 877–902. doi:10.1093/mnras/stab1661. 2106.04608.
- Zhang Y, Comparat J, Ponti G, Merloni A, Nandra K, Haberl F, Locatelli N, Zhang X, Sanders J, Zheng X, Liu A, Popesso P, Liu T, Truong N, Pillepich A, Predehl P, Salvato M, Shreeram S, Yeung MCH and Ni Q (2024), Jan. The hot circumgalactic medium in the eROSITA All-Sky Survey I. X-ray surface brightness profiles. *arXiv e-prints*, arXiv:2401.17308doi:10.48550/arXiv.2401.17308. 2401.17308.
- Zheng Y, Emerick A, Putman ME, Werk JK, Kirby EN and Peek J (2020), Dec. Characterizing the Circumgalactic Medium of the Lowest-mass Galaxies: A Case Study of IC 1613. *ApJ* 905 (2), 133. doi:10.3847/1538-4357/abc875. 2010.15645.